POLITECNICO DI TORINO

Corso di Laurea Magistrale
in Ingegneria Matematica

Tesi di Laurea Magistrale

A 3D-1D multiphase model for growing vascular tumors with angiogenesis

Relatori
Chiara Giverso
Denise Grappein
Stefano Scialò

Candidato
Francesca Marino

Anno Accademico 2024/2025

Summary

In this work we aim to provide a mathematical model both for the angiogenesis and the growth of a vascular tumor.
In the first part of the thesis, we focus only on the formation of new blood vessels, providing a hybrid model to outline the evolution of pressure, chemicals and endothelial cells, that lead the formation of the nascent vasculature.
It is important to underline the fact that, in this framework, we neglect the existence of any cancer cell population and we focus only on the growing network dynamics.
From the mathematical point of view, this kind of problem deals with coupling of PDEs defined in the interstitial tissue and the network, because fluids and chemicals are allowed to flow across the vessels walls.
Therefore, we provide a suitable numerical method that resolves the problem introduced above, exploiting the constrained minimization of a cost functional.
In the second part, instead, we introduce the tumor growth dynamics considering a multiphase model for a cell population and a liquid phase, in which chemicals are dissolved.
In this framework, the model takes into the fact that tumor responses to hypoxia conditions producing endothelial growth factor, that induce the formation of new blood vessels.
Since the main novelty of the second part is the introduction of cell dynamics, we provide a numerical method for the resolution of its governing law, the technique proposed in the first part being still valid for the coupling mechanism.
To conclude, both in the first and in the second part, we present some numerical experiments to investigate the behavior of the corresponding dynamics, in order to understand the biological reliability of the model.

Contents

Chapter 1

Introduction

1.1 Biological Overview

Angiogenesis is a process during which new blood vessels develop starting from a pre-existing vasculature. It is a crucial component of many biological processes [7] and it can occur either in healthy tissue with controlled mechanisms (embryogenesis, tissue repair, wound healing) or in pathological conditions with uncontrolled or excessive blood-vessel formation.
In this work, we focus on pathological events to study tumor-induced angiogenesis, a phenomenon that takes place because tumors can survive in their avascular phase only until they reach a diameter of approximately 1-2 mm. Over this limit, tumor metabolic demand cannot be satisfied because oxygen and nutrients are not able to reach the tumor by the sole effect of diffusion and, in order to grow beyond this size, cancer cells switch to an angiogenic phenotype, attracting blood vessels from the surrounding environment [3, 7, 16].
More precisely, as the tumor increases its volume, the shortage of oxygen leads it to hypoxia and one of the many responses to this condition is the secretion, by the tumor itself, of many polypeptides (tumour angiogenic factors, or TAFs) that induce endothelial cell migration, proliferation and differentiation. Through this multitude of chemicals, the vascular endothelial growth factor (VEGF) has been identified to be one of the main driving forces [7, 21]. In particular, VEGF spreads via the extracellular matrix (ECM) and when it reaches pre-existing blood vessels, it binds to specific receptors located on the endothelial cells (EC) [21].
As a result, pushed by chemotactic effects, ECs start to migrate and proliferate until the newly formed capillary network invades the tumor [7].
In fact, the endothelial cells synthesize matrix degradative enzymes (MDE) that deteriorate the ECM, enabling their migration towards the tumor with the formation of the first protrusion (*sprout*)[3, 7].
A description of this process is provided in Figure (1.1), in which the main components of the angiogenesis process are reported.
When endothelial cells start migrating, they can be classified in two main groups:

- *tipcells*, located at the extremity of capillaries which are able to lead them across chemotactic stimuli;

- *stalk cells*, the more proliferative ones, which can follow the tipcell movement giving rise to the nascent capillary.

As the network grows, many different phenomena can be observed; for example two tipcells may encounter each other and merge, leading to the *anastomosis* process. Moreover, under particular conditions, a new tipcell may arise, either from tipcell differentiation or from stalk-to-tipconversion of aN EC located just behind the leading tipcell. This process lead to two tipcells that migrate in diverging directions, thereby initiating the branching process. In proximity of the tumor, it could happen that the number of branching increases, showing the *brush border effect*.
Finally, once the newly formed vasculature reaches the tumor, cancer cells may have access to oxygen and nutrient again and, eventually, they can enter the blood vessels to form metastasis. [3]
Nevertheless, biological experiments show that the vasculature near the tumor is not able to efficiently supply oxygen and nutrients, since the tumor-induced blood vessels generally have a tortuous geometry, their walls are leaky and the lymphatic drainage is dysfunctional. Moreover, pathological conditions lead to the rapid formation of the network, preventing the full development of the barriers, which can be easily destroyed by the high pressure induced by tumor proliferation [11].

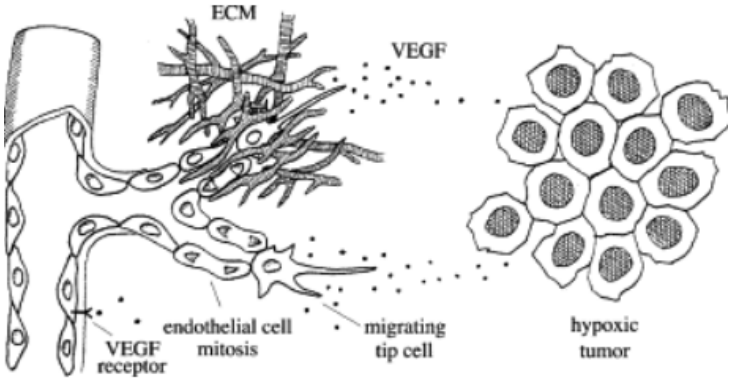

Figure 1.1: Illustration of early events in sprouting angiogenesis: endothelial cell are activated by VEGF, produced by the hypoxic tumor. They start proliferating and migrating in response to chemotactic effects and they degrade the extracellular matrix until they reach the tumor. This figure has been reproduced, with permission, from [1].

When cancer cells have access to nutrients, the process of tumor growth starts, so they can undergo mitosis, proliferation and migration.
Let us focus on the migration phenomenon, which is a fundamental step for the invasion process. In fact, when cells move in the extracellular matrix, they have to deform in order

to cross the space between fibres and they must adhere them to apply a traction force that allows the movement.
However, the structure of the ECM may also be a limit for migration, since cells are not only constituted by an easily deformable cytoplasm, but also by a stiff nucleus, whose structure consists of dense genetic materials (*chromatin*) surrounded by a lipid membrane which is sustained by structural proteins (*nuclear lamina)*[13].
In particular, when the spaces between the ECM pores are too narrow and when the nucleus is not elastic enough, the cell motility is very reduced. As a consequence, cells migration is obstructed and they cannot reach areas with higher concentrations of nutrients.
This short biological overview shows that angiogenesis and tumor growth dynamics are very complex processes, so their description is not trivial. In this perspective, in the following sections we provide a collection of works that face this problems and we will use them as a starting point for our analysis.

1.2 Mathematical models in literature

Despite a large number of in vivo and in vitro experiments tried to give an effective explanation of the phenomenon, angiogenesis is still a challenging event to be studied. In fact, it is a process involving different spatio-temporal scales and many different biological species. The formulation of in silico models may thus help its comprehension.
For these reasons, many mathematical models has been proposed with different approaches: the most important distinction consists in continuous [30] and discrete/hybrid models [25, 21].
The former are generally given by systems of non-linear partial differential equations describing the distribution of ECs, TAFs and of other chemicals dissolved in the extracellular matrix, such as oxygen or degradative enzymes. These kind of models have the advantage of capturing the angiogenic features at the macroscopic scale but they are not able to describe the geometry of the nascent vessels, nor to evaluate the inner blood flow.
In this scenario, we can cite for example [30], in which the authors propose a model of tumor-induced angiogenesis for the growth of new capillaries, that also takes into account their possible natural regression and further regrowth. From the mathematical point of view, the problem is solved thanks to a phase-field approach that resolves the capillary at full scale, while the presence of chemotactic growth factors is modelled by a PDE problem.
For what concerns discrete/hybrid models, instead, they allow to track the evolution of the single endothelial cell and so they can give a realistic representation of the evolving network. Furthermore the individual-based representation of the cells can be coupled with the macroscopic description of the chemicals, making it is possible to describe the interaction between the cells and the environment.
To give some examples of this kind of approach, we can cite the tip-tracking model proposed in [25], in which the ECs density is substituted by an indicator function that captures the network at the cell scale, while the concentration of chemicals is modelled by PDE problems.
Another example is given by [21], in which an agent-based model is employed to describe

the motion of tip cells, while a continuum approach illustrates the evolution of extracellular matrix, chemotactic growth factors, matrix degradative enzyme and stalk cells density.
Nevertheless, also discrete/hybrid methods have some disadvantages such as the fact that the number of vessels which can be considered is limited by the computational cost and moreover, also in this case, it is not always possible to evaluate the blood flow inside the nascent vessel. In this perspective, since it is fundamental to understand how the exchanges between the vessels and the tissue occur, many different models have been proposed to represent the fluid dynamics.
We can cite for example [18], in which the authors propose an algorithmic approach to generate microvascular networks, taking into account the flux of blood and oxygen between the vessels and the tissue, thanks to Starling's filtration law. Nevertheless, they do not consider any interaction between the evolving network and the angiogenic factors, so this model is not completely suitable to describe tumor-induced angiogenesis.
A more effective approach is the one proposed in [3], in which the authors focus on the angiogenesis process in order to describe the fluid flow and the chemical transport both inside the healthy tissue and the blood vessels. A continuum model for the description of chemicals and pressure is adopted, while the evolution of the network is studied at the tipcell scale, thanks to a discrete tip-tracking model.
If we want to consider not only the evolution of the network, but also the growth of an initial concentration of cancer cells, we need to look at more sophisticated models, such as the one proposed in [11]. In this work, the authors present a 3D–1D coupled model of tumor growth associated with an evolving vascular network that also takes into account the angiogenesis process. For the tridimensional domain, a multiphase approach is adopted to describe cell concentration, extracellular matrix and chemicals, whose phases are tracked by a phase-field model. The blood flow and the exchanges between vessels and tissue are actually considered, as well as the interaction between the growing network and the angiogenic growth factors.
Many other different approaches can be use to handle this kind of problems, for example the ones proposed in [32] and [33]. In [32], a phase field model for the cells and the capillaries allows to study the behavior of tumor growth and angiogenesis, while [33] can be considered as an extension of [32], in which the blood flow is also considered. In both cases, the continuous description of cells and capillaries is completed by two PDEs for the nutrients and the TAFs and by a discrete model for the tipcells. Furthermore, the latter can be activated and deactivated in response to chemotactic stimuli.
Another example of a model that take into account both the growth of a cancer cells popiulation and the development of a vascular network is provided by [10], in which the authors build an hybrid model for the growth of a multi-species tumor treated by a phase-field model combined with a law for the fluxes. The dynamics are coupled with differential equations for the extracellular matrix, degradative enzyme and TAFs, while the network evolution is managed by a biased random walk that accounts for chemotactic and haptotactic effects.
Further different approaches are given by [28, 29, 15], in which the authors consider again a continuum model for tumor growth and angiogenesis, with a discrete modelling of the network morphology. In particular, the biological tissue is considered as a non-viscous, non-linear and hyper-elastic material, the ECM and the biochemicals are regulated by

differential problems, with interstitial fluid velocity described by Poiseuille's law, blood velocity given by Darcy's law and trascapillary flux modelled via Starling's filtration law. This kind of approach allows to take into account also the effects of mechanical stimuli both on the evolution of the interstitial tissue and of the network. Moreover, it is also possible to consider the impact of the administration of cytotoxic and anti-angiogenic drugs.
To conclude, a different kind of approach is the one proposed in [26], that resolves the angiogenesis and tumor growth problems at a fully macroscopic scale. In this work, the behavior of normoxic and hypoxic cancer cells, TAFs, vasculature and necrotic cells are modelled via PDE problems, without any description of the cell scale.

1.3 Numerical methods in literature

The resolution of the biological models introduced above typically requires a method able to resolve problems defined in a tridimensional domain with an embedded cylindrical network, whose radius is much smaller than the dimension of the 3D sample.
In this context, it is often convenient to treat the network as a mono-dimensional object, but this reduction is in general non trivial. Moreover, the variational formulation of this kind of problem requires a proper trace operator that is not well posed when the dimensionality gap between the involved manifolds is higher than one.
For this reason, the resolution of these problems is still under investigation because their mathematical formalization is challenging and many works face this task, providing different resolution approaches.
We can cite [8, 9] in which the authors provide a methodological tool to handle elliptic problems in fractured domains. The coupling terms are treated as Dirac measures concentrated on the fractures and the approximation of the solution is obtained introducing suitable weighted Sobolev spaces.
A different approach is given by [14], in which the singularities produced by the exchange between the mono-dimensional geometry and the tridimensional one are treated by a decomposition technique. In this framework, the solution is split into a term that captures the singularities and a regular correction term, allowing to reformulate the 3D-1D model as a fixed point iteration scheme.
Another possible strategy is the regularization of the singularities as shown in [17], in which the exchanges are modelled via smooth kernel functions that extend the source from a mono-dimensional domain to a tridimensional neighbourhood of the vessel. Similarly, in [27] the regularization of the singularities is performed by substituting the Dirac delta sources with functions having a narrow support.
A different methodology is also proposed in [19], where the authors consider a combination of Dirichlet and Neumann conditions in correspondence to the dimensionality gap between the manifolds. In order to provide a well-posed formulation of these conditions, the Lagrange multipliers method has been proposed.
Other examples are [2, 4], whose model assumption are similar to the ones proposed in [20]. In particular, in these works the 3D-1D coupled model is derived from the fully 3D-3D one introducing suitable Sobolev spaces, that allow to define proper trace and

extension operators.
In addition, differently from [20], a domain decomposition technique is implemented, thanks to the introduction of auxiliary variables that formally decouple the tridimensional problem and the mono-dimensional one, while the final solution is obtained minimizing a cost functional, constrained by the governing equations on the subdomains.
The method proposed in [4] is an extension of [2], and the main difference lies in the fact that the former allows to deal with discontinuous functions at the interface between the tridimensional and the mono-dimensional domains.
This different mathematical choice is very useful in many biological problems, especially when the interface is constituted by a semi-permeable membrane.
Furthermore, the problems proposed both [4] and [2] are discretized using finite elements on non-conforming meshes: this is very convenient as it is possible to define different and independent meshes on each subdomain and the handling complex geometries.

1.4 The contribution of the work

In the present work, we want to provide a method able to outline both the angiogenesis process and the tumor growth dynamics and our starting point is [3], in which a 3D-1D coupled model for the sole angiogenesis is provided.
More specifically, we consider three partial differential equation problems to describe the dynamics of pressure, oxygen and vascular endothelial growth factor (VEGF). In particular, Poiseuille's and Darcy's laws describe the fluid flow in the vessels and in the interstitial tissue, respectively. The trans-capillary flux is instead treated with the Starling's filtration law.
The growth of the network is regulated by a tip-tracking model and we take into account the possibility of branching and anastomosis, according to suitable criteria related to the age of the sprouts, their direction and the available quantity of VEGF.
To take into account also tumor growth, the work presented in [3] must be extended and, to this aim, we consider the method proposed in [12].
In particular, we treat the tissue as a mixture constituted by cells, a liquid phase and the extracellular matrix, obtaining the governing equation for cells evolution with a multiphase approach and adding it to the angiogenic cascade.
For what concerns the numerical methods, we start from a finite element discretization and a Backward Euler method for every PDE problem.
Moreover, since pressure and oxygen dynamics involve a 3D-1D coupling between the interstitial tissue and the vasculature, we also have to adopt the method proposed in point is [4].
For the discretization of the growing network, instead, we implement a Forward Euler scheme, with the possibility to consider the virtual growth, i.e. we let the network grow only when the distance between to consecutive tipcells is greater than the characteristic size on a single endothelial cell.
Moreover, to resolve the governing equation for the cell dynamics we implement the Newton's method.

In detail, the thesis is organized as follows. In the first part we focus only on the angiogenesis process, in particular in Chapter 2 we provide the model assumptions and the description of the 3D-1D coupling model. In Chapters 3 and 4 we describe the 3D-1D optimization method and we provide some numerical experiments, respectively.
In the second part we introduce the tumor growth dynamics, in particular in Chapter 5 we obtain the governing law for the cells and we adapt the equation for pressure, oxygen and VEGF to the multiphase approach. In Chapter 6 we formulate the Newton's method and, finally, in Chapter 7 we provide some numerical experiments.

Part I

Angiogenesis

Chapter 2

The Mathematical Modeling of Angiogenesis

2.1 Notations and model assumptions

Before presenting the governing equations of the model, we first specify the domains over which they are defined. In this perspective, we provide the following definitions.

- The set Ω defines the full domain in which biological processes occur, encompassing both the vasculature and the surrounding tissue.
- The time interval in which the dynamics takes place is $[0, T]$ and we partition it into

  $$0 = t_0 < t_1 < ... < t_k < ... < t_K = T,$$

  with

  $$\mathcal{I}_k = (t_{k-1}, t_k] \quad \text{and} \quad \Delta\mathcal{I}_k = t_k - t_{k-1}.$$

- The capillary network at time t_k is denoted by

  $$\Sigma^k \subset \Omega \subset \mathbb{R}^3,$$

  and we neglect the regression and the remodelling of the network, considering only the *sprouting angiogenesis* phenomenon, i.e.

  $$\Sigma^0 \subseteq \Sigma^1 \subseteq ... \subseteq \Sigma^k.$$

- The set $\mathcal{D}^k = \Omega \backslash \overline{\Sigma^k}$ stands for the interstitial volume.
- The boundary of the network is given by

  $$\partial\Sigma^k = \Gamma^k \cup \partial\Sigma^k_{in} \cup \partial\Sigma^k_{out} \cup \partial\Sigma^k_d,$$

  where

– Γ^k is the lateral surface of Σ^k,

– $\partial\Sigma^k_{in} \subset \partial\Omega$ and $\partial\Sigma^k_{out} \subset \partial\Omega$ are the union of the inlet and outlet cross-sections of Σ^k respectively,

– $\partial\Sigma^k_d$ collects all the extremal cross-sections of Σ^k lying in the interior of Ω.

We suppose that $\partial\Sigma^k_{in}$ and $\partial\Sigma^k_{out}$ are fixed in time, so in the following we drop the superscript k.

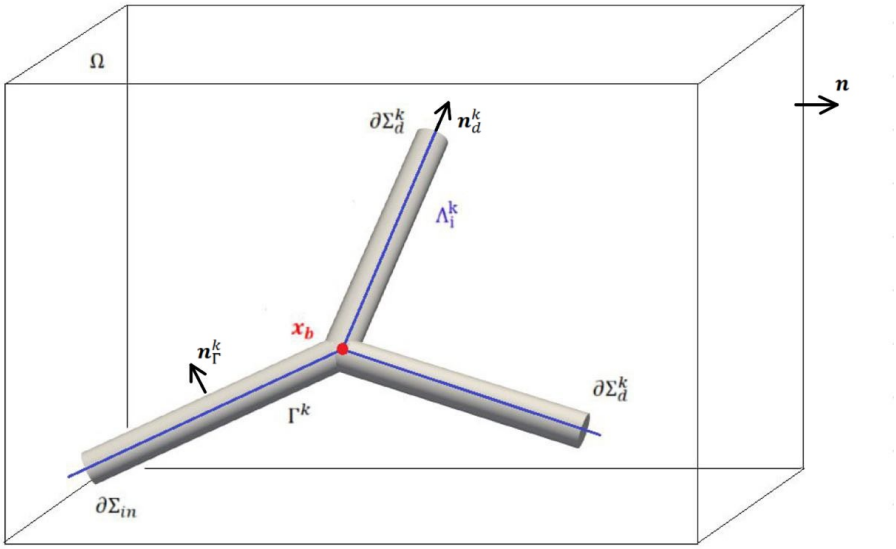

Figure 2.1: Representation of the capillary network Σ^k,

- The external boundary of the interstitial tissue is denoted by

$$\partial\mathcal{D}^k = \partial\Omega \backslash (\partial\Sigma_{in} \cup \partial\Sigma_{out}).$$

- If we imagine to cover the network Σ^k of straight cylindrical segments, the centreline of each cylinder is given by

$$\Lambda^k_i = \{\lambda^k_i(s),\ s \in (0, S^k_i)\} \quad i \in Y^k,$$

where Y^k is the set of the segments indices in the time interval $\mathcal{I}_k$ and S^k_i is curvilinear abscissa of the endpoint of each segment.

Moreover, we define Λ_{in}, Λ_{out} and Λ^k_d as the union of the centre of the sections in $\partial\Sigma_{in}$, $\partial\Sigma_{out}$ and $\partial\Sigma^k_d$, respectively.

- The set $\{\mathbf{x}_b\}_{b\in B^k}$ collects the points at which vessels centrelines join or bifurcate.

- The subset $Y_b^k \subset Y^k$ is such that the segments $\Lambda_j^k,\ j \in Y_b^k$ are connected in $\{\mathbf{x}_b\}$. Furthermore, the curvilinear abscissa $S_{i,b}$ is such that $\lambda_i^k(S_{i,b}) = \mathbf{x}_b,\ i \in Y_b^k$ (clearly $S_{i,b}$ is either 0 or S_i^k);
- $\tilde{\mathbf{n}}_{out}$ and $\tilde{\mathbf{n}}_d^k$ denote the unit normal vector to $\partial\Sigma_{out}$ and $\partial\Sigma_d^k$, both pointing outward the network Σ^k.

  Similarly, $\mathbf{n}_\Gamma^k$ is the unit normal vector to Γ^k pointing outward Γ^k, while $\mathbf{n}$ is the unit normal vector to $\partial\mathcal{D}$ pointing outward $\mathcal{D}^k$

2.2 Models and methods

The present work is an extension of the model presented in [3], in which the angiogenesis and blood delivery processes are described by three partial differential equation problems and an ordinary differential equation one.
More specifically, we treat the pressure, oxygen and VEGF dynamics with the PDE problems, while the evolution of the tip cell positions is given by the ODE one.
For what concerns the initial conditions, we establish an equilibrium configuration for the involved variables, defined over a fixed network Σ_0 and $\mathcal{D}_0 = \Omega \backslash \Sigma_0$.
Successively, the network can progress in response to the available chemicals, so we can compute the new geometry Σ_1 and then we can obtain the new fluid pressure, oxygen and VEGF distributions.

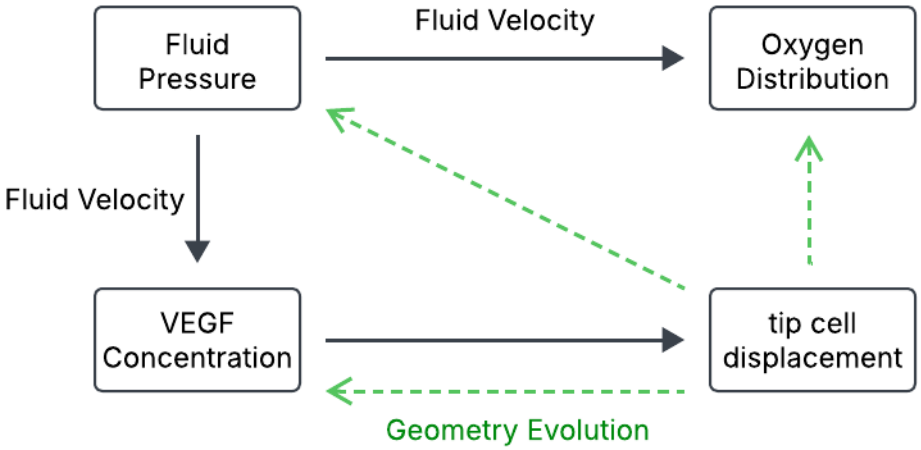

Figure 2.2: Representation of the mutual dependence of the considered quantities.

As shown in Figure (2.2), the first quantity to be estimated is the fluid pressure that allows us to acquire the fluid velocity both in blood vessels and in the interstitial tissue. Once such velocity is computed, we adopt it to evaluate the new oxygen and VEGF configurations.
It is worth to note that, at each time iteration, we keep fixed the vessel geometry and, firstly, we resolve the fluid pressure problem. This allows us to obtain the fluid velocity

that we use in the governing equations for oxygen and VEGF distributions. In particular, we solve the oxygen problem and then the VEGF one, since, as we will show in the following sections, the VEGF concentration is related to the oxygen availability.
At this point, we adopt the VEGF concentration to compute the tip cells displacement, that successively allows us to obtain the new network morphology.
When the vessels geometry is updated, we keep it fixed again and we repeat the process until the final time is reached.

2.2.1 The pressure model

Let us denote by $p(\mathbf{x},t)$ the interstitial fluid pressure and by $\tilde{p}(\mathbf{x},t)$ the the blood pressure inside the capillary network.
The 3D-3D quasi-stationary coupled model that describes the motion of fluid $\forall t \in \mathcal{I}_k$ both in the interstitial tissue and in the capillary blood vessels is the following:

$$-\nabla\cdot\left(\frac{k}{\mu}\nabla p(\mathbf{x},t)\right)+\beta_p^{LS}\frac{S}{V}\Big(p(\mathbf{x},t)-p_{LS}\Big)=0 \qquad \mathbf{x}\in\mathcal{D}^k \tag{2.1}$$

$$\frac{k}{\mu}\nabla p(\mathbf{x},t)\cdot\mathbf{n}_\Gamma^k(\mathbf{x})=\beta_p\Big(\tilde{p}(\mathbf{x},t)-p(\mathbf{x},t)-\Delta p_{onc}\Big) \qquad \mathbf{x}\in\Gamma^k \tag{2.2}$$

$$\frac{k}{\mu}\nabla p(\mathbf{x},t)\cdot\mathbf{n}(\mathbf{x})=\beta_p^{ext}\Big(p_{ext}-p(\mathbf{x},t)\Big) \qquad \mathbf{x}\in\partial\mathcal{D} \tag{2.3}$$

$$\nabla p(\mathbf{x},t)\cdot\mathbf{n}_d^k(\mathbf{x})=0 \qquad \mathbf{x}\in\partial\Sigma_d^k \tag{2.4}$$

$$-\nabla\cdot\left(\frac{R^2}{8\mu}\nabla\tilde{p}(\mathbf{x},t)\right)=0 \qquad \mathbf{x}\in\Sigma^k \tag{2.5}$$

$$\frac{R^2}{8\mu}\nabla\tilde{p}(\mathbf{x},t)\cdot\tilde{\mathbf{n}}_\Gamma^k(\mathbf{x})=\beta_p\Big(p(\mathbf{x},t)-\tilde{p}(\mathbf{x},t)+\Delta p_{onc}\Big) \qquad \mathbf{x}\in\Gamma^k \tag{2.6}$$

$$\tilde{p}(\mathbf{x},t)=\tilde{p}_{in} \qquad \mathbf{x}\in\partial\Sigma_{in} \tag{2.7}$$

$$\tilde{p}(\mathbf{x},t)=\tilde{p}_{out} \qquad \mathbf{x}\in\partial\Sigma_{out} \tag{2.8}$$

$$\nabla\tilde{p}(\mathbf{x},t)\cdot\tilde{\mathbf{n}}_d^k(\mathbf{x})=0 \qquad \mathbf{x}\in\partial\Sigma_d^k. \tag{2.9}$$

We assume that the tissue can be modelled as a saturated porous medium and so we use the Darcy's law to describe the interstitial flow velocity

$$\mathbf{v}(\mathbf{x},t)=-\frac{\kappa}{\mu}\nabla p(\mathbf{x},t) \quad \mathbf{x}\in\mathcal{D}^k,\ t\in\mathcal{I}^k. \tag{2.10}$$

On the other hand, as blood can be considered as an incompressible viscous fluid, we adopt the Poiseuille's law for the capillary blood velocity

$$\tilde{\mathbf{v}}(\mathbf{x},t)=-\frac{R^2}{8\mu}\nabla\tilde{p}(\mathbf{x},t) \quad \mathbf{x}\in\Sigma^k,\ t\in\mathcal{I}^k. \tag{2.11}$$

Moreover, parameters κ, μ, β_p and β_p^{ext} are positive scalars denoting respectively the hydraulic permeability of the tissue, the blood viscosity, the permeability of the capillary wall Γ^k and the conductivity of the external boundary.
For what concerns the term Δp_{onc}, it accounts for the oncotic pressure, a contribution due to different concentrations of chemicals on the two sides of the vessels wall. The most important substance involved in oncotic processes is a protein, the albumin, such that Δp_{onc} assumes the following expression

$$\Delta p_{onc} = \xi\Big(\overline{p}_{onc} - p_{onc}\Big), \tag{2.12}$$

with $\overline{p}_{onc}$ and p_{onc} indicating the oncotic pressure of albumin inside $\mathcal{D}^k$ and Σ^k respectively and ξ being the variance of the membrane from the perfect permeability.
Finally, we consider the lymphatic system drainage through the distributed sink term

$$\beta_p^{LS}\frac{S}{V}\Big(p(\mathbf{x},t) - p_{LS}\Big) \tag{2.13}$$

where β_p^{LS} denotes the permeability of the lymphatic wall, $\dfrac{S}{V}$ stands for the surface of lymphatic vessels per unit of tissue volume and $p_{LS} = p_{ext}$ represents the lymphatic system pressure, with p_{ext} being the basal pressure.

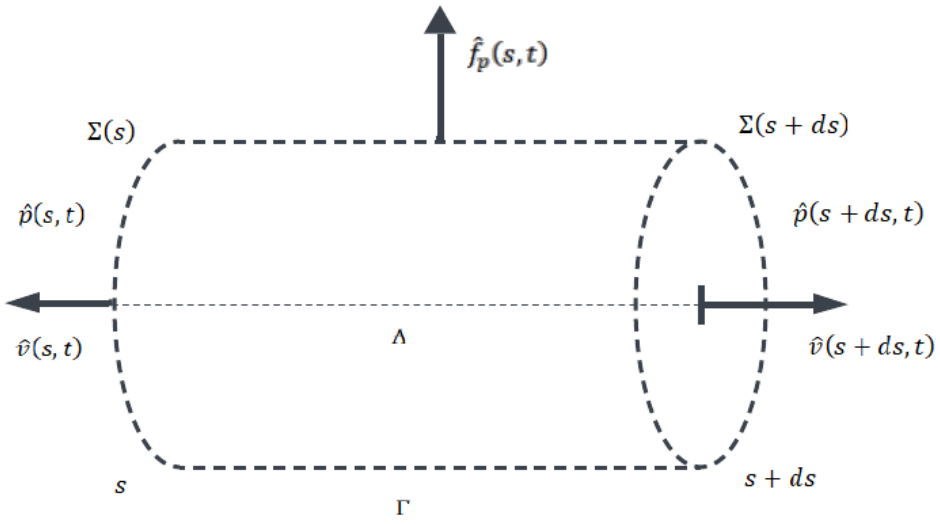

Figure 2.3: Sketch of the 1D reduced problem with related quantities.

Furthermore, Equations (2.1) and (2.5) are coupled via the interface conditions (2.2) and (2.6), which impose the conservation of the fluxes through the vessel walls. Since the radius of the vessels is much smaller than the dimension of the whole domain, it is possible to reduce the above 3D-3D model into a 3D-1D coupled one, assuming that inside the vessels the variation of pressure along the section is negligible [3].

In this perspective, we reduce the above model introducing two one-dimensional quantities, namely $\hat{p}_i(s,t)$ and $\check{p}_i(s,t)$, such that, in cylindrical coordinates, $\forall i \in Y^k$, $s \in (0, S_i^k)$ and $t \in \mathcal{I}_k$ we have

$$\tilde{p}_{|\Sigma_i^k}(r,\theta,s,t) = \hat{p}_i(s,t) \qquad \forall r \in [0,R], \forall \theta \in [0,2\pi) \tag{2.14}$$

$$p_{|\Gamma_i^k}(R,\theta,s,t) = \check{p}_i(s,t) \qquad \forall \theta \in [0,2\pi). \tag{2.15}$$

Moreover, we define the trans-capillary flux as

$$\hat{f}_p^i(s,t) = 2\pi R \beta_p \Big(\hat{p}_i(s,t) - \check{p}_i(s,t) - \Delta p_{onc}\Big) \quad s \in (0, S_i^k),\ t \in \mathcal{I}_k, \tag{2.16}$$

while the Poiseuille's equation (2.11) reduces to

$$\hat{v}_i(s,t) = -\frac{R^2}{8\mu}\frac{\partial \hat{p}_i(s,t)}{\partial s}. \tag{2.17}$$

It is also possible to define the flux inside the blood vessels as

$$Q_i(s,t) = |\Sigma_i(s)|\hat{v}_i(s,t), \tag{2.18}$$

so we can write the conservation law on the vessel centreline as

$$Q_i(s+ds,t) = Q_i(s,t) - \hat{f}_p^i(s,t)ds. \tag{2.19}$$

Now we can finally provide the formulation of the pressure problem in a 3D-1D framework:

$$-\nabla\cdot\left(\frac{k}{\mu}\nabla p(\mathbf{x},t)\right) + \beta_p^{LS}\frac{S}{V}\Big(p(\mathbf{x},t) - p_{LS}\Big) = \sum_{i\in Y^k}\hat{f}_p^i\delta_{\Lambda_i^k} \qquad \mathbf{x}\in\mathcal{D}^k \tag{2.20}$$

$$-\frac{\partial}{\partial s}\left(\frac{\pi R^4}{8\mu}\frac{\partial \hat{p}_i(s,t)}{\partial s}\right) = -\hat{f}_p^i(s,t) \qquad \forall i \in Y^k,\ s\in(0,S_i^k) \tag{2.21}$$

$$\frac{k}{\mu}\nabla p(\mathbf{x},t)\cdot\mathbf{n}(\mathbf{x}) = \beta_p^{ext}\Big(p_{ext} - p(\mathbf{x},t)\Big) \qquad \mathbf{x}\in\partial\mathcal{D} \tag{2.22}$$

$$\hat{p} = \hat{p}_{in} \qquad \text{in } \Lambda_{in} \tag{2.23}$$

$$\hat{p} = \hat{p}_{out} \qquad \text{in } \Lambda_{out} \tag{2.24}$$

$$\frac{\partial \hat{p}}{\partial s} = 0 \qquad \text{in } \Lambda_d \tag{2.25}$$

$$\sum_{j\in Y^k}\frac{\partial \hat{p}_j(S_{j,b},t)}{\partial s} = 0 \qquad \forall b \in B^k \tag{2.26}$$

$$\hat{p}_i(S_{i,b},t) = \hat{p}_j(S_{j,b},t) \qquad \forall i\neq j\in Y_b,\ \forall b\in B^k. \tag{2.27}$$

The last two equations express, respectively, the flux balance and the pressure continuity at bifurcation points, while $\hat{f}_p^i$ is given by (2.16), while $\delta_{\Lambda_i^k}$ stands for the indicator function of the ith vessel centreline.

2.2.2 The oxygen model

Correspondingly to the pressure case, the starting point for the oxygen problem is again a 3D-3D coupled problem, describing its advection, diffusion and consumption both in the interstitial tissue and in the blood vessels.
As previously mentioned and as reported in figure (2.2), the advection velocities in the interstitial tissue and in the blood vessels are computed accordingly to the gradient of fluid pressure, as defined in Equations (2.10) and (2.11), respectively.
Now, denoting by $c(\mathbf{x},t)$ and $\tilde{c}(\mathbf{x},t)$ the oxygen concentration in $\mathcal{D}^k$ and Σ^k respectively, the corresponding 3D-3D coupled problem is

$$\frac{\partial c(\mathbf{x},t)}{\partial t} = \nabla\cdot\Big(D_c\nabla c(\mathbf{x},t)\Big) - \mathbf{v}(\mathbf{x},t)\cdot\nabla c(\mathbf{x},t) - m_c\big(c(\mathbf{x},t)\big) \qquad \mathbf{x}\in\mathcal{D}^k \tag{2.28}$$

$$D_c\nabla c(\mathbf{x},t)\cdot\mathbf{n}_\Gamma^k(\mathbf{x}) = \beta_c\Big(\tilde{c}(\mathbf{x},t) - c(\mathbf{x},t)\Big) \qquad \mathbf{x}\in\Gamma^k \tag{2.29}$$

$$D_c\nabla c(\mathbf{x},t)\cdot\mathbf{n}(\mathbf{x}) = \beta_c^{ext}\Big(c_{ext} - c(\mathbf{x},t)\Big) \qquad \mathbf{x}\in\partial\mathcal{D} \tag{2.30}$$

$$\nabla c(\mathbf{x},t)\cdot\mathbf{n}_d^k(\mathbf{x}) = 0 \qquad \mathbf{x}\in\partial\Sigma_d^k \tag{2.31}$$

$$\frac{\partial\tilde{c}(\mathbf{x},t)}{\partial t} = \nabla\cdot\Big(\tilde{D}_c\nabla\tilde{c}(\mathbf{x},t)\Big) - \tilde{\mathbf{v}}(\mathbf{x},t)\cdot\nabla\tilde{c}(\mathbf{x},t) \qquad \mathbf{x}\in\Sigma^k \tag{2.32}$$

$$\tilde{c}(\mathbf{x},t_{k-1}) = 0 \qquad \mathbf{x}\in\Sigma^k\backslash\Sigma^{k-1} \tag{2.33}$$

$$\tilde{D}_c\nabla\tilde{c}(\mathbf{x},t)\cdot\tilde{\mathbf{n}}_\Gamma^k(\mathbf{x}) = \beta_c\Big(c(\mathbf{x},t) - \tilde{c}(\mathbf{x},t)\Big) \qquad \mathbf{x}\in\Gamma^k \tag{2.34}$$

$$\tilde{c}(\mathbf{x},t) = c_{in} \qquad \mathbf{x}\in\partial\Sigma_{in} \tag{2.35}$$

$$\tilde{D}_c\nabla\tilde{c}(\mathbf{x},t)\cdot\tilde{\mathbf{n}}_{out}(\mathbf{x}) = 0 \qquad \mathbf{x}\in\partial\Sigma_{out} \tag{2.36}$$

$$\nabla\tilde{c}(\mathbf{x},t)\cdot\tilde{\mathbf{n}}_d^k(\mathbf{x},t) = 0 \qquad \mathbf{x}\in\partial\Sigma_d^k \tag{2.37}$$

For $k=0$ we define the initial conditions

$$c(\mathbf{x},t_0) = c_0(\mathbf{x}) \qquad \mathbf{x}\in\mathcal{D}^0 \tag{2.38}$$

$$\tilde{c}(\mathbf{x},t_0) = \tilde{c}_0(\mathbf{x}) \qquad \mathbf{x}\in\Sigma^0. \tag{2.39}$$

On the other hand, for $k>0$ we only have to initialize the amount of oxygen in the newborn capillaries, as reported in Equation (2.33). The oxygen concentration at time t_{k-1} in $\mathcal{D}^k$ is instead available from the final value computed in $\mathcal{I}_{k-1}$,
The parameters D_c, $\tilde{D}_c$, β_c and β_c^{ext} are positive scalars denoting respectively the diffusivity in the interstitial tissue $\mathcal{D}^k$, the diffusivity in the network Σ^k, the permeability to oxygen of the blood vessels wall Γ^k and the permeability of the external boundary $\partial\mathcal{D}^k$.
Moreover, the function $m_c(c(\mathbf{x},t))$ models the oxygen metabolization by endothelial cells and we define it as

$$m_c\big(c(\mathbf{x},t)\big) = M_c c(\mathbf{x},t) \tag{2.40}$$

with M_c being a positive scalar denoting the consumption rate.

Also in this case, Equations (2.28) and (2.32) are coupled via the interface conditions (2.29) and (2.34), for the conservation of the flux.
Consequently, for the same reasons that lead us to reduce the pressure problem, we have to introduce the one-dimensional quantities

$$\tilde{c}_{|\Sigma_i^k}(r,\theta,s,t) = \hat{c}_i(s,t) \qquad \forall r \in [0,R], \forall \theta \in [0,2\pi) \tag{2.41}$$

$$c_{|\Gamma_i^k}(R,\theta,s,t) = \check{c}_i(s,t) \qquad \forall \theta \in [0,2\pi) \tag{2.42}$$

and we define the trans-capillary flux as

$$\hat{f}_c^i(s,t) = 2\pi R \beta_c \Big(\hat{c}_i(s,t) - \check{c}_i(s,t)\Big) \quad s \in (0, S_i^k),\ t \in \mathcal{I}_k. \tag{2.43}$$

In fact, we remind that the blood vessels radius is much smaller than the dimension of the tridimensional domain and we assume again that inside the vessels the oxygen variation along the section is negligible.
In this framework, the above model can be reduced into a 3D-1D one and it assumes the following form

$$\frac{\partial c(\mathbf{x},t)}{\partial t} - \nabla \cdot \Big(D_c \nabla c(\mathbf{x},t)\Big) + \mathbf{v}(\mathbf{x},t) \cdot \nabla c(\mathbf{x},t) + m_c\Big(c(\mathbf{x},t)\Big) = \sum_{i \in Y^k} \hat{f}_c^i \delta_{\Lambda_i^k} \qquad \mathbf{x} \in \mathcal{D}^k \tag{2.44}$$

$$\pi R^2 \frac{\partial \hat{c}_i(s,t)}{\partial t} - \frac{\partial}{\partial s_i}\left(\pi R^2 \tilde{D}_c \frac{\hat{c}_i(s,t)}{\partial s}\right) + \pi R^2 \hat{v}_i(s,t) \frac{\hat{c}_i(s,t)}{\partial s} = -\hat{f}_c^i(s,t) \qquad \forall i \in Y^k,\ s \in (0, S_i^k). \tag{2.45}$$

$$D_c \nabla c(\mathbf{x},t) \cdot \mathbf{n}^k(\mathbf{x}) = \beta_c^{ext}\Big(c_{ext} - c(\mathbf{x},t)\Big) \qquad \mathbf{x} \in \partial\mathcal{D} \tag{2.46}$$

$$\hat{c} = \hat{c}_{in} \qquad \text{in } \Lambda_{in} \tag{2.47}$$

$$\frac{\partial \hat{c}}{\partial s} = 0 \qquad \text{in } \Lambda_{out} \text{ and } \Lambda_d \tag{2.48}$$

$$c(\mathbf{x},t_0) = c_0(\mathbf{x}) \qquad \mathbf{x} \in \mathcal{D}^0 \tag{2.49}$$

$$\hat{c}(\mathbf{x},t_0) = \hat{c}_0(\mathbf{x}) \qquad \mathbf{x} \in \Lambda^0 \tag{2.50}$$

$$\hat{c}(\mathbf{x},t_{k-1}) = 0 \qquad \mathbf{x} \in \Lambda^k \backslash \Lambda^{k-1} \tag{2.51}$$

$$\sum_{j \in Y^b} \frac{\partial \hat{c}_j(S_{j,b},t)}{\partial s} = 0 \qquad \forall b \in B^k \tag{2.52}$$

$$\hat{c}_i(S_{i,b},t) = \hat{c}_j(S_{j,b},t) \qquad \forall i \neq j \in Y_b,\ \forall b \in B^k \tag{2.53}$$

2.2.3 The chemotactic growth factor model

The last PDE problem describes the evolution of the VEGF in the interstitial tissue and its consumption by the network.

More specifically, we suppose that the chemical is only dispersed in the tridimensional sample, so we do not solve any equation inside the blood vessels domain.
In addition, there is no VEGF flux trough the capillary wall, but its consumption by the endothelial cells occurs in terms of receptor mediated binding.
More precisely, the formulation of the problem for the chemotactic growth factor is the following

$$\frac{\partial g(\mathbf{x},t)}{\partial t} = \nabla \cdot (D_g \nabla g(\mathbf{x},t)) - \mathbf{v}(\mathbf{x},t) \cdot \nabla g(\mathbf{x},t) - \sigma g(\mathbf{x},t) + f_g(c(\mathbf{x},t)) \qquad \mathbf{x} \in \mathcal{D}^k \tag{2.54}$$

$$D_g \nabla g(\mathbf{x},t) \cdot \mathbf{n}_\Gamma^k(\mathbf{x}) = -\tilde{\sigma} g(\mathbf{x},t) \qquad \mathbf{x} \in \Gamma^k \tag{2.55}$$

$$\nabla g(\mathbf{x},t) \cdot \mathbf{n}(\mathbf{x}) = 0 \qquad \mathbf{x} \in \partial\mathcal{D} \tag{2.56}$$

$$\nabla g(\mathbf{x},t) \cdot \mathbf{n}_k^d(\mathbf{x}) = 0 \qquad \mathbf{x} \in \partial\Sigma_d^k. \tag{2.57}$$

For $k = 0$ we set the initial condition

$$g(\mathbf{x},0) = g_0(\mathbf{x}) \qquad \mathbf{x} \in \mathcal{D}^0, \tag{2.58}$$

while for $k > 0$ we set

$$g(\mathbf{x},t_k) = g(\mathbf{x},t_{k-1}) \qquad \mathbf{x} \in \mathcal{D}^k. \tag{2.59}$$

The parameters D_g, σ and $\tilde{\sigma}$ are positive scalars denoting respectively the diffusivity of the VEGF in the interstitial tissue, its natural decay and the rate of consumption by the network.
It is important to note that the above model has been modified with respect to the one presented in [3]. In fact, the latter is constituted by an advection-diffusion-reaction equation completed by a Dirichlet's boundary condition at the interface between the tumor and the interstitial tissue, which represents a constant distribution of endothelial growth factor in correspondence to the tumor boundary.
Now, the governing equation is again an advection-diffusion-reaction one, but this time we also introduce a forcing term, and complete the problem with a Neumann's boundary conditions on the whole external boundary.
In particular, the forcing term allows us to take into account the dependency of the VEGF source from the available oxygen and it is given by

$$f_g(c(\mathbf{x},t)) = r_g m_g(\mathbf{x}) f_{VEGF}(c(\mathbf{x},t)). \tag{2.60}$$

In particular, r_g is a positive scalar denoting the VEGF production rate and $m_g(\mathbf{x})$ is the indicator function that identifies the position of the VEGF source. We introduce this function because we want to understand what happens when the growth factor is produced by a source distributed in a specific area of the domain. This choice is a preliminary analysis for the model presented in the second part of the present work, in which we will introduce the tumor growth dynamics and VEGF will be produced by cancer cells.

Finally, $f_{VEGF}(c(\mathbf{x},t))$ is a function that introduces the dependency of the source from the available oxygen. More specifically, we choose $f_{VEGF}(c(\mathbf{x},t))$ as a logistic function whose expression is given by

$$f_{VEGF}(c(\mathbf{x},t)) = -\frac{1}{1+\exp\big(-c(\mathbf{x},t)+c_{hypo}\big)}+1, \tag{2.61}$$

with $c_{hypo} = 11.5$ mmHg and we report it in Figure (2.4).

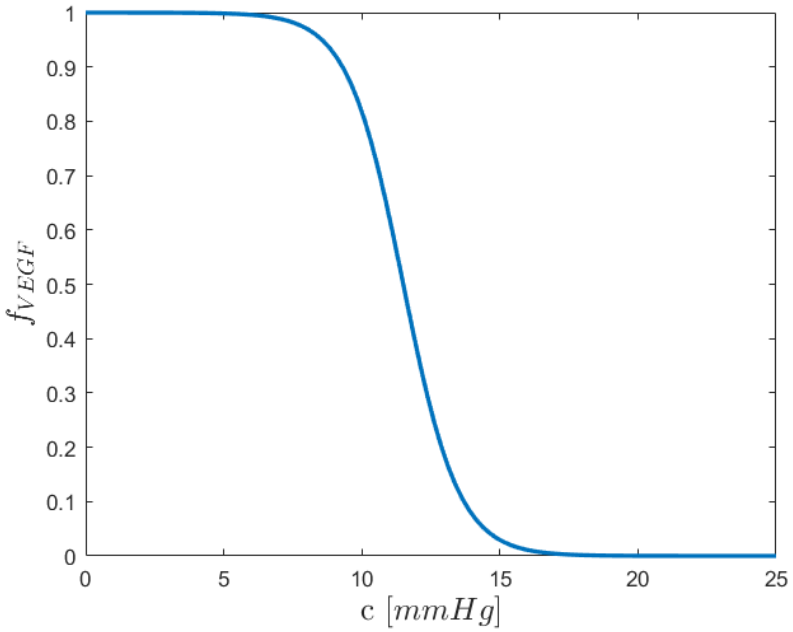

Figure 2.4: VEGF source dependency form the available oxygen.

In particular, we can observe that (2.61) presents an inflection point in correspondence to $c(\mathbf{x},t) = 11.5$ mmHg. We choose this value because, from [23], we know that the tumor produces VEGF in response to hypoxia condition, in order to stimulate the growth of the capillary network. Moreover, as reported in [23], we can consider different hypoxia thresholds to describe the wellness of the tissue. In light of this, we focus on the *physiological* hypoxia level that occurs at a concentration $c(\mathbf{x},t) = 15$ mmHg and on the *pathological* one, that occurs at $c(\mathbf{x},t) = 8$ mmHg.

As a result, in this work we decide to build the function (2.61) such that the production of VEGF is more intense in correspondence to low oxygen concentration ($c(\mathbf{x},t) < 8$ mmHg), weaker for high oxygen concentration ($c(\mathbf{x},t) > 15$ mmHg) and with a transition region between the pathological and physiological hypoxia levels. From the mathematical point of view, the inflection point of the logistic function (2.61) has been set in the middle point of the above two thresholds.

Now, similarly to pressure and oxygen problems, it is possible to introduce the one-dimensional quantity

$$g_{|\Gamma_i^k}(R,\theta,s,t) = \check{g}_i(s,t) \qquad \forall\theta \in [0,2\pi), \tag{2.62}$$

in order to rewrite (2.54)-(2.55) as a 3D equation with a singular reaction term:

$$\begin{aligned}\frac{\partial g(\mathbf{x},t)}{\partial t} - \nabla\cdot(D_g\nabla g(\mathbf{x},t)) + \mathbf{v}(\mathbf{x},t)\cdot\nabla g(\mathbf{x},t) + \sigma g(\mathbf{x},t) - f_g(\mathbf{x},t)\\ = -\sum_{i\in Y^k} 2\pi R\tilde{\sigma}\check{g}(s,t)\delta_{\Lambda_i^k} \quad \mathbf{x}\in\mathcal{D}^k,\ t\in\mathcal{I}_k.\end{aligned} \tag{2.63}$$

2.2.4 The growth of the vascular network

For what concerns the analysis of the tip cells displacement and the consequent growth of the vascular network, we adopt the same model presented in [3] and in the following we show it for completeness.
Since vessel radius is much smaller than the dimensions of the tridimensional domain, we collapse the vascular network at time t_k on its centrelines Λ_k and the interstitial domain $\mathcal{D}^k$ is extended to the whole Ω.
tip cells move in response to chemotactic stimuli and we can model their displacement. In order to achieve this purpose, it is useful to define $\mathbf{x}_p$ as the position of the generic tip cell and to consider the ordinary differential equation

$$\frac{d\mathbf{x}_p}{dt} = \mathbf{w}\big(g(\mathbf{x}_p,t_k),\mathbf{x}_p\big), \qquad p\in\mathcal{P}^k. \tag{2.64}$$

We denote by $\mathcal{P}^k$ the set of tip cells at time t_k, while $\mathbf{w}\big(g(\mathbf{x}_p,t_k),\mathbf{x}_p\big)$ stands for the velocity of the generic tip cell $p\in\mathcal{P}^k$. According to [3, 25], we define it as

$$\mathbf{w}\big(g(\mathbf{x}_p,t_k),\mathbf{x}_p\big) = \begin{cases}\dfrac{l_e}{t_c(g)}\dfrac{\mathbb{K}_{ECM}^{rand}(\mathbf{x})\nabla g}{||\mathbb{K}_{ECM}^{rand}(\mathbf{x})\nabla g||} & \text{if } g > g_{lim}\\ 0 & \text{otherwise.}\end{cases} \tag{2.65}$$

In Equation (2.65), g_{lim} is the minimum value of VEGF that endothelial cells need to proliferate, l_e is the endothelial cell length and $t_c(g)$ is the cell division time [25]. Its expression is given by

$$t_c(g) = \tau\Big(1 + e^{\left(\frac{\overline{g}}{g}-1\right)}\Big), \tag{2.66}$$

where τ is a cell proliferation parameter and $\overline{g}$ is the concentration at which $t_c = 2\tau$ [25]. Its representation is provided in Figure (2.5), for $\overline{g} = 1\cdot 10^{-13}$ kg/mm^3 and $\tau = 12$ h.
We said that tip cells move in response to chemotactic effect, but we also have to consider that their motion is strongly influenced by the structure of the substrate in which they live, so it is necessary to model the orientation of the extracellular matrix fibres.
To this aim, we introduce the matrix $\mathbb{K}_{ECM}^{rand}$, which we define as follows

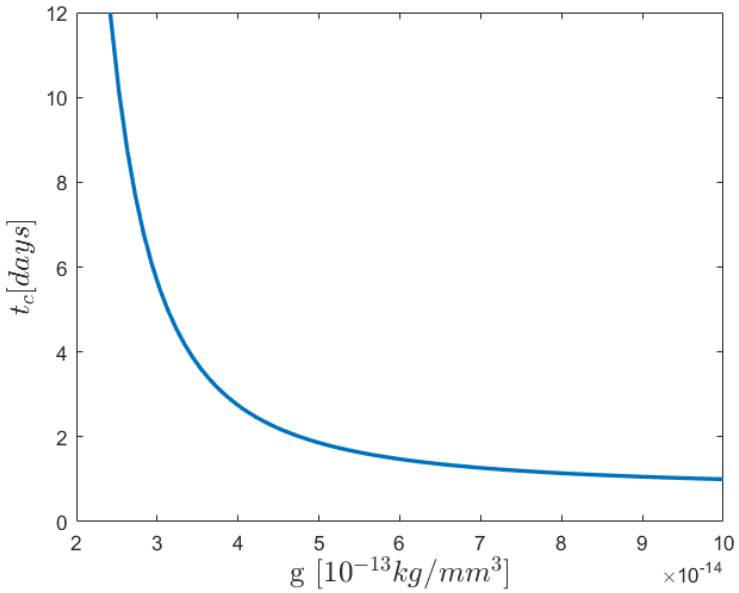

Figure 2.5: Cell division time for $\overline{g} = 1 \cdot 10^{-13}$ kg/mm^3 and $\tau = 12$ h

$$\mathbb{K}^{rand}_{ECM}(\mathbf{x}) = \mathbf{I} + k_{an}(\mathbf{x})\mathbb{K}^{an}_{ECM}(\mathbf{x}). \tag{2.67}$$

The term $\mathbb{K}^{an}_{ECM}(\mathbf{x})$ contains all the informations about the deviation from the isotropic behaviour and $k_{an}(\mathbf{x})$ is the weight of the anisotropic contribution.
More specifically, $\mathbb{K}^{an}_{ECM}(\mathbf{x})$ assumes the following form

$$\mathbb{K}^{an}_{ECM}(\mathbf{x}) = \begin{bmatrix} -k_2(\mathbf{x})^2 - k_3(\mathbf{x})^2 & k_1(\mathbf{x})k_2(\mathbf{x}) & k_1(\mathbf{x})k_3(\mathbf{x}) \\ k_1(\mathbf{x})k_2(\mathbf{x}) & -k_1(\mathbf{x})^2 - k_3(\mathbf{x})^2 & k_2(\mathbf{x})k_3(\mathbf{x}) \\ k_1(\mathbf{x})k_3(\mathbf{x}) & k_2(\mathbf{x})k_3(\mathbf{x}) & -k_1(\mathbf{x})^2 - k_2(\mathbf{x})^2 \end{bmatrix}, \tag{2.68}$$

where the parameters $k_i(\mathbf{x})$, $i = 1,2,3$ and $k_{an}(\mathbf{x})$ are randomly chosen for each position in space, such that

$$\sum_{i=1}^{3} k_i(\mathbf{x})^2 = 1 \quad \text{and} \quad k_{an}(\mathbf{x}) \in [0,1]. \tag{2.69}$$

Branching

tip cells are not only subjected to chemotactic-induced movement, but they may also undergo branching: this phenomenon consists in the formation of two different sprouts, starting from a pre-existing one.
Furthermore, new tip cells may arise from stalk-to-tip conversion just behind the vessel tip, resulting in two tip cells migrating in different directions and thereby initiating the formation of a new branch.

In particular, according to [3, 25], in our model we allow the birth of new sprouts if the following two conditions are both satisfied:

1. the current sprout is old enough, i.e. its age is greater than a threshold age τ_{br},
2. $\frac{||\mathbf{w}_\Pi||}{||\mathbf{w}||} > \alpha_{br}^{\mathbf{w}}$, i.e. the ratio between the norm of the orthogonal projection of $\mathbf{w}$ on the plane Π (perpendicular to the current sprout) and the norm of $\mathbf{w}$ must be greater than a threshold value $\alpha_{br}^{\mathbf{w}}$.

Moreover, since the splitting may happen or not based on the available concentration of VEGF, according to [3] we also introduce a branching probability such that tips are more likely to branch when VEGF concentration is high.
In this work, the following probability has been chosen

$$P_{br} = \begin{cases} \dfrac{1}{1 + \exp\left(-a(g - bg_{br})\right)} & g < g_{br} \\ 1 & \text{otherwise.} \end{cases} \tag{2.70}$$

with $a = 20$ mm^3/kg and $b = 1/2$ and whose shape is the same proposed in [3], but this novel formulation is more compatible with values of τ_{br} close to the minimum of $t_c(g)$.

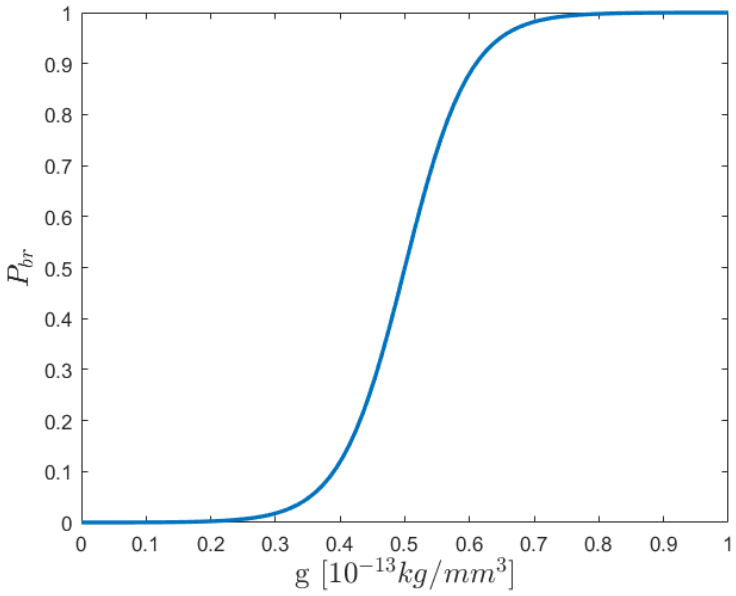

Figure 2.6: Branching probability for $g_{br} = 1 \cdot 10^{-13}$ kg/mm^3

It is also important to specify that, as one can read in equation (2.66), it is counter-intuitive choosing values of τ_{br} lower than the minimum of $t_c(g)$.
The branching probability for $g_{br} = 1 \cdot 10^{-13}$ kg/mm^3 is then reported in Figure (2.70).

Now, assuming that the branching conditions described above are both satisfied and that the probability effectively allows branching to occur, then the division of the parent sprout generates two new extensions, whose direction must be defined.

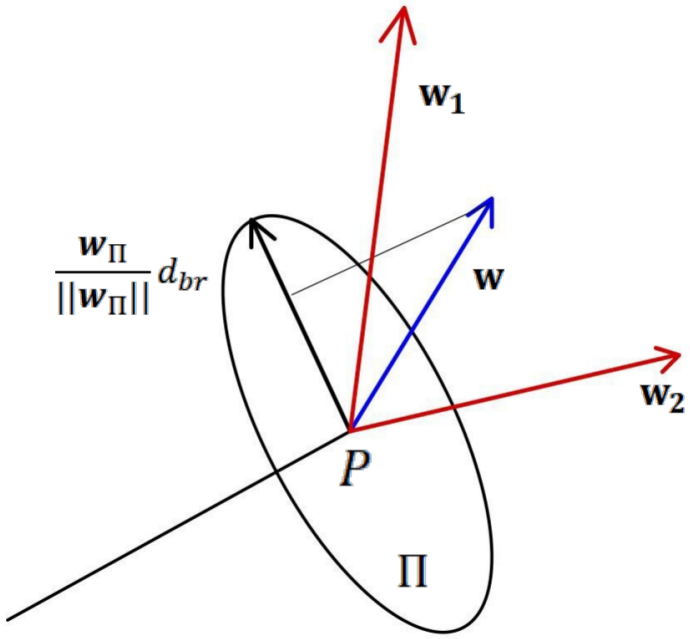

Figure 2.7: Branching directions

To this purpose, let us consider the generic sprout $P \in \mathcal{P}^k$, the plane Π orthogonal to its orientation and $\mathbf{w}_\Pi$ the orthogonal projection of $\mathbf{w}$ on the plane Π.
We can compute the directions of the new sprouts as follows

$$\mathbf{w}_1 = \mathbf{w} + \frac{\mathbf{w}_\Pi}{||\mathbf{w}_\Pi||} d_{br}, \qquad \mathbf{w}_2 = \mathbf{w} - \frac{\mathbf{w}_\Pi}{||\mathbf{w}_\Pi||} d_{br} \tag{2.71}$$

where d_{br} is a function of the diameter of the capillary, as shown in figure (2.7).

Anastomosis

The last possible outcome for tip cells is the formation of loops and this phenomenon is called anastomosis.
Also in this case, the model is the same proposed in [3] and we report it for completeness. In particular, anastomosis occurs whenever two sprouts get together or when a sprout encounters a portion of another sprout that is not older than threshold age τ_{an}.
To be more precise, the first case is called *tip-to-tip* anastomosis and it produces the deactivation of both tip cells.

The second case, instead, is called *tip-to-sprout* anastomosis and it leads to the deactivation of only one of the two tips.
In the simulations we force anastomosis when the distance between two tips or the distance between a tip and a sufficiently young sprout is lower than a value d_{an}.

Chapter 3

The mathematical model for vascular tumour growth with angiogenesis

3.1 The optimization based domain decomposition for 3D-1D coupling

As shown in the previous sections, pressure and oxygen problems need to be solved taking into account the coupling between the tissue and the network.
In particular, since the radius of the blood vessel is much smaller than the dimension of the whole domain, the network can be considered as a one-dimensional object embedded in a three-dimensional one.
Given that, the formulation of a well-posed numerical formulation for this kind of problem is not trivial, since no bounded trace operator is defined when the involved manifolds have a dimensionality gap higher than one [3].
Actually, it is possible to overcome this obstacle defining appropriate Sobolev subspaces to obtain the variational formulation of the problem [2, 4, 20].
The main idea is the to apply a domain domain decomposition strategy that allows to introduce a suitable cost functional. Then we implement the optimization method presented in [4], in which not only no bounded trace operator but also no mesh conformity is required, and consequently it allows to deal with complex time-varying geometries.

3.1.1 The variational formulation

The oxygen problem

In this section, we focus on the oxygen problem, since the presence in this problem of time derivation, advection and reaction terms allows us to give a complete description of the strategy. Similar considerations still apply for simpler elliptic problems such as the pressure one.

We underline the fact that all the following consideration are reported in [3] and we show them for completeness.
The first step is to define the proper spaces for the solution and, for this reason, let us consider $t \in \mathcal{I}_k = (t_{k-1}, t_k]$ and define some important spaces and operators.

- The space of continuous functions on Λ^k whose restriction to Λ_i^k is in $H^1(\Lambda_i^k)$

$$H^1(\Lambda^k) = \prod_{i \in Y^k} H^1(\Lambda_i^k) \cap C^0(\Lambda^k).$$

  Each function $\hat{u} \in H^1(\Lambda^k)$ can be written as

$$\hat{u} = \prod_{i \in Y^k} \hat{u}_i, \quad \hat{u}_i \in H^1(\Lambda_i^k).$$

- The trace operator

$$\gamma_i^k : H^1(\mathcal{D}^k) \cup H^1(\Sigma_i^k) \to H^{1/2}(\Gamma_i^k),$$

  which, given $u \in H^1(\mathcal{D}^k) \cup H^1(\Sigma_i^k)$ returns

$$\gamma_i^k u_i = u_{|\Gamma_i^k}, \quad i \in Y^k.$$

- The extension operator

$$\mathcal{E}_i^k : H^1(\Lambda_i^k) \to H^{1/2}(\Gamma_i^k),$$

  which, given $\hat{u}_i \in H^1(\Lambda_i^k)$ uniformly extends the value of $\hat{u}_i(s)$ to the boundary $\Gamma_i^k(s)$ of the transversal section $\Sigma_i^k(s)$, i.e.

$$\mathcal{E}_i^k \hat{u}_i(s) = \tilde{u}(\mathbf{x}) \qquad \forall \mathbf{x} \in \Gamma_i^k(s).$$

- The extension operator

$$\Theta_i^k : H^1(\Lambda_i^k) \to H^1(\Sigma_i^k),$$

  which given $\hat{u}_i \in H^1(\Lambda_i^k)$ uniformly extends its value to the cross section $\Sigma_i^k(s)$ of the cylinder, i.e.

$$\Theta_i^k \hat{u}_i(s) = \tilde{u}(\mathbf{x}), \qquad \forall \mathbf{x} \in \Sigma_i^k(s).$$

- The spaces

$$\hat{V}_0^k = \left\{ \hat{u} \in H^1(\Lambda^k) : \hat{u}_{|\Lambda_{in}} = 0 \right\}, \quad \hat{V}^k = \left\{ \hat{u} \in H^1(\Lambda^k) : \hat{u}_{|\Lambda_{in}} = \hat{c}_{in} \right\};$$

$$\mathcal{H}_i^{\Gamma_k} = \Big\{ u \in H^{1/2}(\Gamma_i^k) : u = \mathcal{E}_i^k \hat{u}_i,\ \hat{u} \in \hat{V}^k \Big\},$$

$$V^k = \Big\{ u \in H^1(\mathcal{D}^k) : \gamma_i^k u \in \mathcal{H}_i^{\Gamma_k},\ \forall i \in Y^k \Big\},$$

$$\tilde{V}_i^k = \Big\{ u \in H^1(\Sigma_i^k) : u = \Theta_i^k \hat{u}_i,\ \hat{u} \in \hat{V}^k \Big\}.$$

Now, let us consider the oxygen variables for the tissue and for the network, respectively chosen as

$$c(t) \in V^k \qquad \text{and} \qquad \tilde{c}(t) = \prod_{i \in Y^k} \tilde{c}_i(t), \quad \tilde{c}_i(t) \in \tilde{V}_i^k. \tag{3.1}$$

Furthermore, according to (2.41)-(2.42) we introduce the following variables

$$\check{c}(t) \in \hat{V}^k \quad \text{such that} \quad \gamma_i^k c(t) = \mathcal{E}_i^k \check{c}_i(t) \tag{3.2}$$

and

$$\hat{c}(t) \in \hat{V}^k \quad \text{such that} \quad \tilde{c}(t)(\mathbf{x}) = \Theta_i^k \hat{c}_i(t) \quad \forall \mathbf{x} \in \Sigma_i^k. \tag{3.3}$$

It is finally possible to provide the variational formulation of the 3D-1D oxygen problem, that reads as:
$\forall t \in \mathcal{I}_k$, *find* $c(t) \in V^k$ *and* $\hat{c}(t) \in \hat{V}^k$ *such that*

$$\begin{aligned}
&\left(\frac{\partial c}{\partial t}, \eta\right)_{L^2(\mathcal{D}^k)} + \Big(D_c \nabla c, \nabla \eta\Big)_{L^2(\mathcal{D}^k)} + \Big(\mathbf{v} \cdot \nabla c, \eta\Big)_{L^2(\mathcal{D}^k)} + \Big(\mathbf{M}_c c, \eta\Big)_{L^2(\mathcal{D}^k)} + \\
&+ \Big(\beta_c^{ext} c, \eta\Big)_{L^2(\partial\mathcal{D})} + \sum_{i \in Y^k} \Big(2\pi R \beta_c (\check{c}_i - \hat{c}_i), \check{\eta}_i\Big)_{L^2(\Lambda_i^k)} \\
&= \Big(\beta_c^{ext} c_{ext}, \eta\Big)_{L^2(\partial\mathcal{D})} \quad \forall \eta \in V^k : \gamma_i^k \eta = \mathcal{E}_i^k \check{\eta}_i,\ \check{\eta} \in \hat{V}_0^k
\end{aligned} \tag{3.4}$$

$$\begin{aligned}
&\sum_{i \in Y^k} \left[\left(\pi R^2 \frac{\partial \hat{c}_i}{\partial t}, \hat{\eta}_i\right)_{L^2(\Lambda_i^k)} + \left(\pi R^2 \tilde{D}_c \frac{\partial \hat{c}_i}{\partial s}, \frac{\partial \hat{\eta}_i}{\partial s}\right)_{L^2(\Lambda_i^k)} + \right. \\
&\left. + \left(\pi R^2 \hat{v}_i \frac{\partial \hat{c}_i}{\partial s}, \hat{\eta}_i\right)_{L^2(\Lambda_i^k)} + \Big(2\pi R \beta_c (\hat{c}_i - \check{c}_i), \hat{\eta}_i\Big)_{L^2(\Lambda_i^k)} \right] = 0 \qquad \forall \hat{\eta} \in \hat{V}_0^k.
\end{aligned} \tag{3.5}$$

Then, the aim is to apply the domain decomposition strategy presented in [4], in which two auxiliary variables are introduced at the interface to formally decouple the problems related to the vascular network and the tissue dynamics.

More specifically, these two variables are here denoted by $\hat{\psi}^D(t)$ and $\hat{\psi}^\Sigma(t)$ and they allow us to reformulate the problems (3.4)-(3.5) in the following equivalent manner:

$$\begin{aligned}
&\forall t \in \mathcal{I}_k, \quad find \;\; c(t) \in V^k, \;\; \hat{c}(t) \in \hat{V}_c^k, \;\; \hat{\psi}^D(t) \in \hat{V}^k, \;\; \hat{\psi}^\Sigma(t) \in \hat{V}^k \;\; such\ that \\
&\left(\frac{\partial c}{\partial t}, \eta\right)_{L^2(\mathcal{D}^k)} + \left(D_c \nabla c, \nabla \eta\right)_{L^2(\mathcal{D}^k)} + \left(\mathbf{v} \cdot \nabla c, \eta\right)_{L^2(\mathcal{D}^k)} + \left(\mathbf{M}_c c, \eta\right)_{L^2(\mathcal{D}^k)} + \\
&+ \left(\beta_c^{ext} c, \eta\right)_{L^2(\partial\mathcal{D})} + \sum_{i \in Y^k} \left(2\pi R \beta_c \check{c}_i, \check{\eta}_i\right)_{L^2(\Lambda_i^k)} - \sum_{i \in Y^k} \left(2\pi R \beta_c \hat{\psi}_i^\Sigma, \check{\eta}_i\right)_{L^2(\Lambda_i^k)} = \\
&= \left(\beta_c^{ext} c_{ext}, \eta\right)_{L^2(\partial\mathcal{D})} \quad \forall \eta \in V^k : \gamma_i^k \eta = \mathcal{E}_i^k \check{\eta}_i, \;\; \check{\eta} \in \hat{V}_0^k
\end{aligned} \tag{3.6}$$

$$\begin{aligned}
&\sum_{i \in Y^k} \left[\left(\pi R^2 \frac{\partial \hat{c}_i}{\partial t}, \hat{\eta}_i\right)_{L^2(\Lambda_i^k)} + \left(\pi R^2 \tilde{D}_c \frac{\partial \hat{c}_i}{\partial s}, \frac{\partial \hat{\eta}_i}{\partial s}\right)_{L^2(\Lambda_i^k)} + \left(\pi R^2 \hat{v}_i \frac{\partial \hat{c}_i}{\partial s}, \hat{\eta}_i\right)_{L^2(\Lambda_i^k)} \right. \\
&\left. + \left(2\pi R \beta_c \hat{c}_i, \hat{\eta}_i\right)_{L^2(\Lambda_i^k)} - \left(2\pi R \beta_c \hat{\psi}_i^D, \hat{\eta}_i\right)_{L^2(\Lambda_i^k)} \right] = 0 \qquad \forall \hat{\eta} \in \hat{V}_0^k.
\end{aligned} \tag{3.7}$$

with interface conditions, $\forall i \in Y^k$

$$\left\langle \check{c}_i(t) - \hat{\psi}_i^D(t), \hat{\mu}_i \right\rangle_{\hat{V}_0^k, \hat{V}_0^{k'}} = 0 \qquad \forall \hat{\mu}_i \in \hat{V}_0^{k'}, \;\; t \in \mathcal{I}_k \tag{3.8}$$

$$\left\langle \hat{c}_i(t) - \hat{\psi}_i^\Sigma(t), \hat{\mu}_i \right\rangle_{\hat{V}_0^k, \hat{V}_0^{k'}} = 0 \qquad \forall \hat{\mu}_i \in \hat{V}_0^{k'}, \;\; t \in \mathcal{I}_k \tag{3.9}$$

and with $\hat{V}_0^{k'}$ being the dual space of the space $\hat{V}_0^k$.
The final step is to rewrite the original problem into a PDE-constrained optimization one and, in this perspective, we introduce the cost functional

$$J^k\left(\hat{\psi}^D(t), \hat{\psi}^\Sigma(t)\right) = \frac{1}{2} \sum_{i \in Y^k} \left(||\check{c}_i(t) - \hat{\psi}_i^D(t)||^2_{L^2(\Lambda_i^k)} + ||\hat{c}_i(t) - \hat{\psi}_i^\Sigma(t)||^2_{L^2(\Lambda_i^k)} \right) \tag{3.10}$$

representing the error committed when we approximate $\hat{c}(t)$ and $\check{c}(t)$ by $\hat{\psi}^\Sigma(t)$ and $\hat{\psi}^D(t)$.
So, in conclusion, the variational formulation of (3.10) reads:
$\forall t \in \mathcal{I}_k$

$$\min_{\hat{\psi}^D(t), \hat{\psi}^\Sigma(t) \in \hat{V}^k} J^k\left(\hat{\psi}^D(t), \hat{\psi}^\Sigma(t)\right) \quad \text{subject to} \quad (3.6) - (3.7) \tag{3.11}$$

The VEGF problem

As previously mentioned, since there is no flux of VEGF through the vessel walls, the problem is only formulated in a tridimensional framework and the interaction between the chemotactic growth factor and the network is expressed through a singular sink term.

For this reason, a 3D-1D coupling approach is unnecessary but we nevertheless provide the variational formulation because it will be further adopted for the matrix discretization. In particular, it reads as follows:

Find $g(t) \in V^k$ *such that*

$$\begin{cases} \left(\dfrac{\partial g}{\partial t}, \eta\right)_{L^2(D^k)} + \left(D_g \nabla g, \nabla \eta\right)_{L^2(D^k)} + \left(\mathbf{v} \cdot \nabla g, \eta\right)_{L^2(D^k)} + \left(\sigma g, \eta\right)_{L^2(D^k)} + \\ + \displaystyle\sum_{i \in Y^k} \left(2\pi R \check{\sigma} \check{g}_i, \check{\eta}_i\right)_{L^2(\Lambda_i^k)} = \left(f_g, \eta\right)_{L^2(D^k)} \quad \forall \eta \in V^k : \gamma_i^k \eta = \mathcal{E}_i^k \check{\eta},\ \check{\eta} \in H^1(\Lambda^k) \\ g(0) = g_0 \end{cases} \tag{3.12}$$

where $\gamma_i^k g(t) = \mathcal{E}_i^k \check{g}_i(t)$

3.2 Problem discretization

As mentioned in Section 3.1, since the 3D-3D coupled formulation can be reduced into a 3D-1D one, we can extend the tridimensional domain $\mathcal{D}^k$ to the whole Ω and discretize it with a tetrahedral mesh $\mathcal{T}$. This mesh is independent from the vessel network Λ^k, on which we assemble three different partitions: $\hat{\mathcal{T}}^k$, τ_D^k and τ_Σ^k, each one independent from the others and from $\mathcal{T}$. Such meshes could change at each time-step, but instead of re-meshing the whole network at every single iteration, we incrementally add new elements to the previous in order to ensure computational efficiency.
Moreover, to guarantee mesh uniformity, a minimum element size can be fixed.
Now we introduce some notation that will be useful for the matrix formulation, more specifically, for the tridimensional quantities, we denote:

- the number of DOFs of the discrete approximation of $c(t)$ inside Ω as N,
- the linear Lagrangian basis function on Ω as
$$\{\varphi_j\}_{j=1}^N,$$
- the discrete approximations of $c(t)$ as
$$C(t) = \sum_{j=1}^N C_j(t)\varphi_j.$$

For the mono-dimensional ones, instead, we denote

- the number of DOFs at time t_k of the discrete approximation of $\hat{c}(t)$, $\hat{\psi}^D$ and $\hat{\psi}^\Sigma$ as $\hat{N}^k$, $\hat{N}_D^k$ and $\hat{N}_\Sigma^k$ respectively,
- the linear Lagrangian basis function on $\hat{\mathcal{T}}^k$, τ_D^k and τ_Σ^k respectively as
$$\{\hat{\varphi}_j\}_{j=1}^{\hat{N}^k}, \quad \{\hat{\theta}_j^D\}_{j=1}^{\hat{N}_D^k} \quad \text{and} \quad \{\hat{\theta}_j^\Sigma\}_{j=1}^{\hat{N}_\Sigma^k},$$

- the discrete approximations of $\hat{c}(t)$, $\hat{\psi}^D(t)$ and $\hat{\psi}^\Sigma(\mathrm{t})$ respectively as

$$\hat{C}(t) = \sum_{j=1}^{\hat{N}^k} \hat{C}_j(t)\hat{\varphi}_j, \quad \hat{\Psi}^D(t) = \sum_{j=1}^{\hat{N}_D^k} \hat{\Psi}_j^D(t)\theta_j^D \quad \text{and} \quad \Psi^\Sigma(t) = \sum_{j=1}^{\hat{N}_\Sigma^k} \Psi_j^\Sigma(t)\theta_j^\Sigma. \tag{3.13}$$

With reference to the variational formulation of the oxygen problem presented in Section 3.1, let us consider the following matrices and vector definitions for the semi-discretization in space:

$$\begin{aligned}
&\mathbf{A}^k \in \mathbb{R}^{N\times N} \text{ s.t. } A_{l,j}^k = \int_\Omega \Big(D_c\nabla\varphi_j\cdot\nabla\varphi_l + (\mathbf{v}\cdot\nabla\varphi_j)\varphi_l + m_c\varphi_j\varphi_l\Big)d\omega + \\
&\qquad\qquad + \int_{\partial\Omega} \beta_c^{ext}\varphi_{j_{|\partial\Omega}}\varphi_{l_{|\partial\Omega}}d\sigma + \int_{\Lambda^k} 2\pi R\beta_c\varphi_{j_{|\Lambda^k}}\varphi_{l_{|\Lambda^k}}ds, \\
&\hat{\mathbf{A}}^k \in \mathbb{R}^{\hat{N}^k\times\hat{N}^k} \text{ s.t. } \hat{A}_{l,j}^k = \int_{\Lambda^k} \Big(\pi R^2\tilde{D}_c\,\frac{d\hat{\varphi}_j}{ds}\frac{d\hat{\varphi}_l}{ds} + \pi R^2\hat{v}\frac{d\hat{\varphi}_j}{ds}\hat{\varphi}_l\Big)ds + \\
&\qquad\qquad + \int_{\Lambda^k} 2\pi R\beta_c\hat{\varphi}_j\hat{\varphi}_l ds, \\
&\mathbf{M} \in \mathbb{R}^{N\times N} \text{ s.t. } M_{l,j} = \int_\Omega \varphi_j\varphi_l d\omega, \\
&\hat{\mathbf{M}}^k \in \mathbb{R}^{\hat{N}\times\hat{N}} \text{ s.t. } \hat{M}_{l,j}^k = \int_\Omega \pi R^2\hat{\varphi}_j\hat{\varphi}_l ds, \\
&\hat{\mathbf{D}}_\beta^k \in \mathbb{R}^{\hat{N}\times\hat{N}_D^k} \text{ s.t. } (\hat{D}_\beta^k)_{lj} = \int_{\Lambda^k} 2\pi R\beta_c\hat{\varphi}_l\theta_j^D ds, \\
&\mathbf{S}_\beta^k \in \mathbb{R}^{\hat{N}\times\hat{N}_\Sigma^k} \text{ s.t. } (\hat{S}_\beta^k)_{lj} = \int_{\Lambda^k} 2\pi R\beta_c\hat{\varphi}_{l_{|\Lambda^k}}\theta_j^\Sigma ds, \\
&\mathbf{F} \in \mathbb{R}^N \text{ s.t. } F_l = \int_{\partial\Omega} \beta_c^{ext}\varphi_l d\sigma.
\end{aligned}$$

On the other hand, for the time discretization we adopted the backward Euler method, on a uniform partition of the time interval $\mathcal{I}_k$ with a step $\Delta t \le \Delta\mathcal{I}_k$ such that

$$t_{k,q} = t_{k-1} + q\Delta t, \quad q \ge 0.$$

Summarizing, here follows the fully discretized version of the equations (3.6)-(3.7):

$$\begin{cases} (\mathbf{M}+\Delta t\mathbf{A}^k)C(t_{k,q})-\Delta t\mathbf{S}^k_\beta\Psi_\Sigma(t_{k,q})=\mathbf{M}C(t_{k,q-1})+\Delta tF \\ (\hat{\mathbf{M}}^k+\Delta t\hat{\mathbf{A}}^k)\hat{C}(t_{k,q})-\Delta t\hat{\mathbf{D}}^k_\beta\Psi_D(t_{k,q})=\hat{\mathbf{M}}^k\hat{C}(t_{k,q-1}) \\ C(t_{k,0})=\begin{cases} C_0 & \text{if } k=0 \\ C(t_{k-1}) & \text{if } k>0 \end{cases} \\ \hat{C}(t_{k,0})=\begin{cases} \hat{C}_0 & \text{if } k=0 \\ \hat{C}_\sharp(t_{k-1}) & \text{if } k>0 \end{cases} \end{cases} \tag{3.14}$$

where $\hat{C}_\sharp(t_{k-1})$ is the extension of $\hat{C}(t_{k-1})\in\mathbb{R}^{\hat{N}^{k-1}}$ to $\mathbb{R}^{\hat{N}^k}$. In particular, $\hat{C}_\sharp(t_{k-1})$ is a vectors whose elements are null in correspondence of DOFs defined on $\Lambda^k\backslash\Lambda^{k-1}$.
At this point, we just provided the discretization of the PDE-problem described in the section above, but in the same section we also introduced the cost functional (3.10) that allows us to recast the original problem into a PDE-constrained one. So, it is now necessary to provide the discrete formulation of (3.10) and to this aim we have to build the following matrices:

$$\mathbf{G}^k\in\mathbb{R}^{N\times N}\text{ s.t. }G^k_{l,j}=\int_{\Lambda^k}\varphi_{j_{|\Lambda^k}}\varphi_{l_{|\Lambda^k}}ds,$$

$$\hat{\mathbf{G}}^k\in\mathbb{R}^{\hat{N}^k\times\hat{N}^k}\text{ s.t. }\hat{G}^k_{l,j}\int_{\Lambda^k}\hat{\varphi}_j\hat{\varphi}_l ds,$$

$$\mathbf{D}^k\in\mathbb{R}^{N\times\hat{N}^k_D}\text{ s.t. }D^k_{l,j}=\int_{\Lambda^k}\hat{\varphi}_{l_{|\Lambda^k}}\theta^D_j ds,$$

$$\hat{\mathbf{S}}^k\in\mathbb{R}^{N\times\hat{N}^k_\Sigma}\text{ s.t. }\hat{S}^k_{l,j}=\int_{\Lambda^k}\hat{\varphi}_l\theta^\Sigma_j ds,$$

$$\mathbf{G}^k_D\in\mathbb{R}^{\hat{N}^k_D\times\hat{N}^k_D}\text{ s.t. }(G^k_D)_{l,j}=\int_{\Lambda^k}\theta^D_j\theta^D_l ds,$$

$$\mathbf{G}^k_\Sigma\in\mathbb{R}^{\hat{N}^k_\Sigma\times\hat{N}^k_\Sigma}\text{ s.t. }(G^k_\Sigma)_{l,j}=\int_{\Lambda^k}\theta^\Sigma_j\theta^\Sigma_l ds.$$

At this point, all the above definitions allow us to write the discrete formulation of the cost functional at time $t_{k,q}$:

$$\begin{aligned}\tilde{\mathbf{J}}^{k,q}=&\frac{1}{2}\Big(C(t_{k,q})^T\mathbf{G}^kC(t_{k,q})-C(t_{k,q})^T\mathbf{D}^k\Psi_D(t_{k,q})-\Psi^T_D(t_{k,q})(\mathbf{D}^k)^TC(t_{k,q})+\\&+\Psi_D(t_{k,q})^T\mathbf{G}^k_D\Psi_D(t_{k,q})+\hat{C}(t_{k,q})^T\hat{\mathbf{G}}^k\hat{C}(t_{k,q})-\hat{C}(t_{k,q})^T\hat{\mathbf{S}}^k\Psi_\Sigma(t_{k,q})+\\&-\Psi_\Sigma(t_{k,q})^T(\hat{\mathbf{S}}^k)^T\hat{C}(t_{k,q})+\Psi_\Sigma(t_{k,q})^T\mathbf{G}^k_\Sigma\Psi_\Sigma(t_{k,q})\Big),\end{aligned} \tag{3.15}$$

then we can finally formulate the saddle-point system

$$\boldsymbol{\mathcal{K}}^k \begin{bmatrix} C(t_k) \\ \hat{C}(t_{k,q}) \\ \Psi_D(t_{k,q}) \\ \Psi_\Sigma(t_{k,q}) \\ -\Pi(t_{k,q}) \\ -\hat{\Pi}(t_{k,q}) \end{bmatrix} = \begin{bmatrix} 0 \\ 0 \\ 0 \\ 0 \\ \mathbf{M}C(t_{k,q-1}) + \Delta t F \\ \hat{\mathbf{M}}\hat{C}(t_{k,q-1}) \end{bmatrix} \tag{3.16}$$

that collects the first order optimality conditions for problem (3.15) constrained by (3.14) and we can solve it at each time-step.
More specifically, matrix $\mathcal{K}$ is given by

$$\boldsymbol{\mathcal{K}}^k = \begin{bmatrix} \mathbf{G}^k & \mathbf{0} & -\mathbf{D}^k & \mathbf{0} & (\Delta t \mathbf{A}^k + \mathbf{M}^k)^T & \mathbf{0} \\ \mathbf{0} & \hat{\mathbf{G}}^k & \mathbf{0} & -\hat{\mathbf{S}}^k & \mathbf{0} & (\Delta t \hat{\mathbf{A}}^k + \hat{\mathbf{M}}^k)^T \\ -(\mathbf{D}^k)^T & \mathbf{0} & \mathbf{G}_D^k & \mathbf{0} & \mathbf{0} & -\Delta t (\mathbf{D}_\beta^k)^T \\ \mathbf{0} & -(\hat{\mathbf{S}}^k)^T & \mathbf{0} & \mathbf{G}_\Sigma^k & -\Delta t (\mathbf{S}_\beta^k)^T & \mathbf{0} \\ \Delta t \mathbf{A}^k + \mathbf{M}^k & \mathbf{0} & \mathbf{0} & -\Delta t \mathbf{S}_\beta^k & \mathbf{0} & \mathbf{0} \\ \mathbf{0} & \Delta t \hat{\mathbf{A}}^k + \hat{\mathbf{M}}^k & -\Delta t \mathbf{D}_\beta^k & \mathbf{0} & \mathbf{0} & \mathbf{0} \end{bmatrix},$$

while $\Pi(t_{k,q})$, $\hat{\Pi}(t_{k,q})$ are the vector of DOFs of Lagrange multipliers.
To conclude, as proved in [4], matrix $\mathcal{K}$ is non-singular and the unique solution of (3.16) is equivalent to the solution of the optimization problem (3.11).

3.2.1 The VEGF discrete problem

Let us consider now the chemotactic growth factor problem, that is simpler than the oxygen one since no VEGF flux across the vessel wall exists, so we do not have to resolve any 3D-1D coupled problem.
Our aim is to build the finite element discretization for VEGF problem and we can obtain it considering a tetrahedral mesh $\mathcal{T}$ on domain Ω and defining the linear Lagrangian basis functions $\{\varphi_j\}_{j=1}^{N_G}$ on such mesh.
In this way, the discrete approximation of the variable $g(t)$ reads as

$$G(t) = \sum_{j=1}^{N_G} G_k(t)\varphi_j,$$

with N_G being the number of degrees of freedom.
Now, we define the matrices:

$$\mathbf{B}^k \in \mathbb{R}^{N_G \times N_G} \text{ s.t. } B^k_{l,j} = \int_\Omega D_g \nabla\varphi_j \cdot \nabla\varphi_l d\omega + \int_\Omega (\mathbf{v}\cdot\nabla\varphi_j)\varphi_l d\omega,$$
$$+ \int_\Omega \sigma\varphi_j\varphi_l d\omega + \int_{\Lambda^k} 2\pi R\tilde{\sigma}\varphi_{j_{|\Lambda^k}}\varphi_{l_{|\Lambda^k}} ds$$
$$\mathbf{H} \in \mathbb{R}^{N_G \times N_G} \text{ s.t. } H_{l,j} = \int_\Omega \varphi_j\varphi_l d\omega,$$

such that the semi-discretization in space reads as

$$\begin{cases} \mathbf{H}\partial_t G(t) + \mathbf{B}^k G(t) = 0 \quad t \in \mathcal{I}_k \\ G(0) = G_0. \end{cases} \tag{3.17}$$

For time discretization, also in this case we choose to adopt the backward Euler scheme, with a uniform partition of $\mathcal{I}_k$ such that $\Delta t \leq \Delta\mathcal{I}_k$ and

$$t_{k,q} = t_{k-1} + q\Delta t, \quad q \geq 0.$$

The following system is then solved at each time-step to obtain the required solution

$$\begin{cases} (\mathbf{H} + \Delta t\mathbf{B}^k)G(t_{k,q}) = \mathbf{H}G(t_{k,q-1}) \quad k > 0 \\ G(t_{k,0}) = \begin{cases} G_0 & \text{if } k = 0 \\ G(t_{k-1}) & \text{if } k > 0. \end{cases} \end{cases} \tag{3.18}$$

3.2.2 The capillary growth discretization and the virtual growth

Lastly, we provide the discretization of the growing capillary network starting from equation (2.64) and applying the forward Euler method on it.
The relation in (2.64) shows a dependence of the tip cell position from the vascular growth factor, so once $G(t_k)$ is computed, $\mathbf{x}_p$ is updated as follows

$$\mathbf{x}_p(t_{k+1}) = \mathbf{x}_p(t_k) + \Delta t_{k+1}\mathbf{w}(G(t_k), \mathbf{x}_p(t_k)), \quad \forall P \in \mathcal{P}^k. \tag{3.19}$$

Since the capillary network is represented by sets of connected segments in the 3D space, the points $\mathbf{x}_p(t_{k+1})$ and $\mathbf{x}_p(t_k)$ should be joined by a line.
In this work, differently from [3], we introduce the implementation of a so called "*virtual growth*". The distance between $\mathbf{x}_p(t_{k+1})$ and $\mathbf{x}_p(t_k)$ could be very small, so it is not convenient to update the position of the tip cells at each time step, because such distance may be lower than the characteristic dimension of the single endothelial cell and this is not coherent with the biological evidences.
Moreover, the virtual growth is also useful to reduce the dependence of the network morphology from the time-step adopted to the Euler method, as we will show in the following section.

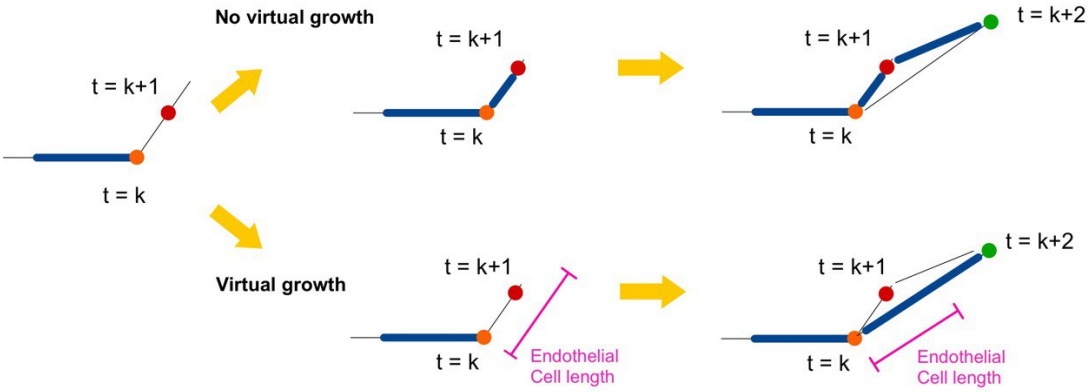

Figure 3.1: Representation of the virtual growth criterion functioning.

To be more precise, in Figure (3.1) we report a simplified representation of the virtual growth functioning, showing the different morphologies obtained with and without its implementation.
More specifically, at each time iteration we evaluate the quantity $\mathbf{x}_p(t_{k+1}) - \mathbf{x}_p(t_k)$ and, if it is lower than a threshold value l_e, which represents the characteristic dimension of the single endothelial cell, we do not update the position of the current tip cell, but we only keep track of it. In the following iteration, we evaluate again the distance between the new (virtual) position and the last physical one, repeating the process until the value l_e is reached. Only at this point, the position of the current tip cell $\mathbf{x}_p(t_{k+1})$ is updated.
Furthermore, even if branching can occur also when the current tip cell belongs to a virtual position, we do not allow the formation of two virtual sprouts, but we only keep track of the fact that the network can undergo branching.
Finally, when we update the position of the current tip cell, we also let the the network produce two sprouts considering the plane Π orthogonal to the last segment involved by the virtual growth. We compute the orthogonal projection $\mathbf{w}_\Pi$ of $\mathbf{w}(G(t_k), \mathbf{x}_p(t_k))$, obtaining the branching directions $\mathbf{w}_1$ and $\mathbf{w}_2$, that allow to split equation (3.19) into

$$\mathbf{x}_p^{(1)}(t_{k+1}) = \mathbf{x}_p(t_k) + \Delta t_{k+1}\mathbf{w}_1, \qquad \mathbf{x}_p^{(2)}(t_{k+1}) = \mathbf{x}_p(t_k) + \Delta t_{k+1}\mathbf{w}_2. \tag{3.20}$$

To conclude, once the new positions of the tip cells have been computed, we update the network in the following manner

$$\Lambda^{k+1} = \Lambda^k \cup \bigcup_{\substack{P\in\mathcal{P}^k;\\ i=1,2}} \left[x_P^{(i)}(t_{k+1}), x_P(t_k)\right] \tag{3.21}$$

gaining the fixed geometry on which all the other quantities will evolve for $t \in \mathcal{I}_{k+1}$.
We also specify the fact that, even if we decided to implemented the virtual growth criterion, many other different choice could have been introduced.

Chapter 4

Numerical Simulations

4.1 The setting

In this section we provide some numerical simulations using the proposed approach.
To this aim, we consider a cubic domain with an edge length of $L = 0.5$ mm and we denote it as $\Omega = [0, L]$.
Successively, we place a small initial vascular network with two inlets and two outlets inside the above domain, as sown in the left panel of Figure (4.1). We suppose that the blood vessel radius is fixed both in time and space and its value is set to $R = 5 \cdot 10^{-3}$ mm.

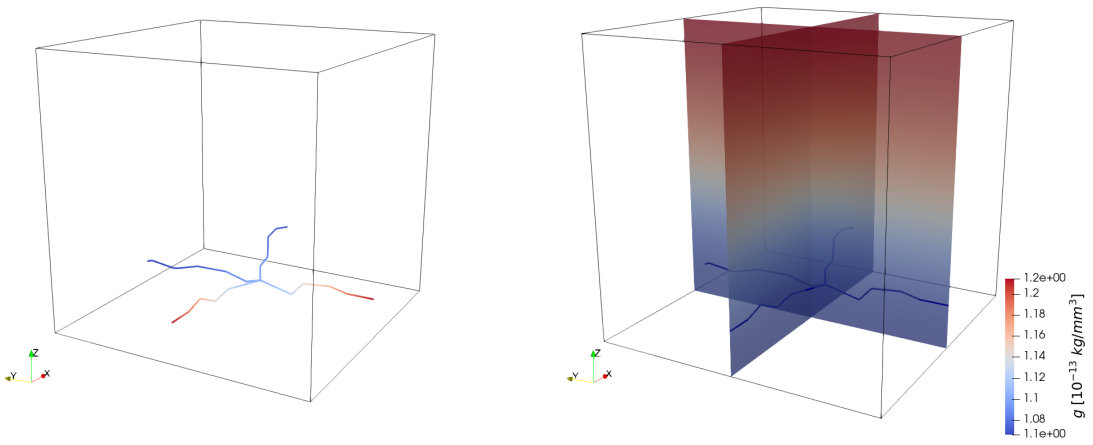

Figure 4.1: On the left, initial capillary network with two blood inlets (red) and two outlets (blue). On the right, initial condition for VEGF problem in the default setting

Now, for what concerns the time discretization, we choose the same uniform time-stepping both for the growth of the network and for the Euler backward method, in particular we set $\Delta\mathcal{I}_k = \Delta t = 12$ h.

On the other hand, for the discretization of the spatial domain, we consider a tetrahedral mesh in which the maximum size of each element is given by $5 \cdot 10^{-6}$.
Regarding instead the parameters of pressure, oxygen, VEGF and network growth, they are listed in Tables (4.1)-(4.3) and we will use them as a default setting.

Table 4.1: Default parameter for pressure.

Parameter	Value	Unit	Description	Reference
β_p^0	$2.78 \cdot 10^{-10}$	$\frac{\text{mm}^2 \cdot \text{h}}{\text{kg}}$	Hydraulic permeability of healthy capillary wall	[6]
r_p^β	10	-	Increase of wall permeability for tumor-generated capillaries	[5]
Δp_{onc}	$4.32 \cdot 10^7$	$\frac{\text{kg}}{\text{mm} \cdot \text{h}^2}$	Oncotic pressure jump at the capillary wall	-
$\beta_p^{LS} \frac{S}{V}$	$2.89 \cdot 10^{-7}$	$\frac{\text{mm} \cdot \text{h}}{\text{kg}}$	Effective permeability of the lymphatic vessels	[6]
k	$1.0 \cdot 10^{-12}$	mm^2	Hydraulic permeability of the tissue	[6]
μ	$1.44 \cdot 10^{-2}$	$\frac{\text{kg}}{\text{mm} \cdot \text{h}}$	Blood viscosity	[6]
$\tilde{p}_{in}$	$6.26 \cdot 10^7$	$\frac{\text{kg}}{\text{mm} \cdot \text{h}^2}$	Inflow pressure	-
$\tilde{p}_{out}$	$6.05 \cdot 10^7$	$\frac{\text{kg}}{\text{mm} \cdot \text{h}^2}$	Outflow pressure	-
p_{LS}	0	$\frac{\text{kg}}{\text{mm} \cdot \text{h}^2}$	Lymphatic system pressure	-
p_{ext}	0	$\frac{\text{kg}}{\text{mm} \cdot \text{h}^2}$	External pressure	-
β_p^{ext}	$1.4 \cdot 10^{-8}$	$\frac{\text{mm}^2 \cdot \text{h}}{\text{kg}}$	Boundary conductivity	[6]

In particular, looking at Tables (4.1) and (4.2), we have introduced two parameters, namely r_p^β and r_c^β, that allow us to describe the *wall permeability increment* that occurs in the blood vessels generated during the angiogenesis process.
In this perspective, we define the pressure hydraulic permeability of the capillary wall as

$$\beta_p(\mathbf{x}) = \begin{cases} \beta_p^0 & \forall \mathbf{x} \in \Lambda^0 \\ r_p^\beta \beta_p^0 & \forall \mathbf{x} \in \Lambda^k \backslash \Lambda^0, \quad \forall k = 0, \dots, K, \end{cases} \tag{4.1}$$

and the oxygen hydraulic permeability of the capillary wall as

Table 4.2: Default parameter for oxygen.

Parameter	Value	Unit	Description	Reference
β_c^0	12.6	$\frac{\text{mm}}{\text{h}}$	Hydraulic permeability of healthy capillary wall	[6]
r_c^β	10	-	Increase of wall permeability for tumor-generated capillaries	-
D_c	4.86	$\frac{\text{mm}^2}{\text{h}}$	Diffusivity, tissue	[6]
m_c	3.6	h^{-1}	Decay/metabolization parameter	-
$\tilde{D}_c$	$1.8 \cdot 10^3$	$\frac{\text{mm}^2}{\text{h}}$	Vascular diffusivity	[6]
$\tilde{c}_{in}$	$1.64 \cdot 10^8$	$\frac{\text{kg}}{\text{mm} \cdot \text{h}^2}$	Inflow concentration	-
c_{ext}	$6.05 \cdot 10^6$	$\frac{\text{kg}}{\text{mm} \cdot \text{h}^2}$	External oxygen concentration	[6]
β_c^{ext}	36	$\frac{\text{mm}}{\text{h}}$	Boundary permeability	-

$$\beta_c(\mathbf{x}) = \begin{cases} \beta_c^0 & \forall \mathbf{x} \in \Lambda^0 \\ r_c^\beta \beta_c^0 & \forall \mathbf{x} \in \Lambda^k \backslash \Lambda^0, \quad \forall k = 0, \dots, K. \end{cases} \tag{4.2}$$

This mathematical expedient allows to take in consideration the fact that tumor-induced vessels are much more leaky than the physiological ones. This happens as the adhesion forces between the endothelial cells in pathological conditions are weaker and so the permeability of vessel walls to fluid and chemicals increases, as shown by biological evidences. Furthermore, for what concerns the values listed in Table (4.3), biological experiments show that the mean VEGF concentration in the tissue is about 20 ng/ml ([22]), while endothelial cells migrate at a VEGF concentration of 50 ng/ml ([31]).
In this work, since we measure the mass in kg, the volume in mm^3 and the time in h, when we convert the above values to our units of measure, we obtain that the order of magnitude of VEGF concentration is 10^{-14} kg/mm^3.
In light of these considerations, we choose to work with

- $g_{lim} = 2.5 \cdot 10^{-14} \ \frac{\text{kg}}{\text{mm}^3}$,
- $\overline{g} = 4 g_{lim} = 1 \cdot 10^{-13} \ \frac{\text{kg}}{\text{mm}^3}$ (according to [25]).

Moreover, data inferred from biological experiments also show that the VEGF diffusion coefficient ranges between $0.036 - 2.16$ mm^2/h, while its decay rate is in the order of $0.456 - 0.65$ h^{-1} ([24]).

Table 4.3: Default parameter for VEGF and network growth.

Parameter	Value	Unit	Description	Reference
D_g	0.18	$\frac{\text{mm}^2}{\text{h}}$	VEGF diffusivity	-
r_g	1	h^{-1}	Rate of VEGF production by the source	-
σ	0.5	h^{-1}	VEGF interstitial decay	-
$\tilde{\sigma}$	0.7	h^{-1}	Endothelial cell VEGF consumption rate	-
g_{lim}	$2.5 \cdot 10^{-14}$	$\frac{\text{kg}}{\text{mm}^3}$	Minimum VEGF concentration for cell proliferation	[22], [31]
$\overline{g}$	$1.0 \cdot 10^{-13}$	$\frac{\text{kg}}{\text{mm}^3}$	VEGF concentration for $t_c = 2\tau$ cell proliferation	[25]
g_{br}	$1.0 \cdot 10^{-13}$	$\frac{\text{kg}}{\text{mm}^3}$	VEGF concentration for $\mathbb{P}_{br} = 1$	-
τ	12	h	Cell proliferation parameter	[25]
l_e	0.04	mm	Endothelial cell length	[25]
α_{br}^w	0.3	-	Threshold of $\frac{\|\|\mathbf{w}_\Pi\|\|}{\|\|\mathbf{w}\|\|}$ for branching	-
d_{br}	$1.0 \cdot 10^{-2}$	mm	Branching distance	-
τ_{br}	48	h	Threshold age for branching	-
d_{an}	$1.0 \cdot 10^{-5}$	mm	Maximum distance for anastomosis	-
τ_{an}	24	h	Maximum capillary age for anastomosis	-

To conclude, we also suppose that only the cells belonging to the tumor-induced network can bind VEGF and consume it. So we can define the VEGF consumption rate as

$$\tilde{\sigma}(\mathbf{x}) = \begin{cases} 0 & \forall \mathbf{x} \in \Lambda^0 \\ \tilde{\sigma} & \forall \mathbf{x} \in \Lambda^k \backslash \Lambda^0, \quad \forall k = 0, \dots, K. \end{cases} \tag{4.3}$$

Before carrying any simulation to understand the impact of the parameter on the whole dynamics, we report the results for the default setting.
To this aim, Figure (4.2) shows, from the top to the bottom, the distributions of pressure, oxygen and VEGF for the default parameters, while Figure and (4.3) gives a representation of the trascapillary flux of fluid and oxygen.
Every quantity is reported at time t = 2, 7, 14 days.
In the first row of Figure (4.2), we can observe that the pressure in the interstitial tissue is lower than the pressure in the blood vessels and it increases over the time: this means

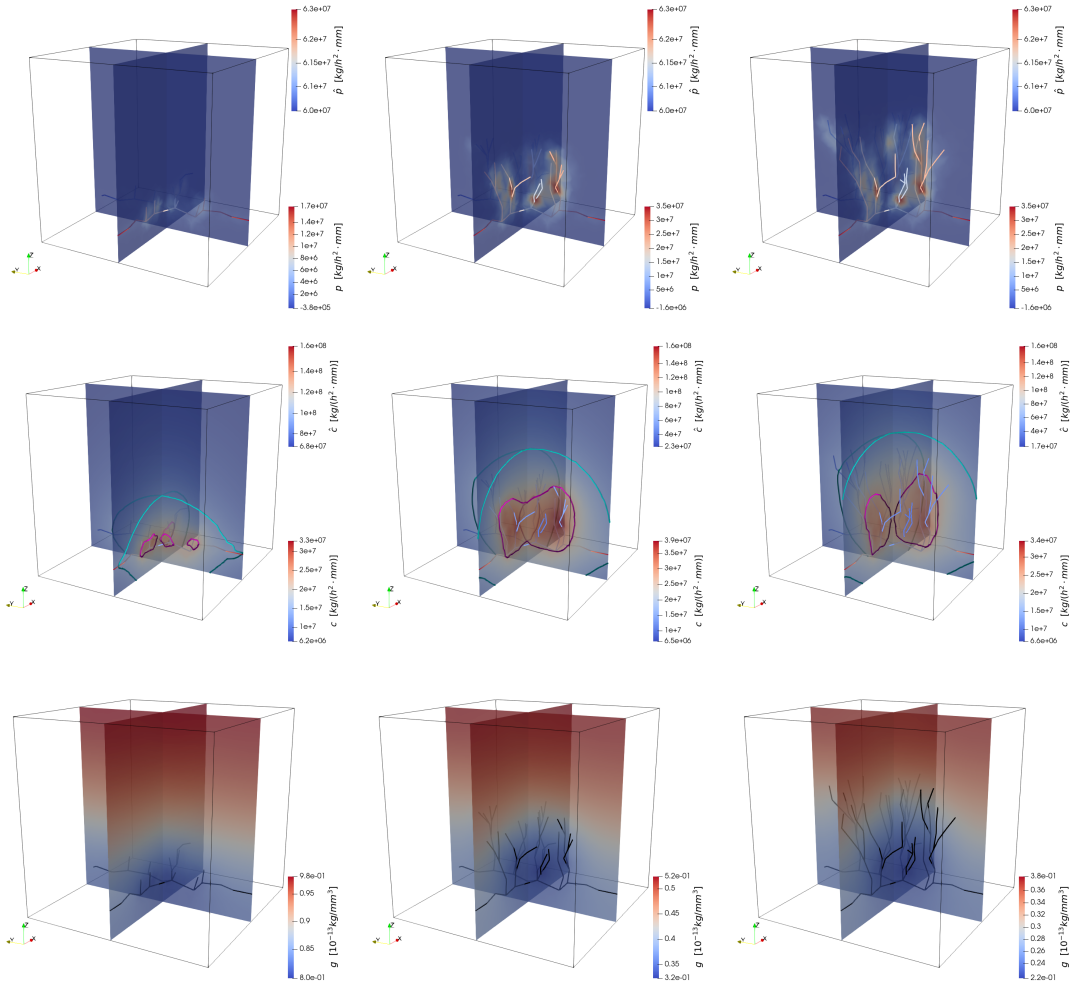

Figure 4.2: Simulation of angiogenesis in the default setting with parameters listed in tables (4.1), (4.2) and (4.3). First row: pressure evolution at times t = 2, 7, 14 days. Second row: oxygen evolution at times t = 2, 7, 14 days with isolines corresponding to 8 mmHg (cyan) and 15 mmHg (magenta). Third row: VEGF evolution at times t = 2, 7, 14 days.

that fluid moves from the vessels to the tissue, exhibiting an arterious behavior. This trend is confirmed by the results reported in the first row of Figure (4.3), where we show the trascapillary flux distribution.
More specifically, this value is computed taking in consideration the difference between the pressure in the blood vessel and the interstitial fluid one. For this reason, since the color scales show positive ranges, we conclude that the fluid flows from the vessels to the interstitium.
For what concerns the oxygen, the corresponding results are shown in the second row of Figure (4.2), in which we also report the isolines for $c = 1.38 \cdot 10^7$ kg/(h$^2 \cdot$ mm) $\approx$

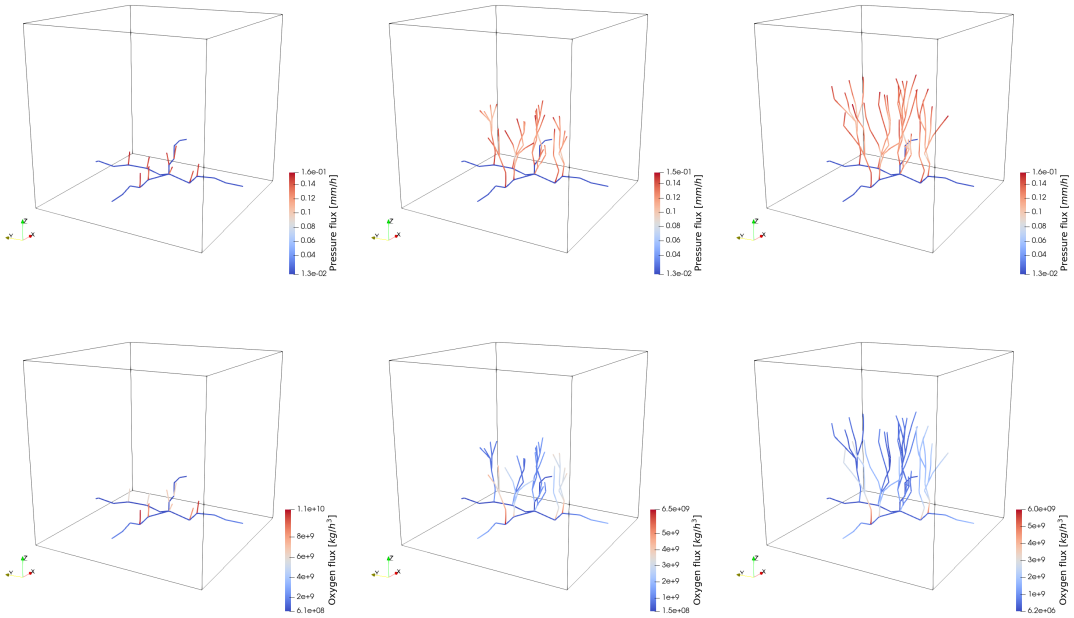

Figure 4.3: Simulation of angiogenesis in the default setting with parameters listed in tables (4.1), (4.2) and (4.3). First row: pressure trascapillary flux at times t = 2, 7, 14 days. Second row: oxygen trascapillary flux at times t = 2, 7, 14 days.

8 mmHg (cyan) and for $c = 2.60 \cdot 10^7$ kg/(h^2 · mm) $\approx$ 15 mmHg (magenta). We remind that, as reported in the previous sections, these thresholds stand for the pathological and physiological hypoxia levels, respectively. Looking at the corresponding isolines, we understand that, starting from an initial condition in which the tissue is highly hypoxic, as the network grows the oxygen flows from the vessels to the interstitium, leading to an increment of its value in the tridimensional domain.

Also in this case, looking at the second row of Figure (4.3), we can observe that the distribution of the oxygen trascapillary flux has a positive range of values and, since it is defined taking in consideration the difference between the value in the blood vessels and in the tissue, we can confirm that the behavior of the oxygen is exactly the one described above.

Finally, the third row of Figure (4.2) shows the VEGF evolution. In this case, differently from the model presented in [3], we consider a source of VEGF that depends on the available oxygen such that the higher is the oxygen, the lower is VEGF production. Moreover, such source is not concentrated on a single face of the domain, but it has initial spatial distribution which is shown in the right panel of Figure (4.1).

We can observe that, even if the network grows, it does not reach the top of the spatial domain but it seems to stabilize. In fact, looking at the maximum value of the VEGF over time, we can see that it reduces and, at the same time, the minimum of the oxygen increases.

This means that as the oxygen increases, the tissue does not suffer for hypoxic conditions and, consequently, the VEGF source is weaker. Moreover, since VEGF is a promoter of endothelial cell proliferation, when it is low, cells are less induced to duplicate and so the network has a limited growth.
In the following section we provide some experiments to show how the variation of the parameters impacts on the final solution.

4.2 Numerical Simulations

In this section we carry some numerical simulations in order understand how the network morphology and the dynamics of pressure and chemicals are influenced by the variation of a single parameter. In particular, in the following we focus on the ones related to the virtual growth of the network, the source of VEGF and the pressure.

4.2.1 The virtual growth

One of the main novelty with respect to the work presented in [3] is the implementation of the virtual growth of the network.
We remind that, in this framework, the vessels are allowed to grow only if the distance between two tip cells is greater than a threshold value.
Furthermore, the proliferation of the endothelial cells occurs at a characteristic time, namely the *cell division time*, that depends on the available VEGF, as we can read in Equation (2.66).
In addition, for the numerical resolution, we have to establish a time step for the Euler method that we adopt for the semi-discretization in time.
In light of these considerations, to understand the impact that the implementation of the virtual growth has on the final morphology, we run some simulations to compare the outcomes for different Euler method time-step.
Furthermore, in order to efficiently discuss the behavior of the dynamics, we decide to temporarily remove the dependence of the cell division time from the VEGF distribution. More specifically, we set

$$t_c(g) = 24 \text{ h} \quad \forall g(\mathbf{x}, t),$$

such that each endothelial cell proliferates with the same characteristic time, independently on its spatial location and on the available VEGF.
Now, we can finally analyse what happens when we consider different time-steps: we are interested in understanding the differences that occur when the time-step is lower or greater than the cell division time.
The results are shown in Figure (4.4), where we consider, on the left column, the outcomes obtained without the implementation of the virtual growth while, on the right, the ones for the virtual growth. For what concerns the values of the time-step, we consider $\Delta t = 6, 12, 48$ h, whose corresponding results are reported from the top to the bottom of Figure (4.4)

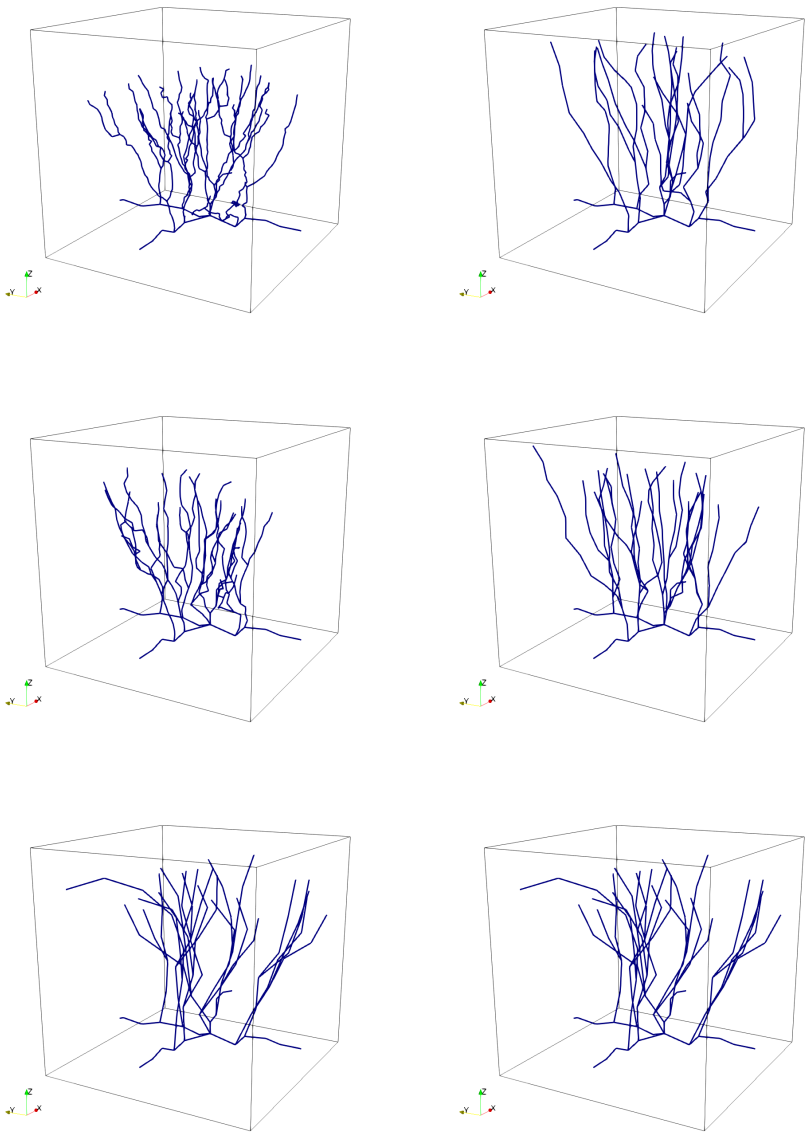

Figure 4.4: Simulation of angiogenesis with a fixed value $t_c = 24$ h. First column: results without the implementation of the virtual growth criterion. Second column: results with the implementation of the virtual growth criterion. First row: results for $\Delta t = 6$ h. Second row: results for $\Delta t = 12$ h. Third row: results for $\Delta t = 48$ h.

We can observe that for $\Delta t < t_c$ (first and second rows), the networks obtained without the implementation of the virtual growth (left panel) are much different from the ones obtained thanks to the virtual growth (right panel), which are instead comparable.

In fact, when the time-step is small and when the network is allowed to grow independently from the distance between two consecutive tip cells, the vessels can extend at each iteration of the method, even of a tiny segment. The results is that the morphology shows a fluctuating pattern, while the virtual growth guarantees a smoother geometry.
On the contrary, the third row of Figure (4.4) shows the outcomes for $\Delta t > t_c$ ($\Delta t = 48$) and we can observe that the results are comparable, while the final morphology highly depends on the chosen time step, when $\Delta t < t_c$.
Indeed, since the time-step is large, the endothelial cells can duplicate themselves at least once, so it is plausible that the distance between the current tip cell and its position in the previous iteration is at least equal, or even greater, than the endothelial cell length.
In this perspective, we expect that the implementation of the two growth criteria leads to the same results, as we obtain in the third row of Figure (4.4).

4.2.2 The VEGF source

Another novelty with respect to the work [3] is the introduction of a VEGF source that replaces the original Dirichlet boundary condition on the upper face of the domain, which constituted the interface between the tissue and the tumor.
This change is useful for a preliminary analysis of the model presented in the second part of this work, in which we introduce the tumor growth dynamics coupled with the angiogenesis process. In the second part of this work, in fact, the VEGF source will be constituted by the cells, which are dispersed in the spatial domain.
In this perspective, it is useful to understand what happens when we act on the parameters that regulate the intensity and the shape of the source, moreover we also analyse the response to the variation of the VEGF consumption rate.
Let us start from the initial VEGF distribution shown in the right panel of Figure (4.1) and let us consider different values for the rate of VEGF production. As reported in Figure (4.5), we can see that, as expected, the lower is the production intensity, the lower is the growth of the network.
In particular, we can see that for $r_g = 0.5$ the network has a limited growth and, in addition, it does not undergo branching.
On the opposite side, for $r_g = 2$, the network is enough stimulated to grow, such that it reaches the top of the domain and the number of branching considerably increases.
Another parameter that has an important impact on the dynamics is the VEGF consumption rate, as reported in Figure (4.6).
Let us start from $\tilde{\sigma} = 0$, i.e. the network does not consume VEGF. In this framework VEGF concentration can decrease for the sole effect of the self-degradation, so its value remains high and the network can extend and produce a large number of branching.
It is also useful to observe that the structure of the resulting network is not spread over the space: this is due to the fact that, since the vessels does not consume the growth factor, it remains high in the proximity of tip cells, so they do not have to explore the domain to find higher concentration of VEGF (chemotactic effects are not strong).
When we consider instead a high consumption rate, we can see that the network growth is lower. In particular, taking for example $\tilde{\sigma} = 5$, the value of VEGF in proximity of the network is very low so it cannot grow neither undergo branching.

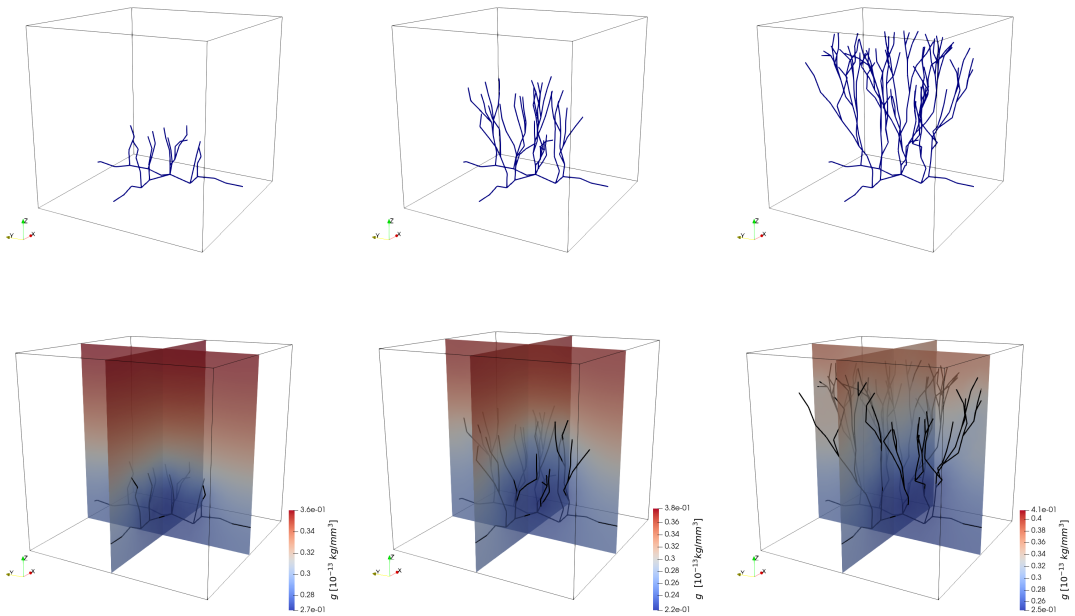

Figure 4.5: Simulations of angiogenesis varying r_g. First row: network morphology a time $T = 14$ days. Second row: VEGF distribution at time $T = 14$ days. From the left to the right, result for $r_g = 0.5$, $r_g = 1$ and $r_g = 2$.

To conclude, we now provide an example with a different shape of the VEGF source.
In this perspective, let us consider a spherical initial distribution, placed in the middle of the domain.
The corresponding results are reported in Figure (4.7), where the first column shows the outcomes for $r_g = 1$ and the second the ones for $r_g = 2$. From the top to the bottom of the figure, we report the initial condition, the final VEGF distribution and network morphology for $T = 14$ days.
As we can observe, for $r_g = 1$ the VEGF source is not strong enough to guarantee a significant growth of the network but, despite this, we can see how the vessels try to point toward the centre of the domain, where the VEGF concentration is higher.
Looking at $r_g = 2$, instead, the VEGF source is stronger and the growth is more encouraged. Also in this case, the vessels initially point toward the centre of the domain and then, as they start consuming VEGF, they enlarge.

4.2.3 The pressure problem

In this last section we provide some experiments to show how the fluid parameters impact on the trascapillary flux.
In this perspective, to efficiently analyse the results, we look at significative quantities that allow us to understand the behavior of the process at a macroscopic scale.

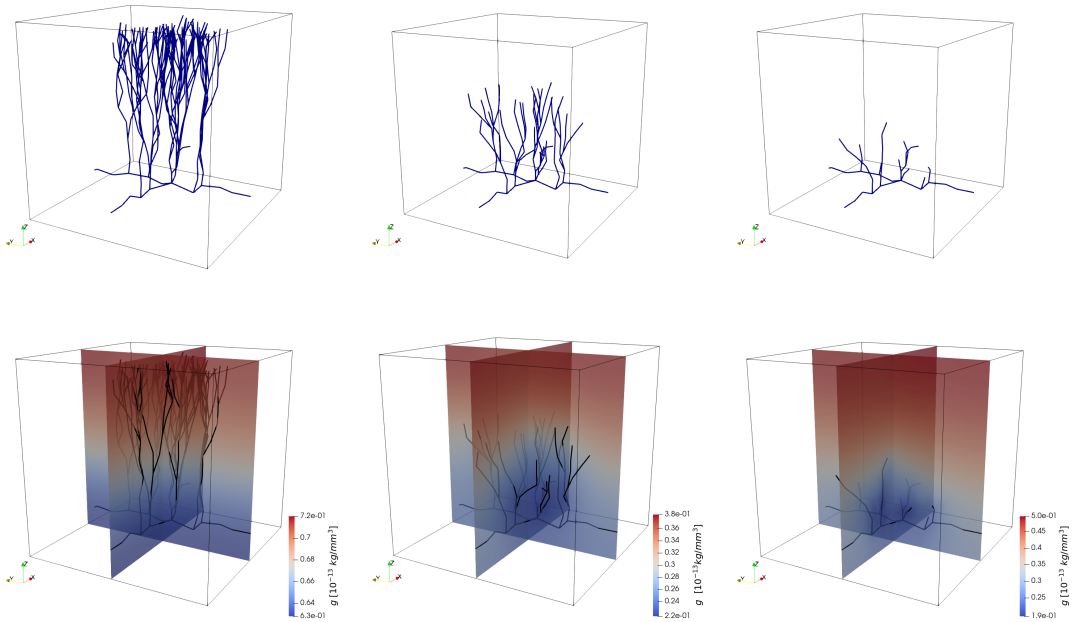

Figure 4.6: Simulations of angiogenesis for different $\tilde{\sigma}$. First row: network morphology at time $T = 14$ days. Second row: VEGF distribution at time $T = 14$ days. From the left to the right, result for $\tilde{\sigma} = 0$, $\tilde{\sigma} = 0.7$ and $\tilde{\sigma} = 5$.

Table 4.4: Pressure characteristic values for the default setting

Max $\check{p}$	Min $\check{p}$	Max $\hat{p}$	Min $\hat{p}$	Total pr. flux	Max pr. flux	Min pr. flux	Network length	Arterious flux
20.1635	-0.9373	36.2500	35.0000	0.6038	0.1556	0.0131	5.8427	5.8427

In particular, we focus on the maximum and minimum pressure values in the interstitial tissue at the final time of $T = 14$ days and, for what concerns the analysis of the trascapillary flux, we compute it taking in consideration the difference between the pressure in the blood vessels and in the tissue, as mentioned in the previous section.
More specifically, we obtain it with the following expression:

$$f_p(s,t) = \begin{cases} \beta_p^0(\hat{p}(s,t) - \check{p}(s,t)) & \forall \mathbf{x} \in \Lambda^0 \\ r_p^\beta \beta_p^0(\hat{p}(s,t) - \check{p}(s,t)) & \forall \mathbf{x} \in \Lambda^k \backslash \Lambda^0. \end{cases} \tag{4.4}$$

Furthermore, in order to evaluate the magnitude of the flux across the whole network, we introduce the computation of the total trans-capillary flux and we defined it as follows:

$$F_p(s,t) = \int_\Lambda f_p(s,t) ds. \tag{4.5}$$

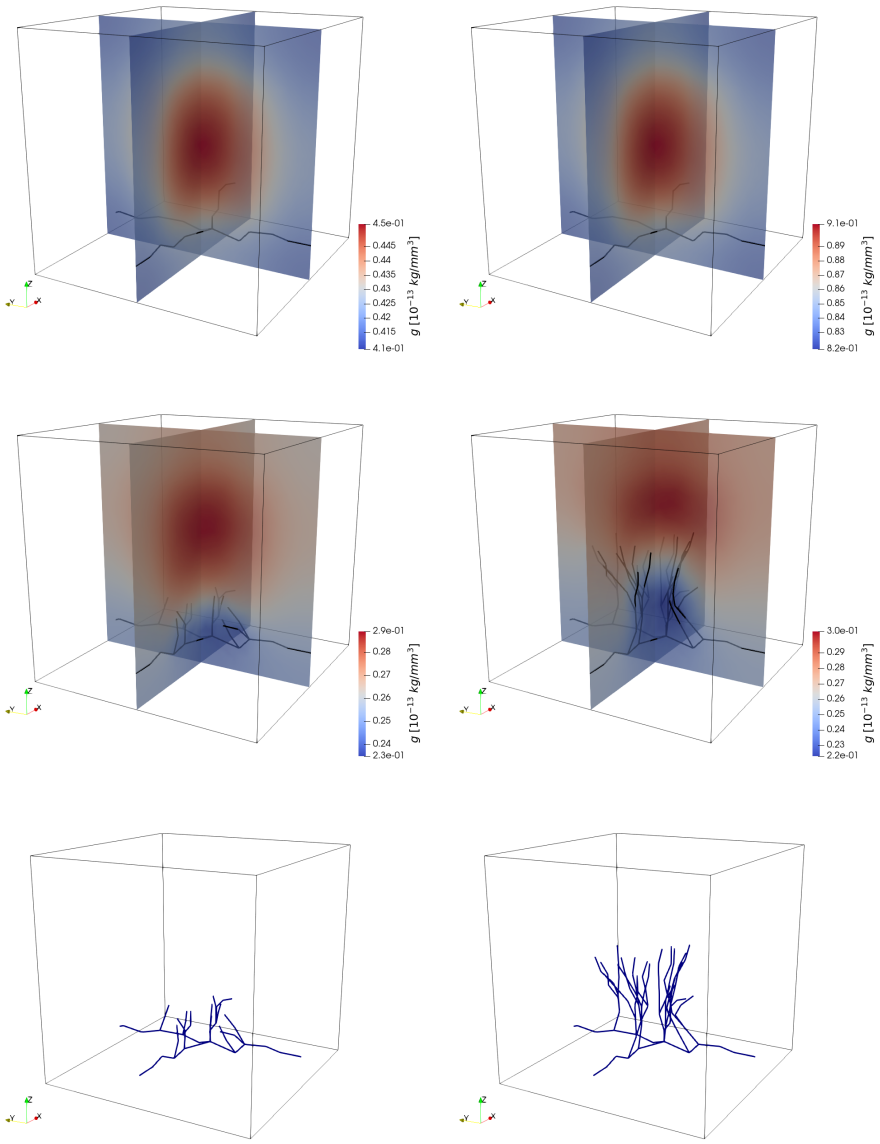

Figure 4.7: Simulations with different initial VEGF distribution. First row: VEGF initial condition. Second row: final VEGF distribution at time $T = 14$ days. Third row: network morphology at time $T = 14$ days. First column: results for $r_g = 1$. Second column: results for $r_g = 2$.

Finally, to measure the extension of the whole network and which percentage of its length is involved by an arterious flow, we introduce a function for the estimation of the total network length and of the portion of the network in which the quantity introduced in

(4.4) is greater than zero.
For what concerns the results of the simulations, Table (4.4) contains all the quantities described above for the default setting, while Tables (4.5), (4.6), (4.7) and (4.8) report the behavior of the pressure dynamics for the variation of the parameters r_p, β_p^0, $\beta_p^{LS}\frac{S}{V}$ and k, respectively.

Table 4.5: Pressure values for different r_p^β

r_p^β	Max $\check{p}$	Min $\check{p}$	Total pr. flux	Max pr. flux	Min pr. flux	Network length	Arterious flux
1	2.9767	-0.1179	0.0959	0.0172	0.0157	5.8056	5.8056
10	20.1635	-0.9373	0.6038	0.1556	0.0131	5.8427	5.8427
50	48.1218	-2.2893	0.7678	0.6117	-0.2777	5.7083	5.0863
100	57.7989	-2.7159	-0.6933	0.9008	-0.9695	5.6950	2.2627

Table 4.6: Pressure values for different β_p^0

β_p^0	Max $\check{p}$	Min $\check{p}$	Total pr. flux	Max pr. flux	Min pr. flux	Network length	Arterious flux
$1 \cdot 10^{-7}$	2.6212	-0.1204	0.0801	0.0171	0.0017	5.8058	5.8058
$0.5 \cdot 10^{-6}$	11.5772	-0.5349	0.3566	0.0814	0.0075	5.8849	5.8849
$1 \cdot 10^{-6}$	20.1635	-0.9373	0.6038	0.1556	0.0131	5.8427	5.8427
$5 \cdot 10^{-6}$	48.1539	-2.2826	0.8094	0.6117	-0.2781	5.7079	5.0859
$1 \cdot 10^{-5}$	57.8132	-2.7076	-0.6292	0.9013	-0.9715	5.6942	2.1664

Let us consider Tables (4.5) and (4.6), which are both related to the variation of the hydraulic permeability of the capillary wall. More specifically, Table (4.5) refers to the variation of the increment of the permeability of the tumor-induced vessels, while Table (4.6) is referred to the variation of the permeability of the healthy capillary wall.
Looking at the outcomes, we can observe that the larger is the permeability, the higher is the pressure in the interstitial tissue.
Furthermore, as we can read in Table (4.4), the minimum value of vascular pressure is $\hat{p}(s,t) = 35$ mmHg, while the maximum is $\hat{p}(s,t) = 36.25$ mmHg and these values does not change when we let the above parameters vary.
When the permeability of the vessels is large, the maximum interstitial pressure is greater than the one in the vasculature and so the fluid flow changes its directions, going from the tissue to the vessels, showing a venous behaviour. This phenomenon is evident for $r_p = 100$, $r_p = 50$, $\beta_p^0 = 1 \cdot 10^{-5}$ and $\beta_p^0 = 5 \cdot 10^{-6}$, which correspond to higher values of the vessel wall permeability.
In particular, looking at the total network length and at the portion of network involved by an arterious trans-capillary flux we observe that, as the permeability decreases, the

portion of arterious network gets greater. For example, we can see that

- for $r_p = 100$, only 40% of the whole network shows arterious flux and the total pressure flux exhibits a negative value,
- for $r_p = 50$, the arterious flux sensibly increases and the portion of network involved by arterious flow reaches about the 90%,
- for $r_p = 10$ and $r_p = 1$, the arterious flux is restored on the whole network.

Similar considerations hold for the results reported in Table (4.6).

Table 4.7: Pressure values for different $\beta_p^{LS}\frac{S}{V}$

$\beta_p^{LS}\frac{S}{V}$	Max $\check{p}$	Min $\check{p}$	Total pr. flux	Max pr. flux	Min pr. flux	Network length	Arterious flux
0	50.7432	-0.1487	-0.0695	0.0897	-0.0723	5.7184	2.1735
0.1	30.2057	-0.1070	0.3814	0.1388	0.0098	5.7949	5.7949
0.5	20.1635	-0.9373	0.6038	0.1556	0.0131	5.8427	5.8427
1	16.6306	-1.3066	0.6731	0.1622	0.0140	5.8465	5.8465

Let us consider now the values listed in Table (4.7), in which we analyse the response of the pressure dynamics when we act on the permeability of the lymphatic system.
As we can read in the first column of Table (4.7), when we do not consider the existence of the lymphatic drainage, i.e. $\beta_p^{LS}\frac{S}{V} = 0$, the interstitial pressure is very high.
In fact, when the excess fluid is not absorbed by the lymphatic system, it exerts a high pressure in the interstitium and it flows towards the vessels, showing again a venous behavior.
As the lymphatic system permeability increases, the efficiency of the drainage improves and the arterious flow is restored.

Table 4.8: Pressure values for different $\frac{k}{\mu}$

$\frac{k}{\mu}$	Max $\check{p}$	Min $\check{p}$	Total pr. flux	Max pr. flux	Min pr. flux	Network length	Arterious flux
$1 \cdot 10^{-13}$	43.1397	-7.7557	0.4259	0.1622	-0.0294	5.8881	5.8607
$0.5 \cdot 10^{-12}$	27.4589	-2.2263	0.5495	0.1542	0.0116	5.8516	5.8516
$1 \cdot 10^{-12}$	20.1635	-0.9373	0.6038	0.1556	0.0131	5.8427	5.8427
$5 \cdot 10^{-12}$	8.8458	$6.457 \cdot 10^{-6}$	0.6944	0.1625	0.0151	5.7255	5.7255
$1 \cdot 10^{-11}$	6.0935	$3.25 \cdot 10^{-4}$	0.7224	0.1650	0.0156	5.7094	5.7094

To conclude, we also report an analysis of the impact of the diffusivity coefficient. In particular we focus on the hydraulic permeability of the tissue, as reported in Table (4.8). In this framework, the dynamics shows an arterious flow for almost every value of k, except for a very small portion of network involved by venous flux for $k = 1 \cdot 10^{-13}$ mm^2. The most important differences lie in the maximum and minimum values of interstitial pressure. In fact, we can observe that the higher is the hydraulic permeability, the lower is the difference between the maximum and the minimum interstitial pressure.
Moreover, for very low values of k, the minimum pressure assumes negative values, showing a sort of "fluctuating" behavior. This confirms the impact of the diffusion coefficients on the regularization of the dynamics.

Part II

Tumor Growth

Chapter 5

The mathematical model for vascular tumor growth with angiogenesis

5.1 The cell concentration model

In this section we introduce the tumor growth dynamics, that we want to couple with the angiogenesis process described in the previous chapters.
In this perspective, the starting point is a vascularized tissue, treated as a mixture with no distinction between healthy and cancer cells.
First of all, we obtain the governing law of the cells evolution, in order to add it to the equations introduced for the angiogenesis process.
Similarly to [12], let us consider a tissue constituted by cancer cells, liquid and extracellular matrix. In particular, we denote by ϕ_c, ϕ_ℓ and ϕ_m the volumetric fraction of cell, liquid and extracellular matrix phases, respectively.
The following equations for mass and momentum balance hold in the 3D-domain:

$$\begin{cases} \dfrac{\partial \phi_i}{\partial t} + \nabla \cdot (\phi_i \mathbf{v}_i) = \Gamma_i \qquad i = \{c, l, m\} \\ \hat{\rho}_i \left[\dfrac{\partial (\phi_i \mathbf{v}_i)}{\partial t} + \nabla \cdot (\phi_i \mathbf{v}_i \otimes \mathbf{v}_i) \right] = \nabla \cdot \tilde{\mathbb{T}}_i + \tilde{\mathbf{m}}_i + \hat{\rho}_i \Gamma_i \mathbf{v}_i. \end{cases} \tag{5.1}$$

In particular

- $\mathbf{v}_i$ is the velocity of the ith phase,
- $\hat{\rho}_i$ is the true volumetric mass density of the ith phase,
- $\tilde{\mathbb{T}}_i$ is the *partial* stress-tensor of the ith phase,
- Γ_i represents the rate at which the ith phase exchanges mass with the other phases,

- $\tilde{\mathbf{m}}_i$ represents the rate at which the ith phase exchanges momentum with the other phases.

5.1.1 Constitutive Assumptions and Modelling Simplifications

In this section, we focus on the momentum balance equations and, first of all, we look at the partial stress tensor and at the momentum exchange rates.
In particular, for what concerns $\tilde{\mathbb{T}}_i$, in a saturated mixture it is given by the *purely hydrostatic* contribution $-\phi_i p\mathbb{I}$, that indicates the amount of pressure sustained by the ith phase, and the *effective* stress-tensor $\mathbb{T}_i$.
The term $\tilde{\mathbf{m}}_i$, instead, is constituted by the non-dissipative component $p\nabla\phi_i$, and the dissipative one $\tilde{\mathbf{m}}_i^{(d)}$. More specifically, we define

$$\tilde{\mathbb{T}}_i = -\phi_i p\mathbb{I} + \mathbb{T}_i \qquad \text{and} \qquad \tilde{\mathbf{m}}_i = \tilde{\mathbf{m}}_i^{(d)} + p\nabla\phi_i. \tag{5.2}$$

where p is the pressure of the interstitial fluid.
Let us focus now on $\tilde{\mathbf{m}}_i^{(d)}$, which is given by the sum of the following two terms:

$$\tilde{\mathbf{m}}_i^{(d)} = \mathbf{G}_i + \overline{\mathbf{m}}_i. \tag{5.3}$$

The first one vanishes with the growth contribution, so we can write

$$\mathbf{G}_i = -\hat{\rho}_i \Gamma_i \mathbf{v}_i. \tag{5.4}$$

The second one, instead, takes the following form

$$\overline{\mathbf{m}}_i = \sum_{\beta \neq i} \overline{\mathbf{m}}_{i\beta}, \tag{5.5}$$

where each term $\overline{\mathbf{m}}_{i\beta}$ represents the force acting on the ith phase due to the presence of the βth phase. In this framework, we assume a viscous interaction between the constituents, so that

$$\overline{\mathbf{m}}_{i\beta} \propto -\phi_i\phi_\beta(\mathbf{v}_i - \mathbf{v}_\beta), \tag{5.6}$$

while, for the action-reaction principle we have that

$$\overline{\mathbf{m}}_{i\beta} = -\overline{\mathbf{m}}_{\beta i}. \tag{5.7}$$

Moreover, in the following we will work under the hypothesis that:

- since we consider the presence of blood vessels and lymphatic system, differently from [12], the mixture is not closed with respect to the mass,
- we do not take into account any momentum exchange between the tissue and the blood vessels,

- the inertial forces are negligible in the momentum balance law for each phase, therefore the corresponding equations reads as

$$\nabla \cdot \tilde{\mathbb{T}}_i + \tilde{\mathbf{m}}_i + \hat{\rho}_i \Gamma_i \mathbf{v}_i = 0, \tag{5.8}$$

  that, by simple calculations, reduces to

$$\nabla \cdot \mathbb{T}_i - \phi_i \nabla p + \overline{\mathbf{m}}_i = 0, \tag{5.9}$$

- the extracellular matrix is rigid and inert, so

$$\mathbf{v}_m \approx 0 \quad \text{and} \quad \Gamma_m \approx 0, \tag{5.10}$$

- the stress tensor of the liquid phase is negligible, so

$$\nabla \cdot \mathbb{T}_\ell \approx 0. \tag{5.11}$$

We can now explicit the system of equations that govern the mixture dynamics:

$$\begin{cases} \phi_c + \phi_\ell + \phi_m = 1 & (5.12) \\ \dfrac{\partial \phi_c}{\partial t} + \nabla \cdot (\phi_c \mathbf{v}_c) = \Gamma_c & (5.13) \\ \dfrac{\partial \phi_\ell}{\partial t} + \nabla \cdot (\phi_\ell \mathbf{v}_\ell) = \Gamma_\ell & (5.14) \\ \dfrac{\partial \phi_m}{\partial t} = 0 & (5.15) \\ -\phi_c \nabla p + \nabla \cdot \mathbb{T}_c + \overline{\mathbf{m}}_{cm} + \overline{\mathbf{m}}_{cl} = 0 & (5.16) \\ -\phi_\ell \nabla p + \overline{\mathbf{m}}_{lm} + \overline{\mathbf{m}}_{lc} = 0. & (5.17) \end{cases}$$

In particular, the following definitions hold

$$\overline{\mathbf{m}}_{lc} = -\phi_\ell \phi_c \mu [\mathbb{K}(\phi_\ell)]^{-1} (\mathbf{v}_\ell - \mathbf{v}_c), \tag{5.18}$$

$$\overline{\mathbf{m}}_{lm} = -\phi_\ell \phi_m \mu [\mathbb{K}(\phi_\ell)]^{-1} \mathbf{v}_\ell, \tag{5.19}$$

$$\overline{\mathbf{m}}_{cl} = -\overline{\mathbf{m}}_{lc}, \tag{5.20}$$

$$\overline{\mathbf{m}}_{cm} = -[\mathbb{M}(\phi_c, \phi_m)]^{-1} \mathbf{v}_c, \tag{5.21}$$

$$\mathbb{T}_c = -\Sigma(\phi_c)\mathbb{I}, \tag{5.22}$$

$$\Sigma(\phi_c) = E \frac{\phi_c - \phi_0}{\phi_{max} - \phi_c} \phi_c, \tag{5.23}$$

where μ is the viscosity of the extracellular fluid, $\mathbb{K}(\phi_\ell)$ is the permeability tensor, $\mathbb{M}(\phi_c, \phi_m)$ is the motility tensor and E is the Young modulus.

Finally, we introduce two more assumptions coming from the dimensional analysis of the momentum balance equations that, as shown in [12], allows to identify which are the dominant contributions in the correspondent laws:

- $\dfrac{\mathbf{v}_c}{\mathbf{v}_\ell} \ll 1 \quad \Longrightarrow \quad \overline{\mathbf{m}}_{cl} \approx \phi_c\phi_\ell\mu\big[\mathbb{K}(\phi_\ell)\big]^{-1}\mathbf{v}_\ell$
- $\dfrac{\Delta p}{E} \ll 1 \quad \Longrightarrow \quad \overline{\mathbf{m}}_{cl} \ll \overline{\mathbf{m}}_{cm},$

  where Δp is the scaling factor of the pressure variable and it represents the gap between the arterial and the lymphatic system pressure.

  This assumption implies that the interaction between the cells and the liquid phase is negligible with respect to the interaction between the cells and the extracellular matrix.

In light of these considerations, Equation (5.16) for the momentum balance equations of the cells phase reduces to

$$\nabla \cdot \mathbb{T}_c + \overline{\mathbf{m}}_{cm} = 0. \tag{5.24}$$

Moreover, substituting all the above definitions, Equation (5.17) for the momentum balance of the liquid phase becomes

$$-\phi_\ell\nabla p - \phi_\ell\phi_m\mu[\mathbb{K}(\phi_\ell)]^{-1}\mathbf{v}_\ell - \phi_c\phi_\ell\mu[\mathbb{K}(\phi_\ell)]^{-1}\mathbf{v}_\ell = 0. \tag{5.25}$$

By simple calculations, from (5.25) we obtain the expression for the fluid phase $\mathbf{v}_\ell$, so that the system of equations for the momentum balance laws reads as

$$\begin{cases} \nabla \cdot (-\Sigma(\phi_c)\mathbb{I}) - \big[\mathbb{M}(\phi_c,\phi_m)\big]^{-1}\mathbf{v}_c = 0 & (5.26) \\ \mathbf{v}_\ell = -\dfrac{1}{1-\phi_\ell}\dfrac{\mathbb{K}(\phi_\ell)}{\mu}\nabla p, & (5.27) \end{cases}$$

with $\phi_c + \phi_\ell = \phi_{max} < 1$.
Now, starting from Equation (5.26) it is possible to compute the cells velocity, that assumes the following expression:

$$\mathbf{v}_c = -\mathbb{M}(\phi_c,\phi_m)\Sigma'(\phi_c)\nabla\phi_c. \tag{5.28}$$

5.1.2 The mass balance equations

Let us focus now on the mass balance equations.
Substituting the expression (5.28) into (5.13), the mass balance equation for the cells phase is

$$\frac{\partial\phi_c}{\partial t} - \nabla \cdot \Big(\phi_c\mathbb{M}(\phi_c,\phi_m)\Sigma'(\phi_c)\nabla\phi_c\Big) = \Gamma_c. \tag{5.29}$$

Similarly, starting from Equation (5.14) and replacing the liquid phase velocity with its expanded form given by (5.27), the mass balance equation for the liquid phase reads as

$$\frac{\partial \phi_\ell}{\partial t} - \nabla \cdot \left(\frac{\phi_\ell}{1-\phi_\ell} \frac{\mathbb{K}(\phi_\ell)}{\mu} \nabla p \right) = \Gamma_\ell. \tag{5.30}$$

At this point, it is convenient to define the structure of the mass exchange rates Γ_c and Γ_ℓ, also recalling that we previously assumed $\Gamma_m \approx 0$.
Let us consider that, in the formulation of Γ_c, we do not take into account the natural decay (apoptosis) of the cells but only their proliferation.
Therefore, since cells can grow according to the available nutrients and the presence of other cells, we define

$$\Gamma_c = \phi_c S_c(\phi_c, c), \tag{5.31}$$

with

$$S_c(\phi_c, c) = \gamma(\phi_{max} - \phi_c)(c - c_{ref})_+. \tag{5.32}$$

Here, γ is the cell duplication rate and c_{ref} is the minimum oxygen concentration over which cells can proliferate.
For what concerns Γ_ℓ, we must take into account the fact that the cells and the lymphatic system both absorb liquid, which is also exchanged with the vasculature.
For these reasons we can write the exchange rate Γ_ℓ as

$$\Gamma_\ell = -\phi_c S_c(c, \phi_c) - \phi_\ell \beta_p^{LS} \frac{S}{V}(p - p_{LS}) + \sum_{i \in Y^k} \hat{f}_p^i \delta_{\Lambda_i^k}. \tag{5.33}$$

Now it is useful to provide a specification about the flux across the vessel walls represented by the third term on the r.h.s of (5.33), which must be considered *from* the vessels *to* the tissue. Moreover, this is also useful to understand the derivation of the trascapillary flux variables already introduced in the fist part of this work, in particular through Equations (2.16) and (2.43).

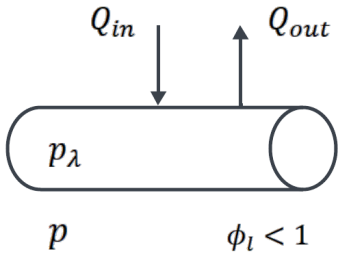

Figure 5.1: Flux direction

Let us suppose to work in the 3D-3D framework so, looking at Figure (5.1), we can define the trans-capillary flux as

$$Q = Q_{out} - Q_{in}, \tag{5.34}$$

where the quantities

$$Q_{out} = \beta_p \Big(p_\lambda - p - \sigma \Delta p_{onc} \Big)_+ \tag{5.35}$$

and

$$Q_{in} = \phi_\ell \beta_p \Big(p + \sigma \Delta p_{onc} - p_\lambda \Big)_+ \tag{5.36}$$

are the outgoing and the incoming fluxes, respectively.
Moreover, p is the interstitial pressure and p_λ is the tridimensional pressure inside the blood vessels and we set $\sigma = 1$.
We also observe that we assume to neglect to positive part in order to avoid non-linearities in the resolution of the corresponding 3D-1D numerical method.
In light of this, when we come back to the 3D-1D scenario, the term f_p^i reads as

$$f_p^i = 2\pi R \beta_p [(\hat{p}_i - \check{p}_i - \Delta p_{onc}) - \check{\phi}_\ell (\check{p}_i - \hat{p}_i + \Delta p_{onc})], \tag{5.37}$$

where $\hat{p}_i$ and $\check{p}_i$ are the same quantities defined in Equations (2.14) and (2.15), while $\check{\phi}_\ell$ is the trace of ϕ_ℓ on the lateral surface of the vessels.
Now, taking into account all the above considerations, we can write the mass balance equations in the tridimensional domain:

$$\begin{cases} \dfrac{\partial \phi_c}{\partial t} - \nabla \cdot (\phi_c \mathbb{M}(\phi_c, \phi_m) \Sigma'(\phi_c) \nabla \phi_c) = \phi_c S_c(\phi_c, c), & (5.38) \\ \dfrac{\partial \phi_\ell}{\partial t} - \nabla \cdot \left(\dfrac{\phi_\ell}{1 - \phi_\ell} \dfrac{\mathbb{K}(\phi_\ell)}{\mu} \nabla p \right) = -\phi_c S_c(c, \phi_c) - \phi_\ell \beta_p^{LS} \dfrac{S}{V} (p - p_{LS}) + \\ \qquad + \displaystyle\sum_{i \in Y^k} 2\pi R \beta_p (1 + \check{\phi}_\ell)(\hat{p}_i - \check{p}_i - \Delta p_{onc}) \delta_{\Lambda_i^k}, & (5.39) \\ \phi_c + \phi_\ell = \phi_{max}. & (5.40) \end{cases}$$

We also observe that, since the first equation to be solved is (5.38), exploiting (5.40) we have that

$$\phi_\ell = \phi_{max} - \phi_c \quad \Longrightarrow \quad \frac{\partial \phi_\ell}{\partial t} = -\frac{\partial \phi_c}{\partial t} \tag{5.41}$$

and (5.39) reduces to an equation for the interstitial pressure.

5.2 The nutrients problem

In the above sections we introduced the tumor growth dynamics and, to this aim, we adopted a multiphase model that allowed us to obtain the equations for the cells dynamics and the pressure in the tridimensional domain.
Now we want to restore also the chemicals dynamics that, as shown in the previous chapters, have a pivotal role in the angiogenesis process.

We assume that oxygen and VEGF are dissolved in the liquid phase, so it is necessary to reformulate the corresponding equations considering that ϕ_ℓ occupies only a portion of the domain Ω.
In this perspective, let us focus on the generic chemical $c_i(\mathbf{x}, t)$, whose evolution is regulated by

$$\frac{\partial(\phi_\ell c_i)}{\partial t} + \nabla \cdot \left(\phi_\ell c_i \mathbf{v}_\ell\right) = \nabla \cdot \left(\phi_\ell \mathbb{D} \nabla c_n\right) + \Gamma_\ell c_i + S_i \tag{5.42}$$

where $\mathbf{v}_\ell$ is nothing but (5.27) and S_i is a source of substances not related to liquid production or absorption.
Expanding the derivatives and recalling the mass balance equation for the liquid phase, Equation (5.42) reduces to

$$\phi_\ell \frac{\partial c_i}{\partial t} + \phi_\ell \mathbf{v}_\ell \cdot \nabla c_i = \nabla \cdot \left(\phi_\ell \mathbb{D} \nabla c_n\right) + S_i. \tag{5.43}$$

This structure can be adopted to provide the governing laws for the evolution of oxygen and VEGF in the tissue. In particular, if we consider the oxygen dynamics in the tridimensional sample we can write

$$\phi_\ell \frac{\partial c}{\partial t} - \nabla \cdot \left(\phi_\ell D_c \nabla c\right) + \left(\frac{\phi_\ell}{1-\phi_\ell} \frac{\mathbb{K}(\phi_\ell)}{\mu} \nabla p\right) \nabla c + \phi_\ell m_c c + \\ - \sum_{i \in Y^k} 2\pi R \beta_c (1 + \check{\phi_\ell})(\hat{c} - \check{c}) \delta_{\Lambda_i^k} = 0. \tag{5.44}$$

To be more precise, m_c is related to oxygen metabolization and it is equivalent to (2.40), while

$$\hat{f}_c^i := -2\pi R \beta_c (1 + \check{\phi_\ell})(\hat{c} - \check{c}) \tag{5.45}$$

is the trans-capillary flux contribution, whose definition is totally comparable to (5.37).
Analogously, for what concerns the VEGF evolution we can write the following equation

$$\phi_\ell \frac{\partial g}{\partial t} - \nabla \cdot \left(\phi_\ell D_g \nabla g\right) + \left(\frac{\phi_\ell}{1-\phi_\ell} \frac{\mathbb{K}(\phi_\ell)}{\mu} \nabla p\right) \nabla g + \phi_\ell \sigma g + \\ + \sum_{i \in Y^k} 2\pi R \tilde{\sigma} \check{\phi_\ell} \check{g} \delta_{\Lambda_i^k} = r_g \phi_c f_{VEGF}(c), \tag{5.46}$$

where all the definitions given in the previous chapters still hold, with the only difference that the source of VEGF now is not defined by an arbitrary function but it corresponds to the cells distribution.

5.3 The tumor growth model

Now we can finally collect all the equations defined above and provide the system that describes both the angiogenesis and the tumor growth dynamics.

$$\frac{\partial \phi_c}{\partial t} - \nabla \cdot \Big(F_c(\phi_c) \nabla \phi_c \Big) + S_c(\phi_c, c)\phi_c = 0 \tag{5.47}$$

$$\phi_\ell = \phi_{max} - \phi_c \tag{5.48}$$

$$\begin{aligned} &- \nabla \cdot \left(\frac{\phi_\ell}{1-\phi_\ell} \frac{\mathbb{K}(\phi_\ell)}{\mu} \nabla p \right) + \phi_\ell \beta_p^{LS} \frac{S}{V} (p - p_{LS}) + \\ &- \sum_{i \in Y^k} 2\pi R \beta_p (1 + \check{\phi_\ell}) (\hat{p} - \check{p} - \Delta p_{onc}) \delta_{\Lambda_i^k} = - \frac{\partial \phi_\ell}{\partial t} + S_c(\phi_c, c)\phi_c \end{aligned} \tag{5.49}$$

$$- \frac{\partial}{\partial s} \left(\frac{\pi R^4}{8\mu} \frac{\partial \hat{p}}{\partial s} \right) + \sum_{i \in Y^k} 2\pi R \beta_p (1 + \check{\phi_\ell}) (\hat{p} - \check{p} - \Delta p_{onc}) \delta_{\Lambda_i^k} = 0 \tag{5.50}$$

$$\begin{aligned} &\phi_\ell \frac{\partial c}{\partial t} - \nabla \cdot \Big(\phi_\ell D_c \nabla c \Big) + \left(\frac{\phi_\ell}{1-\phi_\ell} \frac{\mathbb{K}(\phi_\ell)}{\mu} \nabla p \right) \nabla c + \phi_\ell m_c c + \\ &- \sum_{i \in Y^k} 2\pi R \beta_c (1 + \check{\phi_\ell}) (\hat{c} - \check{c}) \delta_{\Lambda_i^k} = 0 \end{aligned} \tag{5.51}$$

$$\pi R^2 \frac{\partial \hat{c}}{\partial t} - \frac{\partial}{\partial s} \left(\pi R^2 \tilde{D}_c \frac{\partial \hat{c}}{\partial s} \right) + \left(\frac{\pi R^4}{8\mu} \frac{\partial \hat{p}}{\partial s} \right) \frac{\partial \hat{c}}{\partial s} + \sum_{i \in Y^k} 2\pi R \beta_c (1 + \check{\phi_\ell}) (\hat{c} - \check{c}) \delta_{\Lambda_i^k} = 0 \tag{5.52}$$

$$\begin{aligned} \phi_\ell \frac{\partial g}{\partial t} - \nabla \cdot \Big(\phi_\ell D_g \nabla g \Big) + \left(\frac{\phi_\ell}{1-\phi_\ell} \frac{\mathbb{K}(\phi_\ell)}{\mu} \nabla p \right) \nabla g + \phi_\ell \sigma g + \sum_{i \in Y^k} 2\pi R \tilde{\sigma} \check{\phi_\ell} \check{g} \delta_{\Lambda_i^k} = \\ = r_g \phi_c f_{VEGF}(c). \end{aligned} \tag{5.53}$$

In order to to simplify the notation, we do not report explicitly the independent variables, but each physical quantity must be considered as a function of space $\mathbf{x}$ and time t. Moreover, the functions $F_c(\phi_c)$ and $S_c(\phi_c, c)$ are defined as follows

$$F_c(\phi_c) = M \phi_c \Sigma'(\phi_c), \tag{5.54}$$

$$S_c(\phi_c, c) = -\gamma(\phi_{max} - \phi_c)(c - c_{ref})_+, \tag{5.55}$$

where we assume that the motility tensor $\mathbb{M}(\phi_c, \phi_m)$ is isotropic and so, it is proportional to M through the identity $\mathbb{I}$. In addition, we define

$$\Sigma(\phi_c) = E\phi_c \frac{\phi_c - \phi_0}{\phi_{max} - \phi_c} \tag{5.56}$$

and

$$\Sigma'(\phi_c) = \frac{2E\phi_c\phi_{max} - E\phi_c^2 - E\phi_0\phi_{max}}{(\phi_c - \phi_{max})^2}. \tag{5.57}$$

For what concerns the initial and boundary conditions of pressure, oxygen and VEGF problems, they are the same reported in the first part of this work.
More specifically, in order to avoid repetitions, we refer to Equations (2.23)-(2.27) for the initial and boundary conditions of the pressure problem, (2.46)-(2.53) for the oxygen ones and (2.55)-(2.57) for the VEGF ones.
In particular, as in the previous part, the initial conditions of pressure, oxygen and VEGF are obtained solving the correspondent problems in steady state conditions.
Now, the main novelty is the introduction of the cells dynamics.
Since we suppose that cells cannot enter the vasculature, we do not need any interface conditions that model the trans-capillary flux of the cells.
We only have to establish the behaviour of the external boundary of the spatial domain and its initial condition: in this perspective we impose a homogeneous Neumann's boundary conditions on the external boundary while for the initial condition we set an arbitrary distribution. In mathematical terms, this can be written as

$$\nabla\phi_c(\mathbf{x}, t) \cdot \mathbf{n}(\mathbf{x}) = 0 \qquad \mathbf{x} \in \partial\mathcal{D}, \tag{5.58}$$

$$\phi_c(\mathbf{x},0) = \phi_c^{init}(\mathbf{x}) \qquad \mathbf{x} \in \mathcal{D}. \tag{5.59}$$

Chapter 6

Numerical Method

In this section we provide the numerical method that allows us to obtain the solution of the tumor growth problem.
To this aim, it is worth to note that the same methods presented in Section (3.1) are still applicable to the angiogenic cascade.
More specifically, pressure, oxygen, VEGF and network growth model can be solved with the same techniques introduced in the first part of this work.
Nevertheless, it is worth to note that the coefficients of the PDE problems involve now many non-linear terms and so we must introduce suitable quadrature rules.
Let us focus now on the main novelty with respect to the previous part of this work: the introduction of the variable ϕ_c and its corresponding governing law, which is given by:

$$\frac{\partial \phi_c}{\partial t} - \nabla \cdot \Big(F_c(\phi_c) \nabla \phi_c \Big) + S_c(\phi_c, c)\phi_c = 0, \tag{6.1}$$

where the functions $F_c(\phi_c)$ and $S_c(\phi_c, c)$ are defined by (5.54) and (5.55), respectively.
Furthermore, Equation (6.1) is defined only in the tridimensional domain, since we assume that cells cannot enter the vasculature.
Consequently, we do not have to introduce any mathematical description of cells behavior inside the one-dimensional domain: in this perspective, no 3D-1D coupling model is necessary to obtain the solution ϕ_c and, to achieve our purpose, we adopt a finite element discretization with a backward Euler's method for the semi-discretization in time.
Moreover, since we obtain a non-linear problem, we introduce the Newton's method for its resolution.

6.1 The Newton's method

In this section we show how to implement the Newton's method in our specific problem.
Our starting point is

$$\frac{\partial \phi_c}{\partial t} - \nabla \cdot \Big(F_c(\phi_c) \nabla \phi_c \Big) + S_c(\phi_c, c)\phi_c = 0 \tag{6.2}$$

and we provide its time discretization, introducing the following notation

$$\varepsilon := \phi_c^{k+1} \tag{6.3}$$

$$\varepsilon_0 := \phi_c^k \tag{6.4}$$

to indicate the approximation of the solution at time $k+1$ and k, respectively.
We employ the Backward Euler's scheme that, thanks to definitions (6.3) and (6.4), can be written as

$$\frac{\varepsilon - \varepsilon_0}{\Delta t} - \nabla \cdot \Big(F_c(\varepsilon)\nabla\varepsilon\Big) + S_c(\varepsilon, c^k)\varepsilon = 0. \tag{6.5}$$

Here, if we take the approximation of the oxygen at time $k+1$, we would get a non-linearity in the corresponding 3D-1D optimization problem, since the dependence from ϕ_c contained in its equation should be resolved with a non-linear Newton's method. In this framework, for the sake of simplicity, we decide to consider the oxygen at time-step k in order to treat it as a known term.
Now, we also have to provide the spatial discretization of the problem, so we exploit the tetrahedral mesh $\mathcal{T}$ of the the domain Ω and the linear Lagrangian basis functions

$$\{\varphi_j\}_{j=1}^N$$

that we have already defined in section (3.2).
These allows us to write $\forall i \in \{1, \dots, N\}$

$$G_i(\varepsilon) := \int_\Omega \frac{\varepsilon - \varepsilon_0}{\Delta t}\varphi_i d\omega + \int_\Omega F_c(\varepsilon)\nabla\varepsilon \cdot \nabla\varphi_i d\omega + \int_\Omega S_c(\varepsilon, c^k)\varepsilon\varphi_i d\omega \tag{6.6}$$

where $G_i(\varepsilon)$ is the generic component of the non-linear system

$$\mathbf{G}(\varepsilon) = 0 \tag{6.7}$$

that we want to solve with the Newton's method, being

$$\mathbf{G}(\varepsilon) = \begin{bmatrix} G_1(\varepsilon) \\ \vdots \\ G_N(\varepsilon) \end{bmatrix}. \tag{6.8}$$

In order to apply this method, the first step is to linearize the system thanks to the Taylor expansion series, obtaining

$$\mathbf{G}(\varepsilon^{(n+1)}) = \mathbf{G}(\varepsilon^{(n)}) + \mathbb{J}(\varepsilon^{(n)})(\varepsilon^{(n+1)} - \varepsilon^{(n)}) + O((\varepsilon^{(n)})^2). \tag{6.9}$$

In particular, recalling that the Newton's method is an iterative technique, $\varepsilon^{(n+1)}$ is the approximation of the solution we are looking for at the $(n+1)$th iteration of the method, $\varepsilon^{(n)}$ is its approximation at the nth iteration and $\mathbb{J}(\varepsilon^{(n)})$ is the Jacobian matrix of $\mathbf{G}(\varepsilon^{(n)})$.
In light of this, the relation (6.9) allows us to write

$$\mathbf{G}(\varepsilon^{(n+1)}) \approx \mathbf{G}(\varepsilon^{(n)}) + \mathbb{J}(\varepsilon^{(n)})(\varepsilon^{(n+1)} - \varepsilon^{(n)}) = 0, \tag{6.10}$$

that reduces to

$$\mathbb{J}(\varepsilon^{(n)})(\varepsilon^{(n+1)} - \varepsilon^{(n)}) = -\mathbf{G}(\varepsilon^{(n)}). \tag{6.11}$$

This way, at each iteration of the method we have to solve a linear system to get $\varepsilon^{(n+1)}$ and we set suitable stopping criteria to arrest it.
At the end of the iterations, under proper convergence hypotheses, we obtain the solution of the problem ε, i.e. $\varepsilon^{(n)} \to \varepsilon$.
Now, since ε and ε_0 are variables defined in the tridimensional domain, their spatial discretizations are given by

$$\varepsilon = \sum_{j=1}^{N} \varepsilon_j \varphi_j \tag{6.12}$$

$$\varepsilon_0 = \sum_{j=1}^{N} \varepsilon_{0,j} \varphi_j. \tag{6.13}$$

Substituting them inside (6.6) we obtain

$$\begin{aligned} G_i(\varepsilon) = \int_\Omega \frac{\sum_{j=1}^N \varepsilon_j \varphi_j - \sum_{j=1}^N \varepsilon_{0,j} \varphi_j}{\Delta t} \varphi_i d\omega + \int_\Omega F_c(\varepsilon) \nabla \Big(\sum_{j=1}^N \varepsilon_j \varphi_j \Big) \cdot \nabla \varphi_i d\omega + \\ + \int_\Omega S_c(\varepsilon, c^k) \Big(\sum_{j=1}^N \varepsilon_j \varphi_j \Big) \varphi_i d\omega. \end{aligned} \tag{6.14}$$

Now, we can rewrite the first term of (6.14) as

$$\frac{1}{\Delta t} \int_\Omega \left[\sum_{j=1}^N \varepsilon_j \varphi_j - \sum_{j=1}^N \varepsilon_{0,j} \varphi_j \right] \varphi_i d\omega = \frac{1}{\Delta t} \sum_{j=1}^N \varepsilon_j \int_\Omega \varphi_j \varphi_i d\omega - \frac{1}{\Delta t} \sum_{j=1}^N \varepsilon_{0,j} \int_\Omega \varphi_j \varphi_i d\omega \tag{6.15}$$

the second as

$$\int_\Omega F_c(\varepsilon) \nabla \Big(\sum_{j=1}^N \varepsilon_j \varphi_j \Big) \cdot \nabla \varphi_i d\omega = \sum_{j=1}^N \varepsilon_j \int_\Omega F_c(\varepsilon) \nabla \varphi_j \cdot \nabla \varphi_i d\omega. \tag{6.16}$$

and the third as

$$\int_\Omega S_c(\varepsilon, c^k) \Big(\sum_{j=1}^N \varepsilon_j \varphi_j \Big) \varphi_i d\omega = \sum_{j=1}^N \varepsilon_j \int_\Omega S_c(\varepsilon, c^k) \varphi_j \varphi_i d\omega. \tag{6.17}$$

Now it is useful to compute also the Jacobian matrix of $\mathbf{G}(\varepsilon)$, whose generic component is

$$J_{il}(\varepsilon) = \frac{\partial G_i(\varepsilon)}{\partial \varepsilon_l}. \tag{6.18}$$

By simple calculations, its first term is given by

$$\frac{\partial}{\partial \varepsilon_l}\int_\Omega \frac{\sum_{j=1}^N \varepsilon_j\varphi_j - \sum_{j=1}^N \varepsilon_{0,j}\varphi_j}{\Delta t}\varphi_i d\omega = \frac{1}{\Delta t}\int_\Omega \Big(\sum_{j=1}^N \frac{\partial \varepsilon_j}{\partial \varepsilon_l}\varphi_j\Big)\varphi_i d\omega = \frac{1}{\Delta t}\int_\Omega \varphi_l\varphi_i d\omega, \tag{6.19}$$

the second by

$$\begin{aligned}
&\frac{\partial}{\partial \varepsilon_l}\int_\Omega F_c(\varepsilon)\nabla\Big(\sum_{j=1}^N \varepsilon_j\varphi_j\Big)\cdot\nabla\varphi_i d\omega = \\
&= \int_\Omega \frac{\partial F_c(\varepsilon)}{\partial \varepsilon}\frac{\partial \varepsilon}{\partial \varepsilon_l}\nabla\Big(\sum_{j=1}^N \varepsilon_j\varphi_j\Big)\cdot\nabla\varphi_i d\omega + \int_\Omega F_c(\varepsilon)\frac{\partial}{\partial \varepsilon_l}\Big(\sum_{j=1}^N \varepsilon_j\nabla\varphi_j\Big)\cdot\nabla\varphi_i d\omega = \\
&= \int_\Omega F_c'(\varepsilon)\nabla\varepsilon\varphi_l\cdot\nabla\varphi_i d\omega + \int_\Omega F_c(\varepsilon)\nabla\varphi_l\cdot\nabla\varphi_i d\omega
\end{aligned} \tag{6.20}$$

and the third by

$$\begin{aligned}
&\frac{\partial}{\partial \varepsilon_l}\int_\Omega S_c(\varepsilon, c^k)\Big(\sum_{j=1}^N \varepsilon_j\varphi_j\Big)\varphi_i d\omega = \\
&= \int_\Omega \frac{\partial S_c(\varepsilon, c^k)}{\partial \varepsilon_l}\frac{\partial \varepsilon}{\partial \varepsilon_l}\Big(\sum_{j=1}^N \varepsilon_j\varphi_j\Big)\varphi_i d\omega + \int_\Omega S_c(\varepsilon, c^k)\frac{\partial}{\partial \varepsilon_l}\Big(\sum_{j=1}^N \varepsilon_j\varphi_j\Big)\varphi_i d\omega = \\
&= \int_\Omega S_c'(\varepsilon, c^k)\varepsilon\varphi_l\varphi_i d\omega + \int_\Omega S_c(\varepsilon, c^k)\varphi_l\varphi_i d\omega.
\end{aligned} \tag{6.21}$$

In particular, we exploit the following properties

$$\begin{aligned}
&\frac{\partial \varepsilon}{\partial \varepsilon_l} = \frac{\partial}{\partial \varepsilon_l}\Big(\sum_{j=1}^N \varepsilon_j\varphi_j\Big) = \sum_{j=1}^N \delta_{l,j}\varphi_j = \varphi_l, \\
&\frac{\partial}{\partial \varepsilon_l}\Big(\nabla\Big(\sum_{j=1}^N \varepsilon_j\varphi_j\Big)\Big) = \nabla\Big(\sum_{j=1}^N \frac{\partial}{\partial \varepsilon_l}\varepsilon_j\varphi_j\Big) = \sum_{j=1}^N \delta_{l,j}\nabla\varphi_j = \nabla\varphi_l.
\end{aligned} \tag{6.22}$$

Now, since we have obtained the expressions for $G_i(\varepsilon)$ and $J_{il}(\varepsilon)$ without taking into account that the variable ε should be considered as the approximation of the solution at the nth iteration of the method, we finally introduce

$$\varepsilon^{(n)} = \sum_{j=1}^N \varepsilon_j^{(n)}\varphi_j, \tag{6.23}$$

i.e. the discretization of the approximation of the solution at the nth iteration of the method.

So, in light of all the above considerations, we can substitute (6.13) and (6.23) inside all the proposed calculations and then we obtain

$$\begin{aligned} G_i(\varepsilon^{(n)}) =& \frac{1}{\Delta t}\sum_{j=1}^{N}\varepsilon_j^{(n)}\int_\Omega \varphi_j\varphi_i d\omega - \frac{1}{\Delta t}\sum_{j=1}^{N}\varepsilon_{0,j}\int_\Omega \varphi_j\varphi_i d\omega + \\ &+\sum_{j=1}^{N}\varepsilon_j^{(n)}\int_\Omega F_c(\varepsilon^{(n)})\nabla\varphi_j\cdot\nabla\varphi_i d\omega + \sum_{j=1}^{N}\varepsilon_j^{(n)}\int_\Omega S_c(\varepsilon^{(n)},c^k)\varphi_j\varphi_i d\omega, \end{aligned} \tag{6.24}$$

$$\begin{aligned} J_{il}(\varepsilon^{(n)}) = \frac{1}{\Delta t}\int_\Omega \varphi_l\varphi_i d\omega + \int_\Omega F_c'(\varepsilon^{(n)})\nabla\varepsilon\varphi_l\cdot\nabla\varphi_i d\omega + \int_\Omega F_c(\varepsilon^{(n)})\nabla\varphi_l\cdot\nabla\varphi_i d\omega + \\ + \int_\Omega S_c'(\varepsilon^{(n)},c^k)\varepsilon\varphi_l\varphi_i d\omega + \int_\Omega S_c(\varepsilon^{(n)},c^k)\varphi_l\varphi_i d\omega. \end{aligned} \tag{6.25}$$

6.2 Matrix formulation

Now it is useful to show how the discrete formulation of the method presented in the section above is implemented.
We take into account the fact that we solve the following system

$$\mathbb{J}(\varepsilon^{(n)})(\varepsilon^{(n+1)}-\varepsilon^{(n)}) = -\mathbf{G}(\varepsilon^{(n)}), \tag{6.26}$$

where the variables $\varepsilon^{(n)}$ and $\varepsilon^{(n+1)}$ stand for the approximation of the solution ε at the nth and $(n+1)$th iteration of the Newton's method, respectively.
First of all, we have to provide the discretization of the Jacobian matrix $\mathbb{J}(\varepsilon^{(n)})$, whose definition is given by (6.25).
To achieve this purpose, we introduce the following matrices

$$\begin{aligned} &\mathbf{A}(\varepsilon^{(n)}) \in \mathbb{R}^{N\times N} \text{ s.t. } A_{i,l}(\varepsilon^{(n)}) = \int_\Omega F_c(\varepsilon^{(n)})\nabla\varphi_l\cdot\nabla\varphi_i d\omega \\ &\dot{\mathbf{A}}(\varepsilon^{(n)}) \in \mathbb{R}^{N\times N} \text{ s.t. } \dot{A}_{i,l}(\varepsilon^{(n)}) = \int_\Omega F_c'(\varepsilon^{(n)})\nabla\varepsilon^{(n)}\varphi_l\cdot\nabla\varphi_i d\omega \\ &\mathbf{M}(\varepsilon^{(n)}) \in \mathbb{R}^{N\times N} \text{ s.t. } M_{i,l}(\varepsilon^{(n)}) = \int_\Omega S_c(\varepsilon^{(n)},c^k)\varphi_l\varphi_i d\omega \\ &\dot{\mathbf{M}}(\varepsilon^{(n)}) \in \mathbb{R}^{N\times N} \text{ s.t. } \dot{M}_{i,l}(\varepsilon^{(n)}) = \int_\Omega S_c'(\varepsilon^{(n)},c^k)\varepsilon^{(n)}\varphi_l\varphi_i d\omega \\ &\mathbf{B} \in \mathbb{R}^{N\times N} \text{ s.t. } B_{i,l} = \frac{1}{\Delta t}\int_\Omega \varphi_l\varphi_i d\omega. \end{aligned} \tag{6.27}$$

Substituting in (6.25) the definitions suggested in (6.27), the discrete formulation of the Jacobian matrix at the nth iteration is given by

$$\mathbb{J}(\varepsilon^{(n)}) = \mathbf{B} + \mathbf{A}(\varepsilon^{(n)}) + \dot{\mathbf{A}}(\varepsilon^{(n)}) + \mathbf{M}(\varepsilon^{(n)}) + \dot{\mathbf{M}}(\varepsilon^{(n)}). \tag{6.28}$$

Furthermore, we also need to provide the discretization of the term $\mathbf{G}(\varepsilon^{(n)})$: in this perspective, we firstly introduce the definitions (6.27) inside the Equations (6.24).
To be more precise, looking at the first and second addends in (6.24) we get

$$\frac{1}{\Delta t}\sum_{j=1}^{N}\varepsilon_j^{(n)}\int_\Omega \varphi_j\varphi_i d\omega - \frac{1}{\Delta t}\sum_{j=1}^{N}\varepsilon_{0,j}\int_\Omega \varphi_j\varphi_i d\omega = \sum_{j=1}^{N}\varepsilon_j^{(n)}B_{i,j} - \sum_{j=1}^{N}\varepsilon_{0,j}B_{i,j}. \tag{6.29}$$

For what concerns the third, instead, we obtain

$$\int_\Omega F_c(\varepsilon^{(n)})\nabla\Big(\sum_{j=1}^{N}\varepsilon_j^{(n)}\varphi_j\Big)\cdot\nabla\varphi_i d\omega = \sum_{j=1}^{N}\varepsilon_j^{(n)}\int_\Omega F_c(\varepsilon^{(n)})\nabla\varphi_j\cdot\nabla\varphi_i d\omega = \sum_{j=1}^{N}\varepsilon_j^{(n)}A_{i,j}(\varepsilon^{(n)}) \tag{6.30}$$

and the last term in (6.24) can be rewritten as

$$\int_\Omega S_c(\varepsilon^{(n)},c^k)\Big(\sum_{j=1}^{N}\varepsilon_j^{(n)}\varphi_j\Big)\varphi_i d\omega = \sum_{j=1}^{N}\varepsilon_j^{(n)}\int_\Omega S_c(\varepsilon^{(n)},c^k)\varphi_j\varphi_i d\omega = \sum_{j=1}^{N}\varepsilon_j^{(n)}M_{i,j}(\varepsilon^{(n)}). \tag{6.31}$$

We can finally assemble all the above calculations, in order to provide the component-wise matrix formulation of (6.6)

$$G_i(\varepsilon^{(n)}) = \sum_{j=1}^{N}\varepsilon_j^{(n)}B_{i,j} - \sum_{j=1}^{N}\varepsilon_{0,j}B_{i,j} + \sum_{j=1}^{N}\varepsilon_j^{(n)}A_{i,j}(\varepsilon^{(n)}) + \sum_{j=1}^{N}\varepsilon_j^{(n)}M_{i,j}(\varepsilon^{(n)}), \tag{6.32}$$

that, more compactly, reads as

$$\mathbf{G}(\varepsilon^{(n)}) = \mathbf{B}\varepsilon^{(n)} - \mathbf{B}\varepsilon_0 + \mathbf{A}(\varepsilon^{(n)})\varepsilon^{(n)} + \mathbf{M}(\varepsilon^{(n)})\varepsilon^{(n)}, \tag{6.33}$$

To recapitulate, for the resolution of the system (6.11) we provide the discretization of the matrix $\mathbb{J}(\varepsilon^{(n)})$ and of the term $\mathbf{G}(\varepsilon^{(n)})$.
Such discrete formulations are given by

$$\mathbb{J}(\varepsilon^{(n)}) = \tilde{\mathbf{J}}(\varepsilon^{(n)}) + \mathbf{B} \tag{6.34}$$

$$\mathbf{G}(\varepsilon^{(n)}) = \tilde{\mathbf{G}}\varepsilon^{(n)} - \mathbf{B}\varepsilon_0, \tag{6.35}$$

being

$$\tilde{\mathbf{J}}(\varepsilon^{(n)}) := \mathbf{A}(\varepsilon^{(n)}) + \dot{\mathbf{A}}(\varepsilon^{(n)}) + \mathbf{M}(\varepsilon^{(n)}) + \dot{\mathbf{M}}(\varepsilon^{(n)}) \tag{6.36}$$

$$\tilde{\mathbf{G}}\varepsilon^{(n)} := \mathbf{B}\varepsilon^{(n)} + \mathbf{A}(\varepsilon^{(n)})\varepsilon^{(n)} + \mathbf{M}(\varepsilon^{(n)})\varepsilon^{(n)}. \tag{6.37}$$

In particular, as we can observe, the coefficients of the integrand functions figuring in (6.27) are not linear, so it is necessary to introduce suitable quadrature rules in order to gain their approximation.

Chapter 7

Numerical Simulations

7.1 The setting

In this section we provide some numerical results in order to understand the behavior of the dynamics of the system when we take in consideration the presence of a cancer cell population.
As we did in Chapter 4, we consider a cubic domain $\Omega = [0, L]$ in which we place a small initial vascular network with two inlets and two outlets, whose radius is set to $R = 5 \cdot 10^{-3}$ mm.
Nevertheless, differently from the previous case, the domain edge length is now given by $L = 2.5$ mm, while for the spatial discretization we consider a tetrahedral mesh in which the maximum element size, which is close to the dimension at which tumours start to activate angiogenesis, is $5 \cdot 10^{-4}$ mm
Moreover, regarding the time discretization, we consider again the same uniform time-stepping both for the growth of the network and for the Euler backward method, but this time we set $\Delta\mathcal{I}_k = \Delta t = 6$ h, while the final time is $T = 50$ days.
For what concerns the parameters of the models, the ones related to pressure, oxygen, VEGF and network growth dynamics are almost the same listed in Tables (4.1)-(4.3).
However, in this novel setting, in which we consider also the tumor growth dynamics, we have to adjust some of the values introduced in the first part of this work in order to obtain results that are more consistent with biological observations.
In this perspective, Table (7.1) collects all the parameters which are different from the ones introduces in the first part and, in addition, we also report the parameters related to the cell governing equation.
Another difference with respect to the first part of this work stands in the branching probability parameters.

$$P_{br} = \begin{cases} \dfrac{1}{1 + \exp\left(-a(g - bg_{br})\right)} & g < g_{br} \\ 1 & \text{otherwise,} \end{cases} \tag{7.1}$$

In Equation (7.1), we remind the formulation of the probability function and now we

Table 7.1: List of parameters with different values with respect to the first part of this work and new parameters related to the tumor growth dynamics.

Parameter	Value	Unit	Description	References
k	$1.0 \cdot 10^{-11}$	mm^2	Hydraulic permeability of the tissue	[6]
m_c	0.36	h^{-1}	Decay/metabolization parameter	-
c_{ext}	$1.4 \cdot 10^7$	$\frac{\text{kg}}{\text{mm} \cdot \text{h}^2}$	External oxygen concentration	[6]
r_g	0.5	h^{-1}	Rate of VEGF production by the source	-
g_{br}	$2.0 \cdot 10^{-13}$	$\frac{\text{kg}}{\text{mm}^3}$	VEGF concentration for $\mathbb{P}_{br} = 1$	-
d_{br}	$4.0 \cdot 10^{-2}$	mm	Branching distance	-
M	$1.4 \cdot 10^{-10}$	$\frac{\text{mm}^3 \cdot \text{h}}{\text{h}}$	Motility of the cells	[13]
E	$5.2 \cdot 10^7$	$\frac{\text{kg}}{\text{mm} \cdot \text{h}^2}$	Young modulus	[13]
c_{ref}	$1.4 \cdot 10^7$	$\frac{\text{kg}}{\text{mm} \cdot \text{h}^2}$	Necrotic threshold	-
γ	1/48	h^{-1}	Cells duplication rate	-
ϕ_{max}	1	-		
ϕ_0	0.5	-		

set different values for the parameters $a = 5$ mm^3/kg, which regulates the slope of the function, and $b = 3/4$ which acts on the position of the inflection point.

We provide the representation of the probability function in Figure (7.1).

We also have to observe that, in this novel setting, in which we also take into account cancer cells evolution, we assume to work with a different value of g_{br}. In particular, here we set $g_{br} = 2.0 \cdot 10^{-13}$ kg/mm^3 because, as we will show in the numerical experiments reported in the following section, the VEGF concentration in the tissue is always greater than $1 \cdot 10^{-13}$ kg/mm^3.

In this perspective, if we adopt the same branching parameters of the previous part of this work, we would obtain an excessive network development, since tip cells would be allowed to proliferate unconditionally because of the high amount of available VEGF.

Thanks to this novel combination of parameters, we can shift the threshold for the maximum branching probability in correspondence to higher values of VEGF concentration, so we can obtain a more organized network morphology.

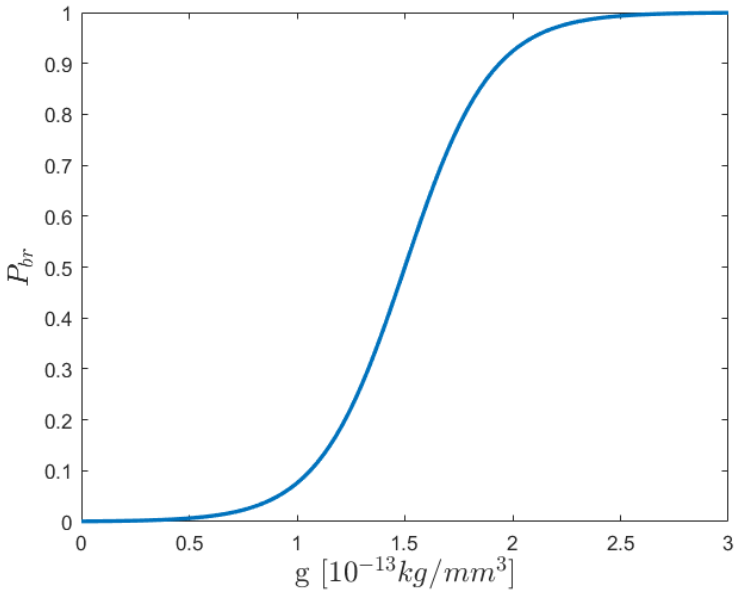

Figure 7.1: Branching probability for $g_{br} = 2 \cdot 10^{-13}$ kg/mm^3

7.2 Numerical simulations

We now provide some numerical simulations in order to analyse the growth dynamic and, first of all, we want to understand what happens when we take different initial distributions of cells.
More specifically, we carry two different experiments considering the following initial conditions:

$$\phi_c^{init}(\mathbf{x},0) = 0.5 \quad \forall \mathbf{x} \in \Omega \tag{7.2}$$

and

$$\phi_c^{init}(\mathbf{x},0) = 0.5 + 0.75 \exp\left\{ -\left[\frac{(x-1.25)^2}{20} + \frac{(y-1.25)^2}{20} + \frac{z^2}{2} \right] \right\}. \tag{7.3}$$

In the first case, as we can read in Equation (7.2), we consider a homogeneous initial distribution of cells over the whole tridimensional domain.
In the second framework, instead, Equation (7.3) has the shape of a Gaussian function to mimic an higher concentration of tumor cells close to the vascularized region
To be more precise, we report the two initial conditions in Figure (7.2): on the left panel we display the homogeneous one, while on the right we report the Gaussian one.
In the latter case we assume that, in proximity of the vasculature, the oxygen concentration is high enough to guarantee a stronger cells proliferation. Far from the vasculature, instead, cells are suffering for hypoxia condition and their concentration is lower.

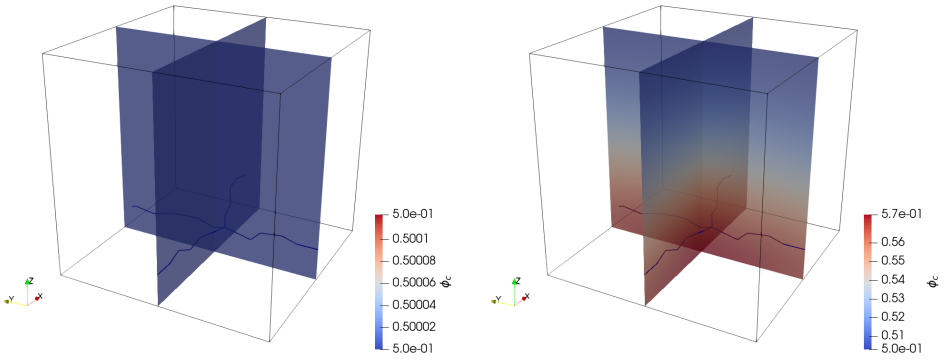

Figure 7.2: Different initial conditions for cancer cell population. Left panel: the homogeneous initial condition. Right panel: Gaussian initial condition.

For what concerns the evolution over the time of the physical quantities involved by angiogenesis and tumor growth processes, we refer to Figures (7.3), (7.6), (7.8) and (7.10), in which we report cells, VEGF, oxygen and pressure development, respectively.
In particular, in the first column of each figure, we show the results for the homogeneous initial condition, while in the second we report the evolution of the dynamics starting from the Gaussian distribution of cells. For both cases, we exhibit the outputs at 10, 30, 50 days.
Looking at Figure (7.3) we can see that, independently form the initial condition, the dynamics lead to the same qualitative behavior in which cells are much more concentrated in correspondence to the initial vascular network.
Here, in fact, the oxygen is more available and, remembering that the production of cells is regulated by Equation (5.55), when the oxygen concentration is high, cells proliferation is stronger.

The main difference between the two scenarios lies in the maximum and minimum cell concentration values, whose evolutions over the time are reported in Figure (7.4).
More specifically, looking at Figure (7.4), we can observe that, even if the Gaussian initial condition ensures a higher cell concentration in the whole domain, in the homogeneous framework the maximum cell concentration exhibits a more rapid increment in the first phases of the process. We can justify this phenomenon because cancer cells located in proximity of the initial network start proliferating very rapidly, thanks to the high amount of available oxygen.
In addition, recalling that the proliferation is proportional to $\phi_{max} - \phi_c$, as reported in Equation (5.55), when cell concentration is high, their development is reduced. In light of this, cells increment in the Gaussian setting is slower.
Successively, when the cells that were initially homogeneously distributed over the spatial domain assume a configuration similar to the Gaussian one, the two different dynamics develop with almost the same speed, even if cell concentration in the Gaussian scenario

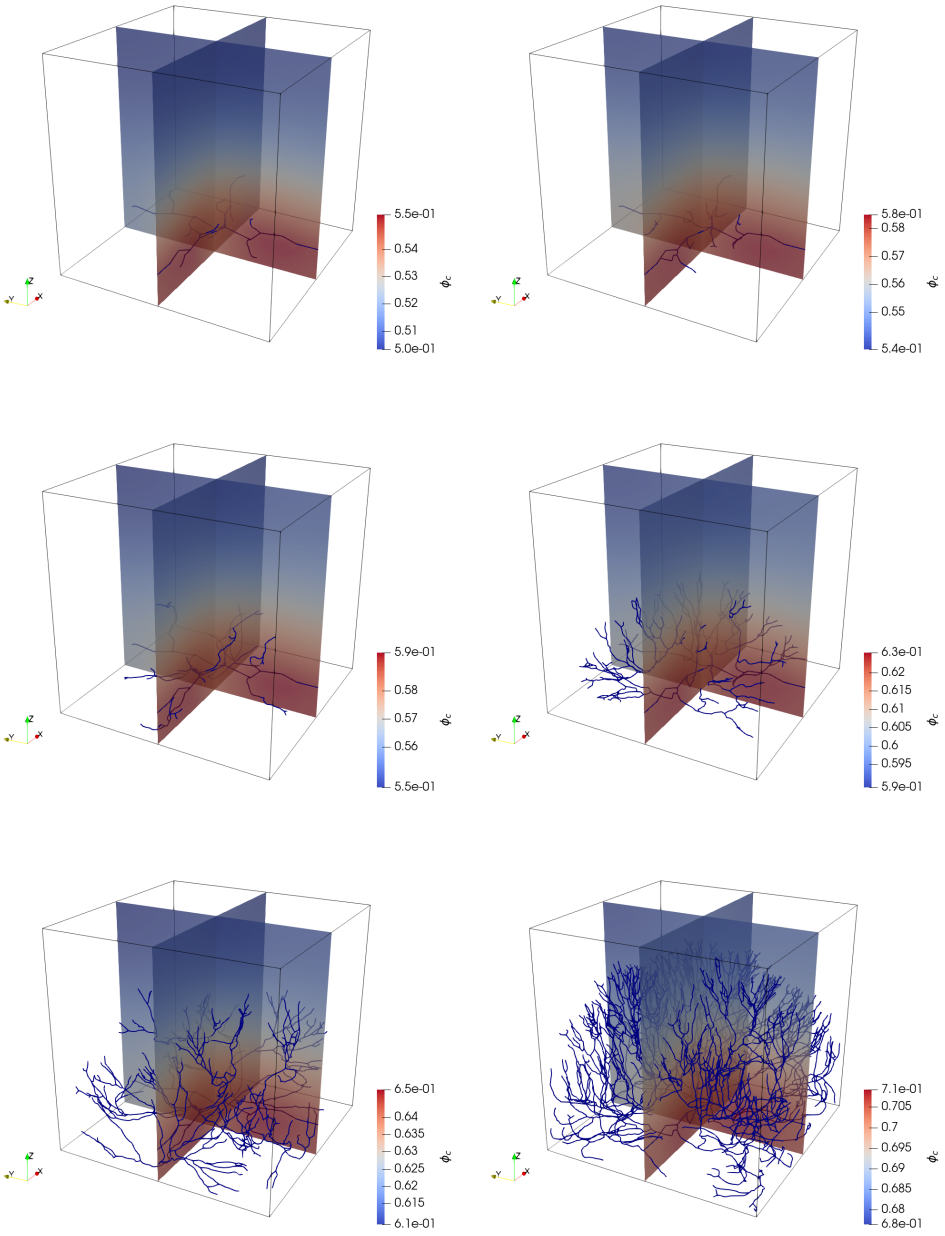

Figure 7.3: Simulation of tumor growth with parameter listed in Tables (4.1), (4.2), (4.3), (7.1). From the top to the bottom, cancer cells evolution at time 10, 30, 50 days. On the left panels: results for the homogeneous initial condition. On the right panels: results for the Gaussian initial condition.

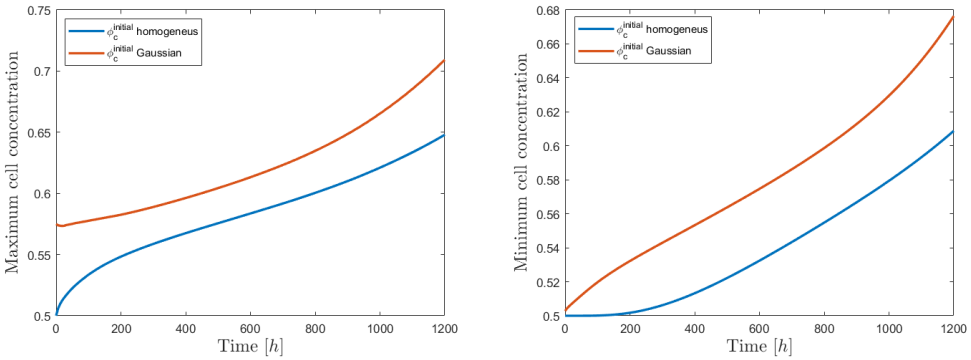

Figure 7.4: Simulation for different cell initial conditions. Left panel: evolution of the maximum cell concentration. Right panel: evolution of the minimum cell concentration.

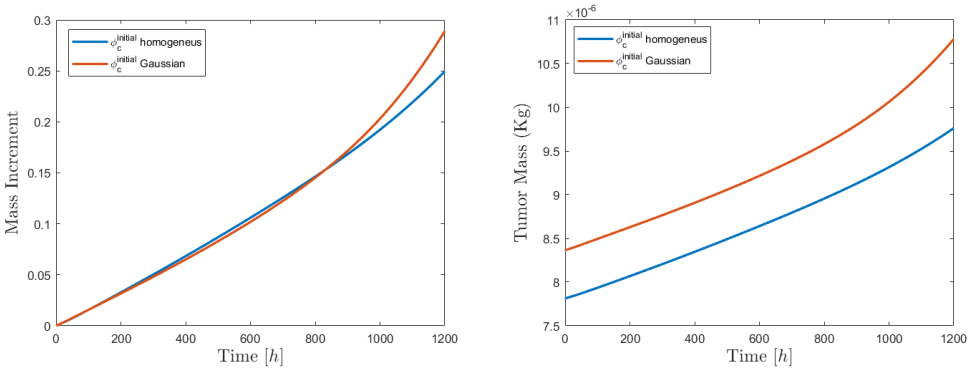

Figure 7.5: Simulation for different cell initial conditions. Left panel: relative tumor mass increment. Right panel: total tumor mass.

remains higher.
Moreover, looking at the results referred to the Gaussian setting, we can identify an increment of cell proliferation speed in the last 20 days of simulations. This happens since, as we will shown in the following, the number of vessels increases too, so the oxygenation of the tissue is higher.
Similarly, looking at Figure (7.5), we can observe that both the relative increment and the total mass of the tumor rise over the time with almost the same velocity. This happens at least for the first thirty days of simulations, successively we can observe again a differentiation between the two behaviors, and in the following we will give a proper justification of this fact.
We also recall that the total tumor mass is given by

$$M = \int_{\Omega} \rho(\mathbf{x}, t)\phi_c(\mathbf{x}, t)d\Omega, \tag{7.4}$$

with $\rho(\mathbf{x}, t) = 1 \cdot 10^{-6}$ kg/mm^3 being the cell density, assumed to be equal to the water density.
In light of this, accordingly with the formulation of the initial condition and with the above considerations regarding the maximum value of cell concentration, the total tumor mass of the Gaussian framework remains always greater than the corresponding value in the homogeneous setting.
Let us examine now the VEGF evolution: we remind that, when we consider the tumor growth dynamics, the VEGF is directly produced by cancer cells and the VEGF source depends now by the variable ϕ_c. To be more precise, we recall that its expression is given by

$$S_g = \phi_c r_g \left(- \frac{1}{1 + \exp\left(- c(\mathbf{x}, t) + c_{hypo}\right)} + 1 \right), \tag{7.5}$$

with $c_{hypo} = 11.5$ mmHg.
This formulation suggests us that the higher is the cell concentration, the stronger is the VEGF production.
In light of these considerations and since the Gaussian initial condition guarantees a greater presence of cells in the tissue, in this setting the VEGF concentration is higher.
In facts, from the biological point of view, when the number of cells increases, the quantity of oxygen needed for their survival increases too.
Recalling now that VEGF is a chemical that promotes the proliferation and the migration of the endothelial cells and since oxygen in delivered by blood vessels, when cancer cells need more nutrients, they produce more growth factor so the network can enlarge.
Consequently, as the network develops, it brings more oxygen to the tissue, allowing cancer cells to proliferate.
As previously mentioned, looking at the VEGF values reported in Figure (7.6), we can observe that they are greater that one, so we can justify our choice to shift the threshold at which the branching probability is maximum in correspondence to higher values of growth factor concentrations.
Moreover, as expected, the maximum VEGF values for the dynamics that starts from the Gaussian initial condition are greater than the homogeneous case.
The main consequence of this fact lies in the network morphology: we can see that in the Gaussian framework the resulting vasculature is much more extended and it shows a very large number of branches.
The above considerations induce us to analyse also some physical quantities directly related to the network morphology, in order to give a quantitative measure of its extension.
In particular, we focus on the number of active points over the time and on the final network length, that we report in Figure (7.7) and Table (7.2), respectively.
We remind that the active points are nothing but tip cells for which the concentration of VEGF is high enough to guarantee tip cell motion.
Accordingly with the above observations, Figure (7.7) perfectly shows the impact that higher concentrations of VEGF have on the network evolution.
Looking at the number of active points, when we consider the setting with the Gaussian initial condition, we can observe that it is greater than the corresponding value in the

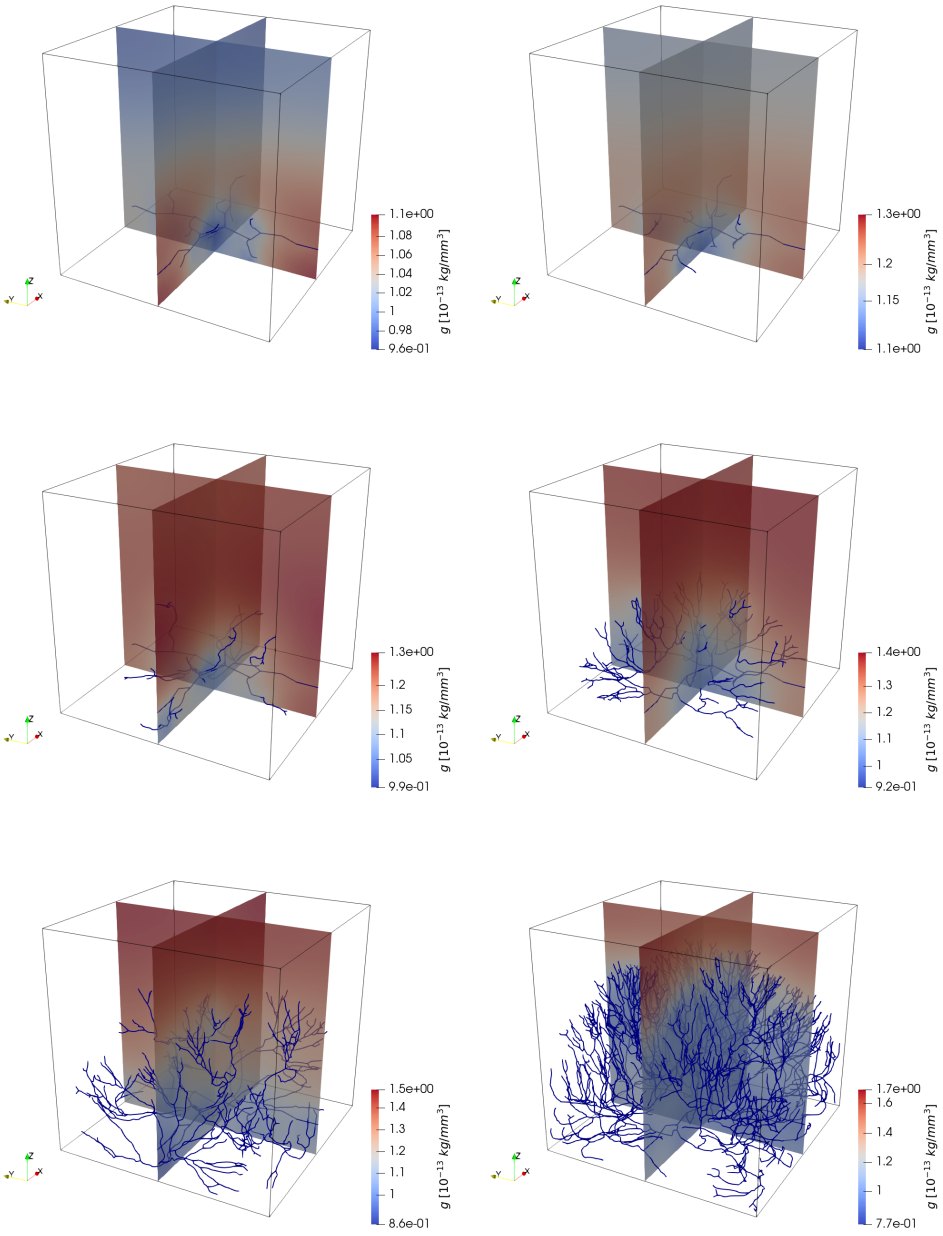

Figure 7.6: Simulation of tumor growth with parameter listed in Tables (4.1), (4.2), (4.3), (7.1). From the top to the bottom, VEGF evolution at time 10, 30, 50 days. On the left panels: results for the homogeneous initial condition. On the right panels: results for the Gaussian initial condition.

homogenous framework, since in the first case the VEGF concentration is higher.
More specifically, the number of active points in the case of Gaussian distribution is about three times the corresponding value in the case of homogeneous setting.
A similar relation is also registered in the total network length, that we report in Table (7.2), and this confirms the fact that higher VEGF concentrations correspond to a greater network extension.

Table 7.2: Total network length for different ϕ_c initial condition

Initial condition	Homogeneous ϕ_c^0	Gaussian ϕ_c^0
Total Network Length (mm)	92.3408	311.1089

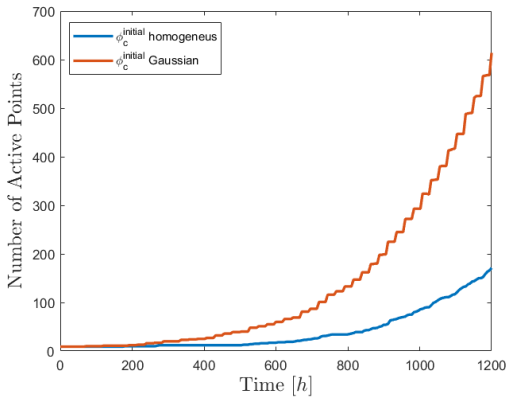

Figure 7.7: Number of active points for different cell initial condition

At this point, it is worth to examine the oxygen dynamics in order to demonstrate that when the network is more developed, the tissue is better oxygenated.
In this perspective, let us look at Figure (7.8), in which we also report the isolines corresponding to $c(\mathbf{x}, t) \approx 1.38 \cdot 10^7$ kg/(h$^2 \cdot$ mm) ≈ 8 mmHg (cyan).
As we can observe, both at 10 and 30 days, the maximum value of oxygen in the tissue is almost the same independently from the considered initial condition.
Looking at the final time $T = 50$ days, instead, we can see that in the homogeneous setting, the maximum oxygen value is given by $c(\mathbf{x}, t) \approx 14$ mmHg, while for the Gaussian initial distribution the maximum reaches the value $c(\mathbf{x}, t) \approx 20$ mmHg.
These results justify the fact that when we have a more extended vasculature, this can effectively supply a higher quantity of oxygen, allowing the cancer cells to proliferate.
Moreover, recalling again that the growth of the tumor mass is regulated by Equation (5.55), when the oxygen is more available, the proliferation is more intense.
In light of this, we can also justify the fact that, as reported in Figure (7.5), the relative mass increment in the Gaussian setting shows an increase of its velocity, with respect to the homogeneous one, after the first thirty days of simulation.

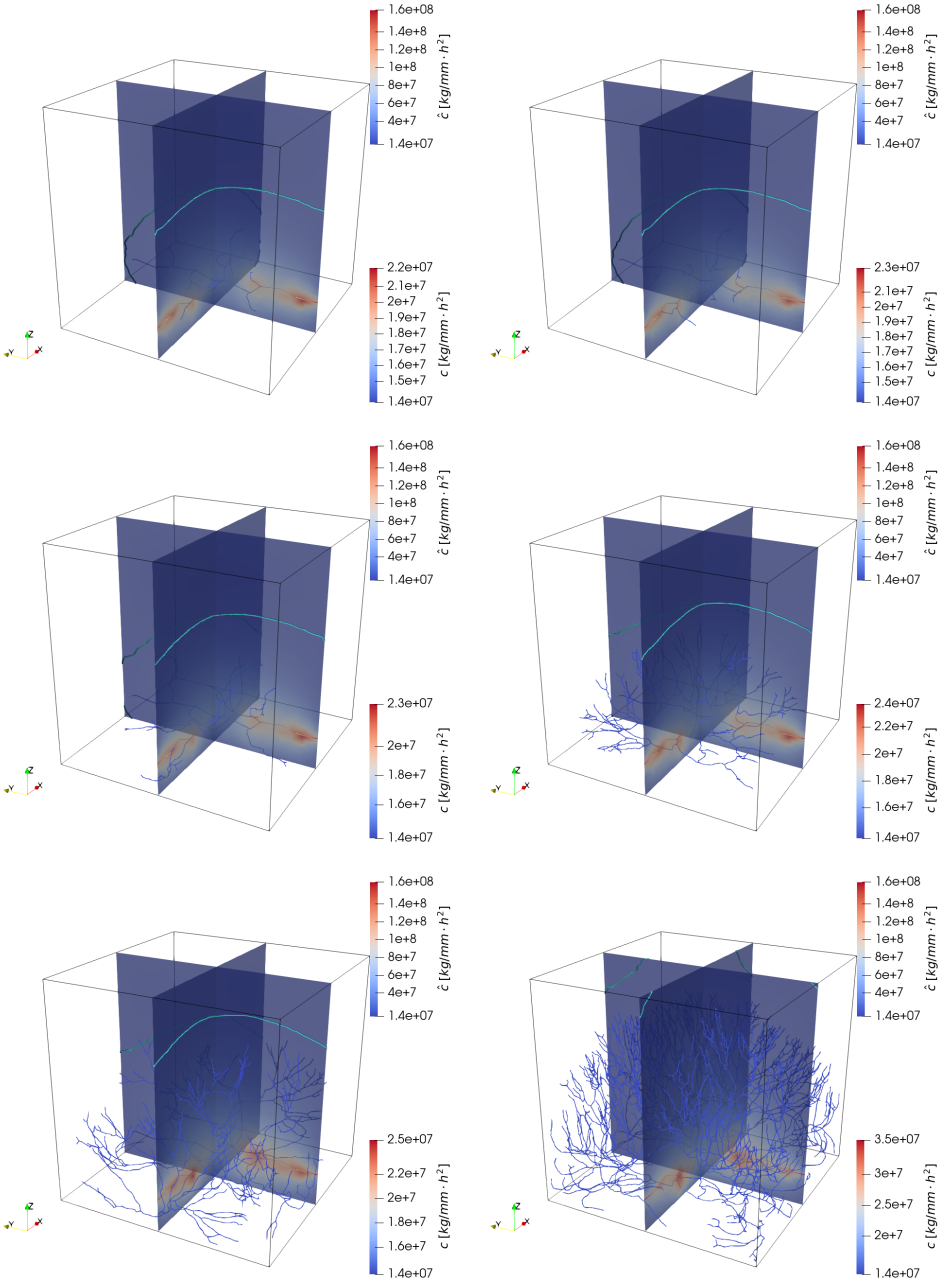

Figure 7.8: Simulation of tumor growth with parameter listed in Tables (4.1), (4.2), (4.3), (7.1). From the top to the bottom, oxygen evolution at time 10, 30, 50 days. On the left panels: results for the homogeneous initial condition. On the right panels: results for the Gaussian initial condition.

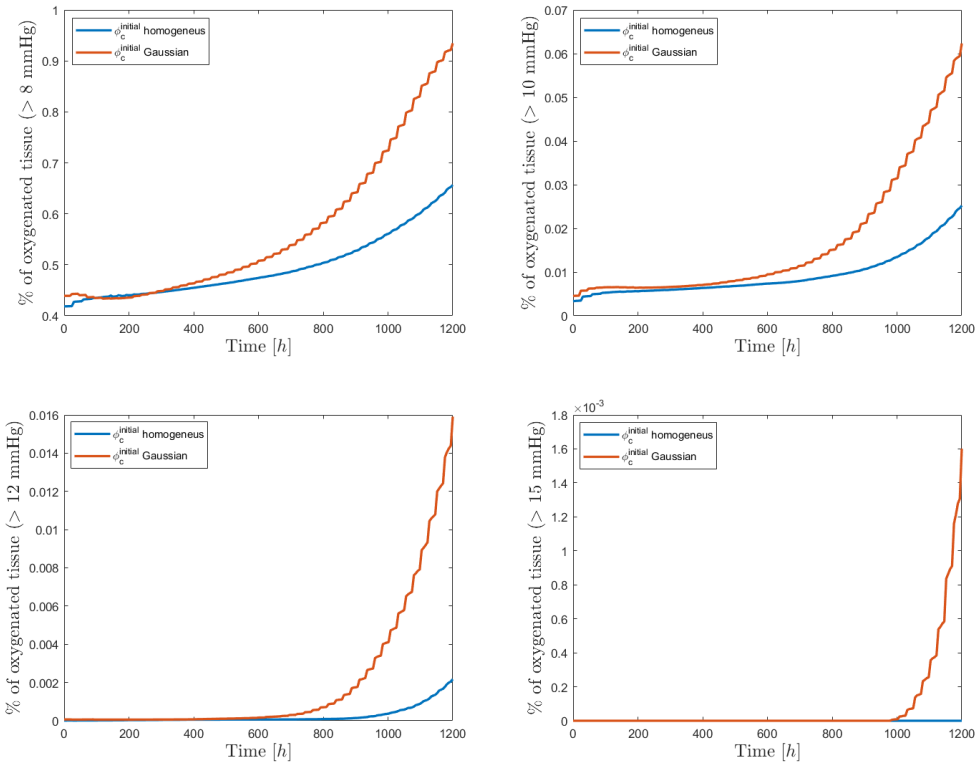

Figure 7.9: Simulation for different cell initial conditions. Analysis of the fraction of oxygenated tissue.

Now, looking at the isolines corresponding to the pathological hypoxia level ($c(\mathbf{x}, t) = 8$ mmHg), we can also observe that the portion of tissue involved by hypoxia condition progressively decreases over the time for both the initial conditions.

Nevertheless, it is also evident that this reduction is much more considerable when we start from the Gaussian distribution of cells, especially looking at the last time step, where the hypoxia affects only the upper corners of the domain.

In order to provide a quantitative measure of the percentage of tissue involved by hypoxia conditions, we can look at Figure (7.9). Here we report the percentage of tissue in which the oxygen concentration is above different thresholds, in particular we consider 8, 10, 12, 15 mmHg.

We can observe that, if we consider the percentage of tissue above the pathological hypoxia level (8 mmHg), the Gaussian setting guarantees a better oxygenation and, at the end of the simulations, about the 90% of the interstitium is not affected by pathological hypoxia condition.

Also the homogeneous initial condition ensures a good oxygenation of the tissue, but since the network development is slower, the oxygenation process is slower too and, after 50 days, only the 50% of the tissue is above the pathological hypoxia threshold.

If we consider higher thresholds, instead, we can observe that, even if with the Gaussian initial condition we still obtain a better oxygenation, the percentage of tissue above a certain threshold decreases as the threshold increases.
More specifically, we can observe that

- the percentage of tissue above 10 mmHg is lower than the 7% in the case of Gaussian initial condition and the 3% in the case of homogeneous one,
- the percentage of tissue above 12 mmHg is lower that the 1.6% in the Gaussian framework and of the 0.4% in the homogeneous one,
- the percentage of tissue above 15 mmHg is lower than the 0.16% in the Gaussian setting and null in the homogeneous one.

Therefore, recalling that $c(\mathbf{x}, t) = 15$ mmHg is the physiological hypoxia level, the oxygenation of the tissue is never high enough to lead it in the physiological hypoxia condition.
To conclude, let us consider the pressure evolution whose results are listed in Figure (7.10). As we can observe, the vascular pressure is always greater than the interstitial one, both for each considered time-step and independently from the cells initial condition. This means that we always obtain an arterious behavior of the vascular network, as expected. It is worth to note that, in the Gaussian framework, the interstitial pressure is greater than the corresponding value in the homogeneous one. This is coherent with the fact that cells concentration in this setting is higher and they can press even more the tissue.

7.3 Sensitivity to parameter changes

In this section we provide some numerical results in order to understand the impact that the variation of some selected parameters has on the process evolution.
In order to achieve this purpose, the starting point for all of the following simulation is the homogeneous distribution of cells and we let vary only one parameter at a time. More specifically, we focus on the variation of the following parameters:

- the permeability to the oxygen of the vascular network, i.e. β_c^0,
- the radius of the blood vessels, i.e. R,
- the cells duplication rate, i.e. γ
- the cells motility coefficient, i.e. $M \cdot E$.

Furthermore, in order to represent the larger number of information in the most clear and concise manner, we analyse the following characteristic quantities:

- the percentage of oxygenated volume for different thresholds (8, 10, 12, 15 mmHg),
- the relative tumor mass increment and the total tumor mass,
- the maximum and the minimum cancer cells concentration,

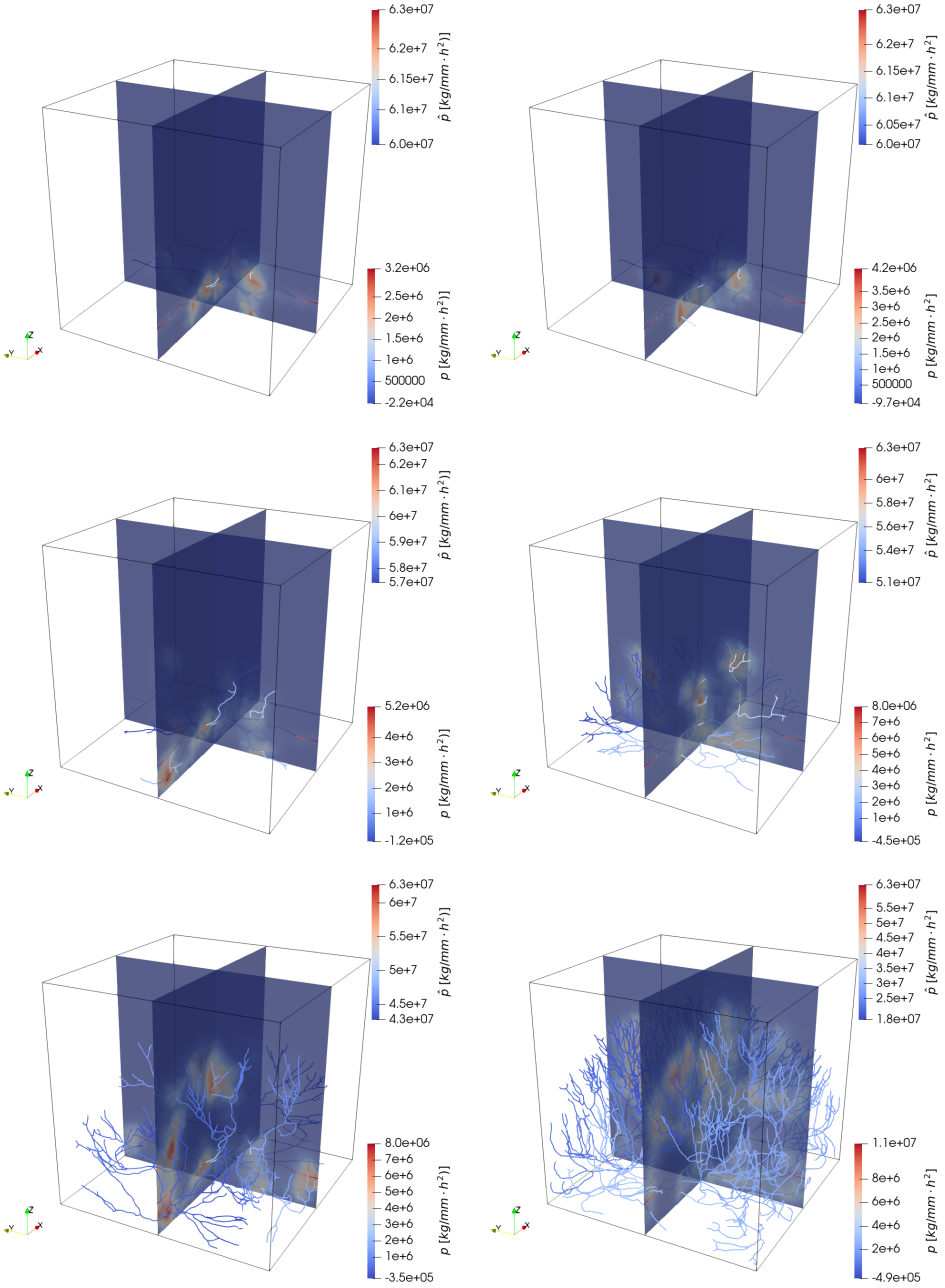

Figure 7.10: Simulation of tumor growth with parameter listed in Tables (4.1), (4.2), (4.3), (7.1). From the top to the bottom, pressure evolution at time 10, 30, 50 days. On the left panels: results for the homogeneous initial condition. On the right panels: results for the Gaussian initial condition.

- the number of active points,
- the final network length.

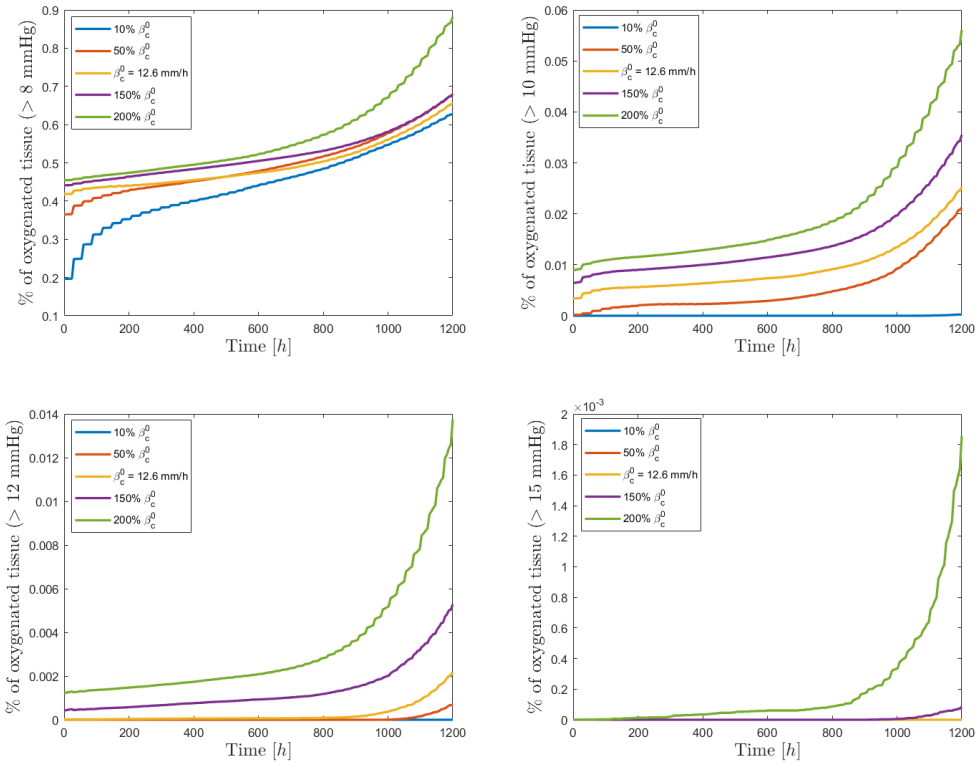

Figure 7.11: Simulations for variations of β_c^0. Analysis of the fraction of oxygenated tissue.

Let us start our analysis from the variation of the parameter β_c^0, that we remind it acts at the interface between the interstitium and the vascular network.
It stands for the vessel wall permeability to oxygen so, the greater its value, the more easily the oxygen can be exchanged form the blood to the tissue.
In the original setting, the parameter value is given by $\beta_c^0 = 12.6$ mm/h and, since we want to understand how its reduction or increment affects the dynamics evolution, we consider the following variations:

- the 10% of the original value,
- the 50% of the original value,
- the 150% of the original value,
- the 200% of the original value.

Let us start from the analysis of the tissue oxygenation and, to this aim, we consider the same threshold introduced for the comparison between the homogeneous and the Gaussian initial condition.
The results are reported in Figure (7.11) and we can observe that, as the permeability increases, the percentage of oxygenated tissue above a certain threshold progressively increases too. Nevertheless, also in this case, we obtain a significant oxygenation of the tissue only when we measure its portion over the pathological hypoxia level (8 mmHg).
In this case, in fact, we reach about the 60% of the tissue above the corresponding threshold for almost every variation of the parameter.
The only exception occurs when the permeability is twice the original one: in this case the percentage of tissue whose oxygenation is greater that 8 mmHg reaches the 90%.
Looking instead at the other considered thresholds, we observe that, as they increase, the percentage of enough oxygenated tissue gets smaller.
Therefore, also in this case, we cannot obtain a configuration in which the physiological oxygenation is restored in the interstitium.

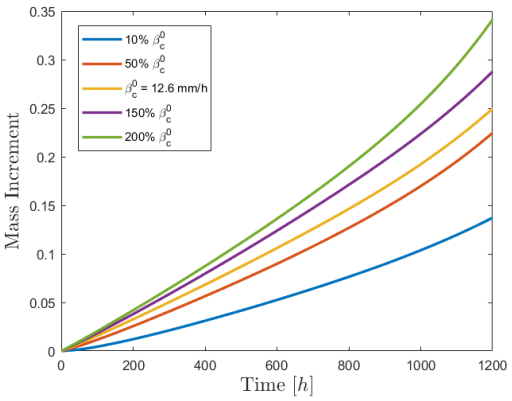

Figure 7.12: Tumor mass increment for variations of the parameter β_c^0

Looking instead at Figure (7.12), we can deduce some informations about the tumor mass and its variation over the time.
More specifically, we can see that the greater the permeability, the greater the tumor mass. This is coherent with the results regarding the oxygenation of the tissue: in fact, as we have already discussed in the previous section, when the available oxygen increases, the proliferation of the cells gets stronger.
Consequently, since a higher permeability ensures a greater oxygen supply, we can detect also a more evident amount of the tumor mass.
Finally, in order to give a measure of the network extension, we can look at Figure (7.13) and Table (7.3), in which we report the number of active points and the total length of the vasculature, respectively.
Also in this case, we can observe that the greatest values both in term of active points and of total length are registered in correspondence to those parameter values that ensure a better oxygenation of the tissue.

Table 7.3: Total Network Length for variations of the parameter β_c^0

Parameter value (mm/h)	10% β_c^0	50% β_c^0	$\beta_c^0 = 12.6$	150% β_c^0	200% β_c^0
Total Network Length (mm)	60.4450	94.1491	92.3408	103.2173	186.7224

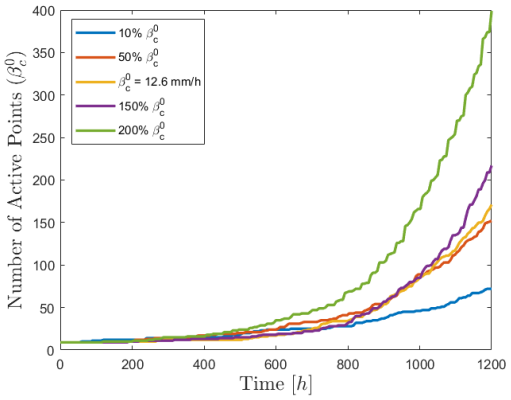

Figure 7.13: Number of active points for variation of the parameter β_c^0

For example, we can observe that when considering a permeability value which is the 10% of the original one, at final time $T = 50$ days the total network length is about 60 mm and we find about 75 active points.
On the opposite side, when we look at the outputs corresponding to a permeability value which is twice the original one, the number of active points is given by 400 and the total network length reaches 186 mm.
These results confirm again that, when the vasculature is properly developed, the oxygenation of the tissue is high enough to guarantee a stronger proliferation of the cells.
Similar considerations also hold for the variation of the blood vessels radius, that in the original framework is set to $R = 5 \cdot 10^{-3}$ mm.
Along the same lines of the previous case, we let the radius change and, more specifically, we consider the following variations:

- the 10% of the original value,
- the 50% of the original value,
- the 115% of the original value.

Looking at the oxygenation levels of the tissue, reported in Figure (7.14), we can observe that when the radius is very small it cannot properly carry nutrients and so the interstitial oxygenation remains even below the pathological hypoxia level.

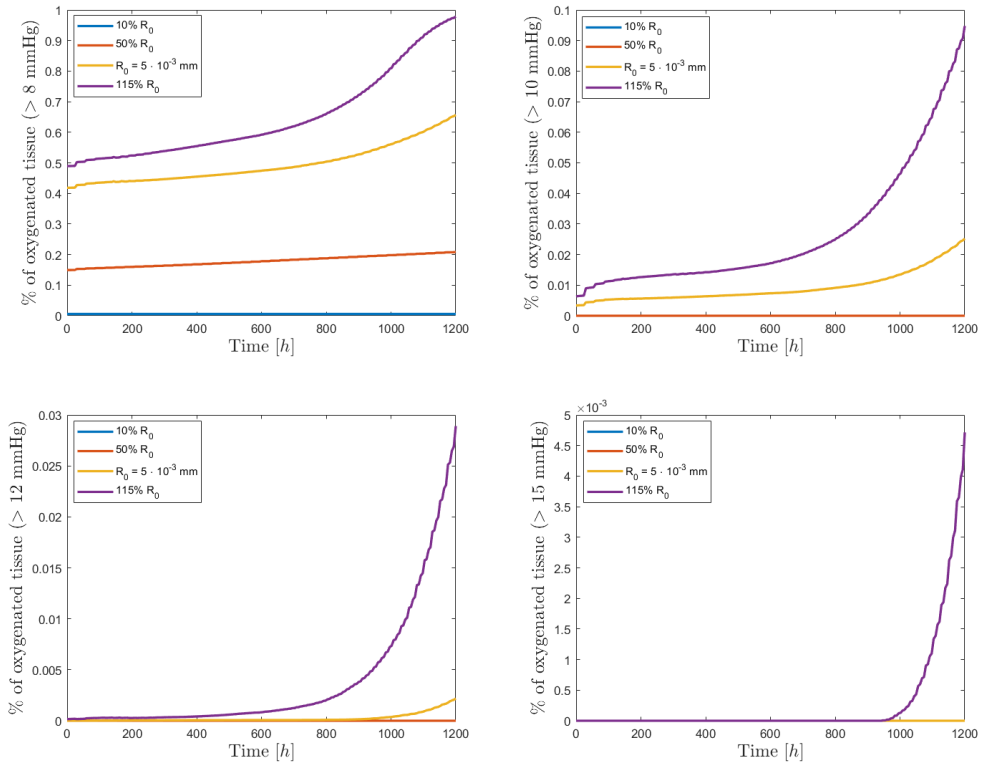

Figure 7.14: Simulations for variations of R. Analysis of the fraction of oxygenated tissue.

On the contrary, when the radius increases, for example when we consider the case in which it is the 115% of its original value, the oxygenation level sensibly increases too and, at time $T = 50$ days, almost the whole tissue is above the pathological hypoxia level.

For what concerns the other thresholds, namely 10, 12, 15 mmHg, also in these cases we cannot identify a configuration in which the oxygenation is considerably high, so we are not able again to reach the physiological hypoxia condition (15 mmHg).

In addition, similarly to the previous analysis, we can still observe that as the oxygenation increases, the tumor mass becomes larger, as reported on the left panel of Figure (7.15). We can see, in fact, that the greatest tumor mass occurs when the radius is twice its original value, which corresponds to the better oxygenation level too.

Table 7.4: Total Network Length for variations of the parameter R

Parameter value (mm)	10% R_0	50% R_0	$R = 5 \cdot 10^{-3}$	115% R_0
Total Network Length (mm)	44.5509	55.7645	92.3408	242.9077

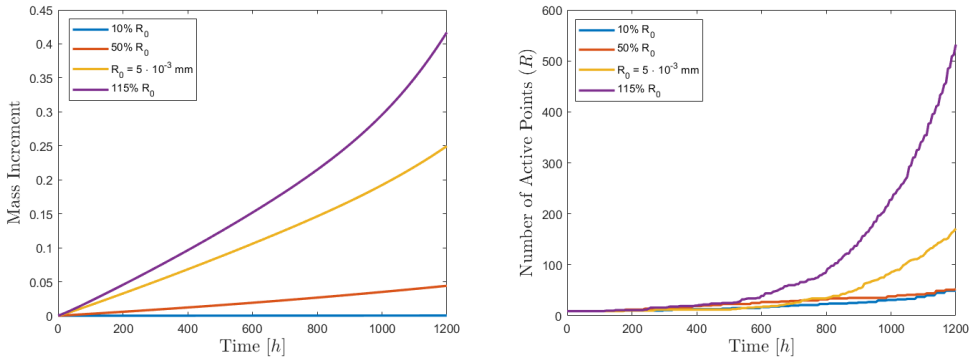

Figure 7.15: Tumor mass for variations of the parameter R

Moreover, looking at the number of active points and at the total network length, whose informations are collected on the right panel of Figure (7.15) and Table (7.4), also in this case we can observe that the considerations carried above are still valid. This means that, in correspondence to higher oxygenation levels, we notice again a more developed blood vasculature that also ensures a more intense cell proliferation.
Let us consider now the variation of another parameter, but this time we move our focus from the oxygen to the cells dynamics.
In this perspective, we consider the cell duplication rate γ, that we remind it acts in the term (5.55) and that in the original framework was set to $\gamma = 1/48$ h^{-1}.
In order to understand the impact that its reduction or increment may have on the evolution of the process, we consider the following variations:

- $\gamma = 1/36$ h^{-1},
- $\gamma = 1/72$ h^{-1},
- $\gamma = 1/96$ h^{-1}.

This time, in addition to the analysis of the tumor mass, we also introduce the evaluation of the maximum and minimum cells concentration values over the time and we report them in Figure (7.16).
As expected, when cells undergo mitosis very rapidly, i.e. γ is high, the maximum and the minimum cell concentrations reach higher values with respect to the case in which the duplication is slower. For example, when we compare the maximum cell concentration corresponding to $\gamma = 1/36$ h^{-1} with the one of $\gamma = 1/96$ h^{-1}, we can observe that the first is sensibly greater than the second. This confirms the fact that, when cells are forced to duplicate themselves quickly, their concentration increases more strongly.
Now, recalling that the tumor mass is given by Equation (7.4), higher values of cancer cell concentration directly reflect on the tumor mass, as reported on the left panel of Figure (7.17).

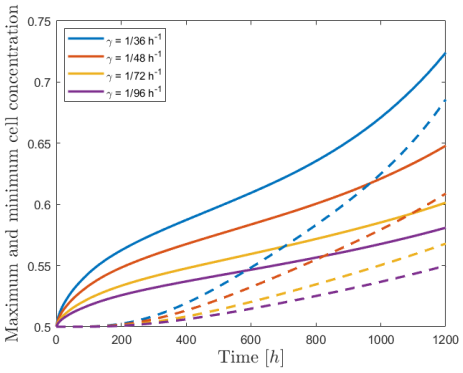

Figure 7.16: Analysis of cancer cell concentration for variation of γ. Continuous lines: maximum cell concentration. Dashed lines: minimum cell concentration.

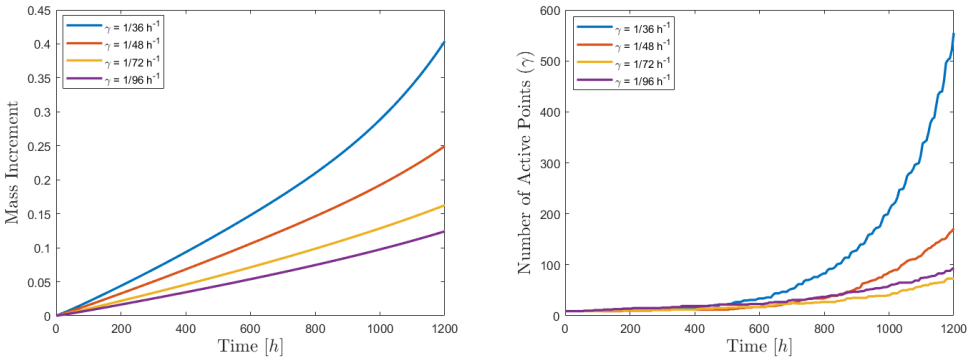

Figure 7.17: Simulations for variations of γ. Left panel: Relative tumor mass increment. Right panel: number of active points.

Here in fact we can observe that, when the duplication is slow, for example $\gamma = 1/96$ h^{-1}, the tumor has a limited growth, both in term of speed and final value.
Finally, if we want to understand the impact that the variation of γ has of the network extension, we can look at the right panel of Figure (7.17) and Table (7.5), in which we report the number of active points and the length of the vasculature, respectively.
We can observe that the results corresponding to $\gamma = 1/48$ h^{-1}, $\gamma = 1/72$ h^{-1} and $\gamma = 1/96$ h^{-1} are about superimposable. Looking instead at the case $\gamma = 1/36$ h^{-1}, we can observe a rapid increment both of the number of active points and of the total network length. This happens because, when cells start proliferating very rapidly, they need more oxygen to survive so they induce a stronger blood vessels development.
This fact is also confirmed by the results reported in Figure (7.18), in which we show again the oxygenation level of the interstitium.
As we can observe, for $\gamma = 1/48$ h^{-1}, $\gamma = 1/72$ h^{-1} and $\gamma = 1/96$ h^{-1}, the percentage for the different thresholds are quite the same. When we look at the results corresponding

Table 7.5: Total Network Length for variations of the parameter γ

Parameter value (1/h)	$\gamma = 1/36$	$\gamma = 1/48$	$\gamma = 1/72$	$\gamma = 1/96$
Total Network Length (mm)	234.8008	92.3408	57.3251	71.6707

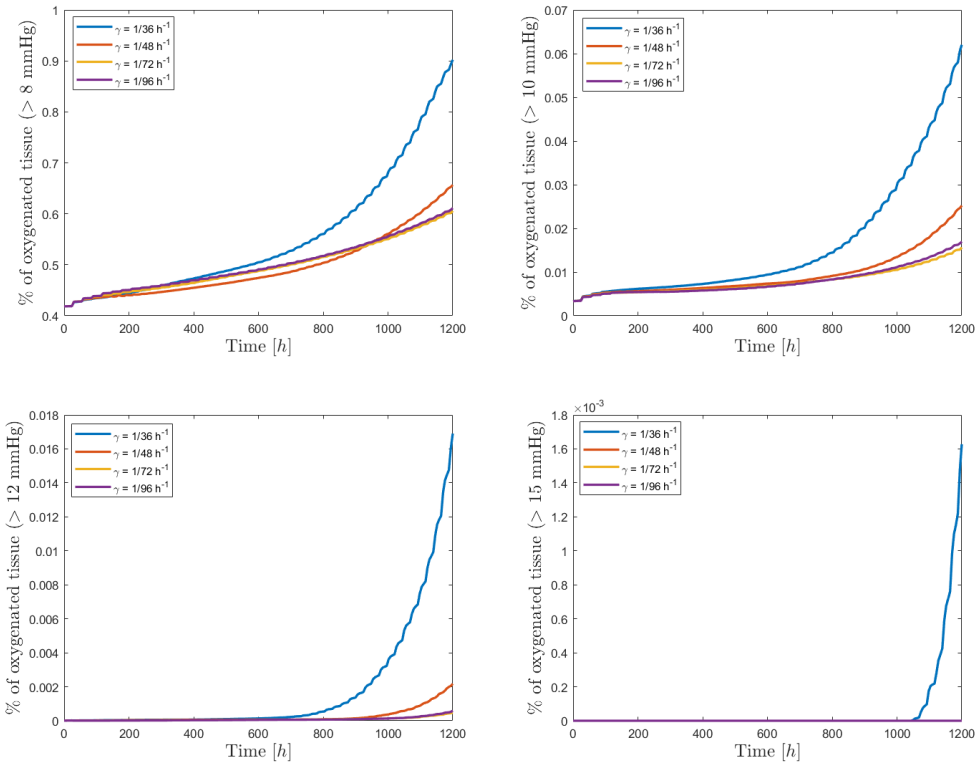

Figure 7.18: Simulations for variations of γ. Analysis of the fraction of oxygenated tissue.

to $\gamma = 1/36$ h^{-1}, instead, we can see that the percentage of oxygenated tissue above the level 8 mmHg sensibly increases, in parallel with the number of active points and the total network length. So, we demonstrate again the fact that a solid vasculature can supply a proper tissue oxygenation.
To conclude, we consider one more parameter that involves the cell dynamics.
We focus now on the motility coefficient of the cells, that in the original setting was given by $M \cdot E = 7.2 \cdot 10^{-3}$ mm^2/h.
In order to understand its impact, we consider the following variations

- $M \cdot E = 7.2 \cdot 10^{-5}$ mm^2/h,
- $M \cdot E = 7.2 \cdot 10^{-1}$ mm^2/h.

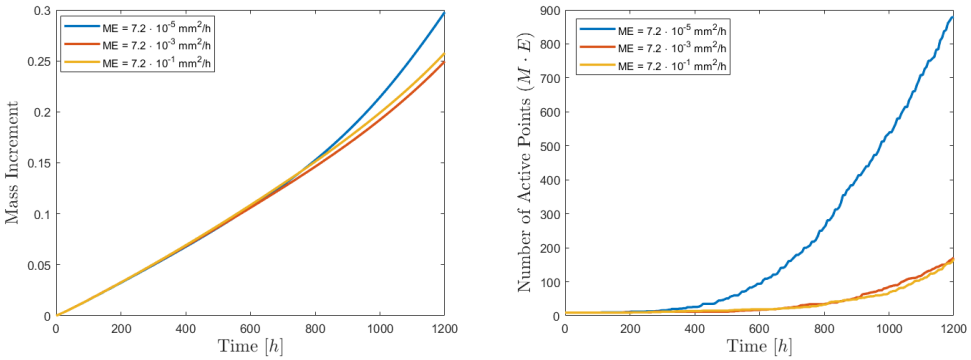

Figure 7.19: Simulations for variations of $M \cdot E$. Left panel: Relative tumor mass increment. Right panel: number of active points.

The starting point of our analysis is the evaluation of the tumor mass, which is reported on the left panel of Figure (7.19). As we can observe, this parameter does not have a huge impact on the mass, which reaches almost the same values independently form the parameter variation. The only exception occurs in the latest phases of the simulations, when we look at the results corresponding to $M \cdot E = 7.2 \cdot 10^{-5}$ mm^2/h.
It is then worth to provide further analysis in order to understand the reason of this even small deviation.

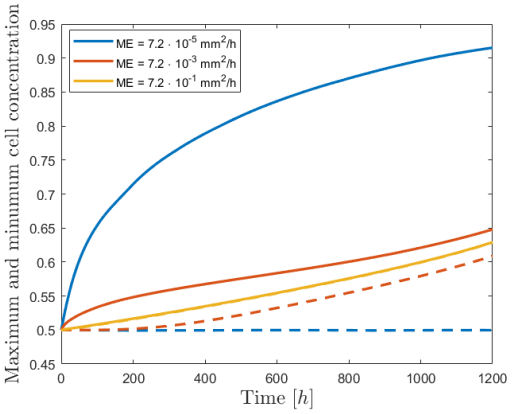

Figure 7.20: Analysis of cancer cell concentration for variation of $M \cdot E$. Continuous lines: maximum cell concentration. Dashed lines: minimum cell concentration.

In this perspective, we examine the behavior of the maximum and minimum cells concentrations, that we report in Figures (7.20). Here we can see that the maximum values are inversely proportional to the motility coefficient: the lower the cells diffusion is, the higher the maximum concentration is.
In addition we can observe that, when $M \cdot E = 7.2 \cdot 10^{-5}$ mm^2/h, the maximum cell

concentration reaches values much greater than the others, which remain rather comparable independently from the parameter variation. In fact, when the cells motility is very small, i.e. $M \cdot E = 7.2 \cdot 10^{-5}$ mm^2/h, the maximum exceeds 0.9, while in all the other cases it reaches about 0.65.
For what concerns the minimum, instead, we can detect a direct proportionality, such that the lower the cells motility, the lower the minimum concentration too.
Also in this case we can observe that the results corresponding to $M \cdot E = 7.2 \cdot 10^{-5}$ mm^2/h are distanced from the ones given by the other variation of the parameter $M \cdot E$.
In particular, the minimum concentration results lower than the other cases, which still remain comparable.
Moreover, when $M \cdot E = 7.2 \cdot 10^{-5}$ mm^2/h, the minimum cells concentration stays unchanged over the time, maintaining the same amount of the initial condition.
Looking again at Figure (7.20) we can also deduce that the lower the cells motility, the greater the differentiation between the maximum and the minimum cells concentration.
We can justify this phenomenon recalling that the motility is related to the random movement of the cells within the spatial domain. This means that, when the motility is high, cells are allowed to migrate, so they can potentially move towards regions with a better oxygenation level. But when the motility is very low, cancer cells are essentially stuck in their initial location.
This means that, if a certain group of cells was initially placed in proximity of a blood vessel, where the oxygen supply is high enough to guarantee their proliferation, cell concentration can increase in that specific portion of the domain.
On the contrary, if we consider cells located in a area with limited oxygen availability, they cannot proliferate so their concentration does not increases over the time.
This can explain why, when we consider $M \cdot E = 7.2 \cdot 10^{-5}$ mm^2/h, we obtain a very high maximum cells concentration, but looking at the minimum we cannot detect any variation.
On the opposite side, when the motility increases, the distance between the maximum and the minimum cells concentration becomes smaller, until the corresponding curves become superimposable, as we can see when $M \cdot E = 7.2 \cdot 10^{-1}$ mm^2/h.

Table 7.6: Total Network Length for variations of the parameter $M \cdot E$

Parameter value (mm^2/h)	$ME = 7.2 \cdot 10^{-5}$	$ME = 7.2 \cdot 10^{-3}$	$ME = 7.2 \cdot 10^{-1}$	$ME = 7.2$
Total Network Length (mm)	490.7984	92.3408	87.9476	67.9777

It is now useful to analyse some information regarding the vasculature extension, so we focus again of the number of active points and the total network length, that we report on the left panel of Figure (7.19) and Table (7.6).
According to the considerations above, we can still observe that the results regarding the parameter values $M \cdot E = 7.2 \cdot 10^{-3}$ mm^2/h and $M \cdot E = 7.2 \cdot 10^{-1}$ mm^2/h are almost comparable both in terms of number of active points and of total network length.

The main difference lies again in the parameter value $M \cdot E = 7.2 \ \cdot 10^{-5}$ mm^2/h, for which the we obtain a much more extended vascular network.
In order to understand the efficiency of the vasculature, we can conclude looking at Figure (7.21), in which we report again the tissue oxygenation level.
As we can see, it does not exist again a parameter configuration leading to a high enough oxygenation that ensure to reach the physiological hypoxia condition.
Nevertheless, when $M \cdot E = 7.2 \ \cdot 10^{-5}$ mm^2/h, the 90% of the tissue reaches the pathological hypoxia level and this results confirms again the fact that cells proliferation is guaranteed when the vasculature is developed enough to supply a good amount of oxygen.

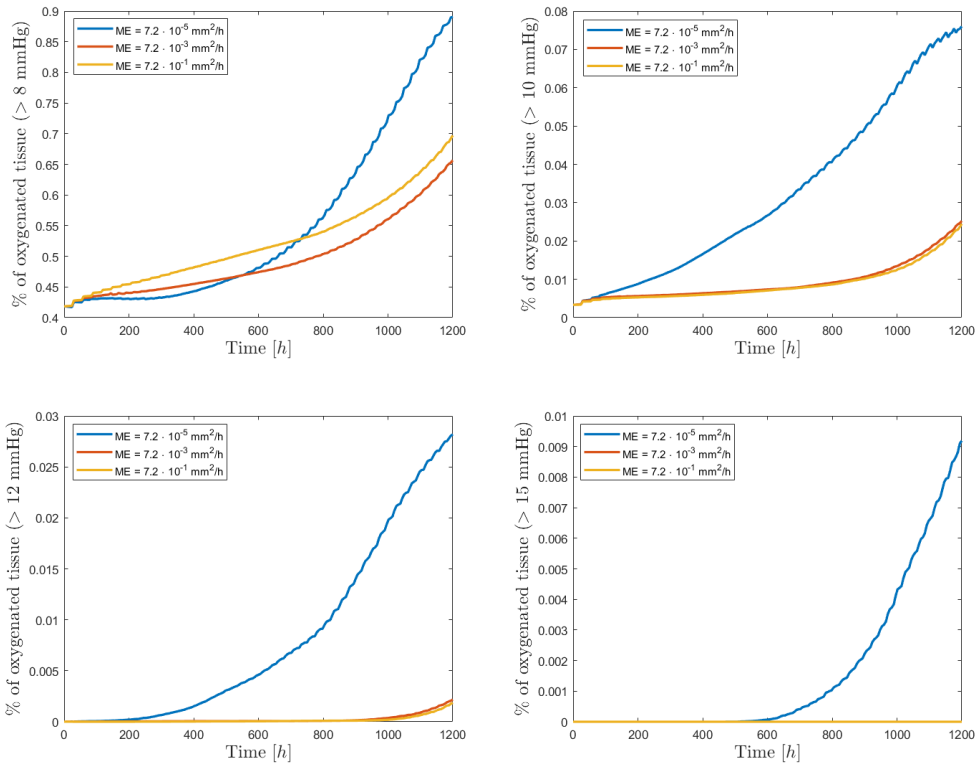

Figure 7.21: Simulations for variations of $M \cdot E$. Analysis of the fraction of oxygenated tissue.

Chapter 8

Conclusions

In this master thesis we provided a mathematical model for the growth of a vascular tumor, combined with the angiogenesis dynamics, i.e the formation of new blood vessels. More specifically, in the first part of the present work, we neglected the evolution of a cancer cells population and we focused on a simplified setting in which we studied only the angiogenesis process. This has been a fundamental step because the development of new blood vessels is itself a complex mechanism, since it involves the interaction between different physical quantities on different scales. In particular, as we focused on the tumor-induced angiogenesis, we took into account the evolution of the endothelial cells, that lead the formation of the nascent vasculature, as well as the pressure, oxygen and endothelial growth factor dynamics. In addition, we have also been able to represent both the pressure and the oxygen trascapillary flux.
However, we have to remind that VEGF is generally produced by the tumor itself, so in this simplified setting in which we do not consider the presence of any cancer cells population, we built an artificial source of endothelial growth factor.
From the mathematical point of view, we initially provided a 3D-3D coupled strategy to describe pressure, oxygen and VEGF evolution. Successively, exploiting the assumption that the blood vessels radius is much smaller than the dimension of the tridimensional domain, we reduced the above model into a 3D-1D coupled one. For what concerns the network, instead, we adopted a discrete tip-tracking model.
In particular, we introduced a growth criterion for the vasculature (the *virtual growth*), such that the effective development of the newly formed vessels does not occur until the distance between two consecutive tip cells does not reach the endothelial cell length.
Regarding the numerical method, instead, we implemented an optimization strategy based on the minimization of a PDE-constrained cost functional.
The numerical experiments performed thanks to the above model, allowed us to capture important aspects related to the network development and the blood flow.
More specifically, we carried an analysis of the VEGF source, acting on the parameters that regulate its intensity and its shape. As expected, we obtained that when the VEGF concentration is higher, we get a more more extended vascular network.
Moreover, changing the shape of the source, we noticed that the growth occurs along the direction of higher concentrations of VEGF, confirming the fact that endothelial cells

move in response to chemotactic stimuli.
In addition, we also considered the variation of the rate at which the network consumes VEGF. In this perspective, we observed that a very high consumption reflects on a very low value of VEGF in correspondence of the network itself, that cannot properly enlarge.
To conclude, in the first part of this work we also carried an analysis of the parameters related to the pressure evolution. Our aim was to reproduce an arterious behavior of the fluxes across the vessel walls, i.e. the blood must flow from the vessels to the interstitium. To this aim, we focused on the permeability of the vessel walls and on the efficiency of the lymphatic drainage.
We observed that when the permeability is not too high, the network is entirely involved by arterious flow, while as the permeability increases, the percentage of vasculature involved by venous behavior increases too.
We also observed that the lymphatic system has a pivotal role in the fluids flow direction, in particular when the drainage is not efficient enough, i.e. the permeability of the lymphatic system is not sufficiently high, the fluid is not properly absorbed and it presses the interstitium. This leads to an inversion of the fluxes and the fluid moves from the tissue to the vessels.
In the second part of the present work, instead, we introduced the tumor growth dynamics. To this aim, the starting point was the model defined for the angiogenesis process but we also introduced the governing law for cancer cells evolution.
The main novelty lies in the fact the we distinguished the cells from the interstitial fluid, so it has been necessary the adoption of a multiphase approach.
In this perspective, we reformulated the equations describing pressure, oxygen and VEGF evolution, taking in consideration the fact that they are dispersed in the liquid phase.
For what concerns the numerical method, the only difference lies in the implementation of the Newton's method for the resolution of cells governing law, while the PDE-constrained method defined in the first part was still applicable for the other quantities.
Thanks to this model and to the corresponding simulations, we deduced important informations related to the tumor growth and the vascularization precess.
In fact, in the second part, we provided many numerical simulations varying different key parameters in order to understand their impact on the whole dynamics.
We started defining two different initial distribution of cells and we understood that, independently from the initial condition, the evolution converges to a configuration in which cells are much more concentrated in correspondence to the vascular network. Here in fact, the proliferation is higher thanks to the large oxygen availability.
We also observed that the VEGF concentration is directly proportional to the number of cancer cells: when the tumor is very extended it easily undergoes hypoxia condition so it produces a larger amount of endothelial growth factor in order to encourage the blood vessels development.
For what concerns the impact of the parameter, we focused on the permeability to oxygen and the radius of the vessel, moreover we analysed the variation of the cells duplication rate and their diffusivity coefficients. We studied the response of the hypoxic volume percentage, the tumor mass, the number of active points and the total network length.
As expected, we found out that when either the permeability or the radius increase, the oxygenation of the tissue increases too, leading to an increment both of the tumor mass

and of the network extension.
Similar reasoning also hold for the variation of the duplication rate: when cells have a fast proliferation their mass increases too and they need a higher oxygen amount to survive. In light of this, they produce more VEGF that stimulate the network development and, consequently, this can ensure a larger oxygen supply.
For what concerns the diffusivity coefficient, instead, it allowed us to understand that the lower is its value, the lower is cells motility too, so only the ones located in proximity of the vessels can effectively proliferate.
To conclude, we provide some considerations regarding possible development of this work. For example, even if we observed that the tumor can proliferate when the oxygen is more available, we have to remind that biological evidences show that cancer cells may response to hypoxia condition moving from an aerobic to an anaerobic metabolism.
This phenomenon is known as *Warburg effect* and it allows cells to produce energy consuming glucose instead of oxygen.
Therefore, the above model could be extended introducing the governing equation of glucose, which could be mainly consumed by cancer cells when the oxygenation of the tissue is not high enough to guarantee their survival.
Moreover, since we consider a simplified setting with a very small initial vasculature, we can imagine to extend the present work considering a larger number of vessels, also with different spatial configurations.
Similarly, we can also work with a greater spatial domain edge length.
Furthermore, it could be interesting the introduction of a method that outlines the interface between cancer and healthy cells, as well as the possibility to study the deformation of the tumor itself.
We may also remove the hypothesis that the extracellular matrix is rigid and inert, so we can examine its consumption introducing also an equation for the degradative enzymes.
Furthermore, we recall that in the present work we solved the cancer cells governing law treating the oxygen concentration as a known term. More specifically, at each time step, we approximated the oxygen with its value at the previous iteration.
In light of this, it could be useful to generalize this method considering the oxygen value at the current time and introducing a non linear Newton method to resolve the non linearity in the corresponding 3D-1D optimization problem.
To conclude, in order to give a measure of the effects that the variation of some key parameter has on some quantity of interest, it could be useful the implementation of the sensitivity analysis. For example, in light of the analysis carried in second part of the present work, we may focus on the wall permeability and on the vessels radius in order to study the variation of the hypoxic volume percentage and the tumor mass in a more rigours way, using sensitivity analysis techniques
To conclude, although the proposed model can still be greatly improved, this work takes the first step towards understanding the modelling of tumor vascularization.

Bibliography

[1] A. L. Bauer, T. L. Jackson, and Y. Jiang. A cell-based model exhibiting branching and anastomosis during tumor-induced angiogenesis. *Biophysical Journal*, 92(9): 3105–3121, 2007. ISSN 0006-3495. URL https://doi.org/10.1529/biophysj.106.101501.

[2] S. Berrone, D. Grappein, and S. Scialò. 3d-1d coupling on non conforming meshes via a three-field optimization based domain decomposition. *Journal of Computational Physics*, 448:110738, 2022. URL https://doi.org/10.1016/j.jcp.2021.110738.

[3] S. Berrone, C. Giverso, D. Grappein, L. Preziosi, and S. Scialò. An optimization based 3d-1d coupling strategy for tissue perfusion and chemical transport during tumor-induced angiogenesis. *Computers & Mathematics with Applications*, 151:252–270, 2023. URL https://doi.org/10.1016/j.camwa.2023.09.046.

[4] S. Berrone, D. Grappein, and S. Scialò. A pde-constrained optimization method for 3d-1d coupled problems with discontinuous solutions. *Numerical Algorithms*, 95(1): 499–526, 2024. URL https://doi.org/10.1007/s11075-023-01579-w.

[5] L. Cattaneo and P. Zunino. Computational models for fluid exchange between microcirculation and tissue interstitium, 2014. ISSN 1556-1801. URL https://www.aimsciences.org/article/id/7cdf7e3a-f8c1-454d-b5e9-46d2150ae68d.

[6] L. Cattaneo and P. Zunino. A computational model of drug delivery through microcirculation to compare different tumor treatments. *International journal for numerical methods in biomedical engineering*, 30(11):1347–1371, 2014. URL https://doi.org/10.1002/cnm.2661.

[7] M. A. Chaplain. Mathematical modelling of angiogenesis. *Journal of neuro-oncology*, 50:37–51, 2000. URL https://doi.org/10.1023/A:1006446020377.

[8] C. D'Angelo. Finite element approximation of elliptic problems with dirac measure terms in weighted spaces: Applications to one- and three-dimensional coupled problems. *SIAM Journal on Numerical Analysis*, 50(1):194–215, 2012. doi: 10.1137/100813853. URL https://doi.org/10.1137/100813853.

[9] C. D'Angelo and A. Quarteroni. On the coupling of 1d and 3d diffusion-reaction equations: Application to tissue perfusion problems. *Mathematical Models and Methods*

in Applied Sciences, 18(08):1481–1504, 2008. doi: 10.1142/S0218202508003108. URL https://doi.org/10.1142/S0218202508003108.

[10] H. B. Frieboes, F. Jin, Y.-L. Chuang, S. M. Wise, J. S. Lowengrub, and V. Cristini. Three-dimensional multispecies nonlinear tumor growth—ii: tumor invasion and angiogenesis. *Journal of theoretical biology*, 264(4):1254–1278, 2010. URL https://doi.org/10.1016/j.jtbi.2010.02.036.

[11] M. Fritz, P. K. Jha, T. Köppl, J. T. Oden, A. Wagner, and B. Wohlmuth. Modeling and simulation of vascular tumors embedded in evolving capillary networks. *Computer Methods in Applied Mechanics and Engineering*, 384:113975, 2021. URL https://doi.org/10.1016/j.cma.2021.113975Getrightsandcontent.

[12] C. Giverso, M. Scianna, and A. Grillo. Growing avascular tumours as elasto-plastic bodies by the theory of evolving natural configurations. *Mechanics Research Communications*, 68:31–39, 2015. URL https://doi.org/10.1016/j.mechrescom.2015.04.004.

[13] C. Giverso, A. Arduino, and L. Preziosi. How nucleus mechanics and ecm microstructure influence the invasion of single cells and multicellular aggregates. *Bulletin of mathematical biology*, 80:1017–1045, 2018. URL https://doi.org/10.1007/s11538-017-0262-9.

[14] I. Gjerde, K. Kumar, and J. Nordbotten. Well modelling by means of coupled 1d-3d flow models. In *ECMOR XVI-16th European Conference on the Mathematics of Oil Recovery*, volume 2018, pages 1–12. European Association of Geoscientists & Engineers, 2018. URL https://doi.org/10.3997/2214-4609.201802117.

[15] M. Hadjicharalambous, E. Ioannou, N. Aristokleous, K. Gazeli, C. Anastassiou, and V. Vavourakis. Combined anti-angiogenic and cytotoxic treatment of a solid tumour: in silico investigation of a xenograft animal model's digital twin. *Journal of theoretical biology*, 553:111246, 2022. URL https://doi.org/10.1016/j.jtbi.2022.111246.

[16] F. Hillen and A. W. Griffioen. Tumour vascularization: sprouting angiogenesis and beyond. *Cancer and Metastasis Reviews*, 26(3):489–502, 2007. URL https://doi.org/10.1007/s10555-007-9094-7.

[17] T. Koch, M. Schneider, R. Helmig, and P. Jenny. Modeling tissue perfusion in terms of 1d-3d embedded mixed-dimension coupled problems with distributed sources. *Journal of Computational Physics*, 410:109370, 2020. URL https://doi.org/10.1016/j.jcp.2020.109370.

[18] T. Köppl, E. Vidotto, and B. Wohlmuth. A 3d-1d coupled blood flow and oxygen transport model to generate microvascular networks. *International journal for numerical methods in biomedical engineering*, 36(10):e3386, 2020. URL https://doi.org/10.1002/cnm.3386.

[19] M. Kuchta, F. Laurino, K.-A. Mardal, and P. Zunino. Analysis and approximation of mixed-dimensional pdes on 3d-1d domains coupled with lagrange multipliers. *SIAM Journal on Numerical Analysis*, 59(1):558–582, 2021. URL https://doi.org/10.48550/arXiv.2004.02722.

[20] F. Laurino and P. Zunino. Derivation and analysis of coupled pdes on manifolds with high dimensionality gap arising from topological model reduction. *ESAIM: Mathematical Modelling and Numerical Analysis*, 53(6):2047–2080, 2019. URL https://doi.org/10.1051/m2an/2019042.

[21] F. Milde, M. Bergdorf, and P. Koumoutsakos. A hybrid model for three-dimensional simulations of sprouting angiogenesis. *Biophysical journal*, 95(7):3146–3160, 2008. URL https://doi.org/10.1529/biophysj.107.124511.

[22] K.-A. Norton and A. S. Popel. Effects of endothelial cell proliferation and migration rates in a computational model of sprouting angiogenesis. *Scientific reports*, 6(1): 36992, 2016. URL https://doi.org/10.1038/srep36992.

[23] T. W. Secomb, R. Hsu, N. Beamer, and B. M. Coull. Theoretical simulation of oxygen transport to brain by networks of microvessels: effects of oxygen supply and demand on tissue hypoxia. *Microcirculation*, 7(4):237–247, 2000. URL https://doi.org/10.1111/j.1549-8719.2000.tb00124.x.

[24] G. Serini, D. Ambrosi, E. Giraudo, A. Gamba, L. Preziosi, and F. Bussolino. Modeling the early stages of vascular network assembly. *The EMBO journal*, 2003. URL https://doi.org/10.1093/emboj/cdg176.

[25] S. Sun, M. F. Wheeler, M. Obeyesekere, and C. W. Patrick. A deterministic model of growth factor-induced angiogenesis. *Bulletin of mathematical biology*, 67:313–337, 2005. URL https://doi.org/10.1016/j.bulm.2004.07.004.

[26] K. R. Swanson, R. C. Rockne, J. Claridge, M. A. Chaplain, E. C. Alvord Jr, and A. R. Anderson. Quantifying the role of angiogenesis in malignant progression of gliomas: in silico modeling integrates imaging and histology. *Cancer research*, 71 (24):7366–7375, 2011. URL https://doi.org/10.1158/0008-5472.CAN-11-1399.

[27] A.-K. Tornberg and B. Engquist. Numerical approximations of singular source terms in differential equations. *Journal of Computational Physics*, 200(2):462–488, 2004. URL https://doi.org/10.1016/j.jcp.2004.04.011.

[28] V. Vavourakis, P. A. Wijeratne, R. Shipley, M. Loizidou, T. Stylianopoulos, and D. J. Hawkes. A validated multiscale in-silico model for mechano-sensitive tumour angiogenesis and growth. *PLoS computational biology*, 13(1):e1005259, 2017. URL https://doi.org/10.1371/journal.pcbi.1005259.

[29] V. Vavourakis, T. Stylianopoulos, and P. A. Wijeratne. In-silico dynamic analysis of cytotoxic drug administration to solid tumours: Effect of binding affinity and vessel permeability. *PLoS Computational Biology*, 14(10):e1006460, 2018. URL https://doi.org/10.1371/journal.pcbi.1006880.

[30] G. Vilanova, I. Colominas, and H. Gomez. A mathematical model of tumour angiogenesis: growth, regression and regrowth. *Journal of The Royal Society Interface*, 14 (126):20160918, 2017. URL https://doi.org/10.1098/rsif.2016.0918.

[31] Y. Wang, Q. S. Zang, Z. Liu, Q. Wu, D. Maass, G. Dulan, P. W. Shaul, L. Melito, D. E. Frantz, J. A. Kilgore, et al. Regulation of vegf-induced endothelial cell migration by mitochondrial reactive oxygen species. *American Journal of Physiology-Cell Physiology*, 301(3):C695–C704, 2011. URL https://doi.org/10.1152/ajpcell.00322.2010.

[32] J. Xu, G. Vilanova, and H. Gomez. A mathematical model coupling tumor growth and angiogenesis. *PloS one*, 11(2):e0149422, 2016. URL https://doi.org/10.1371/journal.pone.0149422.

[33] J. Xu, G. Vilanova, and H. Gomez. Phase-field model of vascular tumor growth: Three-dimensional geometry of the vascular network and integration with imaging data. *Computer Methods in Applied Mechanics and Engineering*, 359:112648, 2020. URL https://doi.org/10.1016/j.cma.2019.112648.